Linköping Studies in Science and Technology
Thesis No. 1301

Combining Analytical and Iterative Reconstruction in Helical Cone-Beam CT

Johan Sunnegårdh

Linköping University
INSTITUTE OF TECHNOLOGY

Department of Electrical Engineering
Linköpings universitet, SE-581 83 Linköping, Sweden

Linköping February 2007

Linköping Studies in Science and Technology
Thesis No. 1301

Author

Johan Sunnegårdh
Department of Electrical Engineering
Linköping University
SE-581 83 Linköping, Sweden

Sunnegårdh, Johan
Combining analytical and iterative reconstruction in helical cone-beam CT
ISBN 978-91-85715-73-2
ISSN 0280-7971

Typeset with LaTeX
Printed in Sweden by LiU-tryck, Linköping, 2007

Abstract

Contemporary algorithms employed for reconstruction of 3D volumes from helical cone beam projections are so called non-exact algorithms. This means that the reconstructed volumes contain artifacts irrespective of the detector resolution and number of projection angles employed in the process. In this thesis, three iterative schemes for suppression of these so called cone artifacts are investigated.

The first scheme, iterative weighted filtered backprojection (IWFBP), is based on iterative application of a non-exact algorithm. For this method, artifact reduction, as well as spatial resolution and noise properties are measured. During the first five iterations, cone artifacts are clearly reduced. As a side effect, spatial resolution and noise are increased. To avoid this side effect and improve the convergence properties, a regularization procedure is proposed and evaluated.

In order to reduce the cost of the IWBP scheme, a second scheme is created by combining IWFBP with the so called ordered subsets technique, which we call OS-IWFBP. This method divides the projection data set into subsets, and operates sequentially on each of these in a certain order, hence the name "ordered subsets". We investigate two different ordering schemes and number of subsets, as well as the possibility to accelerate cone artifact suppression. The main conclusion is that the ordered subsets technique indeed reduces the number of iterations needed, but that it suffers from the drawback of noise amplification.

The third scheme starts by dividing input data into high- and low-frequency data, followed by non-iterative reconstruction of the high-frequency part and IWFBP reconstruction of the low-frequency part. This could open for acceleration by reduction of data in the iterative part. The results show that a suppression of artifacts similar to that of the IWFBP method can be obtained, even if a significant part of high-frequency data is non-iteratively reconstructed.

Sammanfattning

De rekonstruktionsmetoder som idag används för medicinsk datortomografi är alla icke-exakta. Det betyder att de framräknade bilderna innehåller fel, ovasett noggrannhet och upplösning vid datainsamlingen. För konvinklar upp till $\pm 2^\circ$ är dessa fel försumbara, men för högre vinklar uppstår störande artefakter. I denna avhandling undersöks tre metoder för att undertrycka dessa artefakter.

Den första metoden, vars namn på engelska förkortas IWFBP, bygger på iterativ tillämpning av en icke-exakt metod. För denna metod har reduktion av artefakter, brusnivåer samt spatiell upplösning mätts genom rekonstruktion av för ändamålet konstruerade testobjekt. Resultaten visar en tydlig minskning av artefaktnivån under de första fyra iterationerna. En bieffekt är att brusnivån och den spatiella upplösningen ökar. För att förbättra konvergensegenskaper och undvika denna bieffekt föreslås och undersöks en modifikation av den ursprunliga metoden.

Istället för att, som i IWFBP-metoden, använda alla tillgängliga mätningar vid varje iteration, kan en delmängd användas. Detta utgör grunden till metod nummer två, förkortad OS-IWFBP. Effekten av antal delmängder, ordning av dessa samt möjlighet till uppsnabbning av IWFBP-metoden har undersökts. Det visar sig att antalet nödvändiga iterationer sjunker något när dena teknik används. En nackdel är dock att brusnivån ökar jämfört med IWFBP-metoden.

Den tredje metoden bygger på att ingångsdata först delas upp i en lågfrekvent del och en högfrekvent del. Iterativ rekonstruktion görs nu endast på den lågfrekventa delen. Detta kan möjliggöra för uppsnabbning genom nedsampling av data i den iterativa delen. Resultaten visar att artefakter undertrycks ungefär lika mycket som för IWFBP-metoden trots att en betydande del högfrekvent information rekonstrueras icke-iterativt.

Acknowledgments

I would like to take this opportunity to thank the following people that have contributed to this thesis.

First of all, I would like to thank my supervisor Professor Per-Erik Danielsson, whose ideas form the basis of the present work, for his never ending commitment and enthusiasm, for all advice concerning the writing, and for always leaving his door open.

Professor Gösta Granlund for giving me the opportunity to work and study at the Computer Vision Laboratory.

Maria Magnusson for interesting discussions and for providing answers to my never ending flow of questions regarding various topics in the field of image processing and computed tomography.

All other members at the Computer Vision Laboratory for help with various problems and for the friendly and inspiring atmosphere at the laboratory.

Karl Stierstorfer for providing reconstruction software used in the thesis and for being an invaluable source of information about CT reconstruction.

Tommy Elfving for sharing his knowledge in numerical analysis and optimization theory.

My family for all support during the writing of this thesis.

The work reported in this thesis have been supported by Siemens Medical Solutions under the general research agreement “Combining ART and Filtered Backprojection” between the electrical engineering department at Linköping University and Siemens AG, MED CTE.

Contents

Chapter 1

Introduction

1.1 Helical cone-beam computed tomography (CT)

In the areas of medical diagnostics and non-destructive testing, it is of great interest to be able to reproduce images of the interior of objects without destroying them. One common technique for doing this originates from 1972, when Sir Godfrey Hounsfield at Electrical and Musical Industries Limited (EMI) patented the first CT scanner. The technology made a huge success and in 1979, Alan Cormack and Hounsfield were awarded the Nobel Prize for this invention.

A CT scanner uses digitally sampled X-ray projection data from an object collected in many directions to calculate cross-sectional images of the X-ray attenuation. High acquisition speed is generally desirable since this reduces examination time and image artifacts due to motion. Since 1972, several major improvements have been made in this direction, the first one being employment of fan-beam instead of parallel beam geometry.

Since higher data acquisition speed often implies more complicated scanning geometries, the need for novel image reconstruction algorithms have occurred quite frequently. Below follows a presentation of three, from an image reconstruction point of view, interesting developments of the geometrical setup.

- **Fan beam projections.** As shown in Figure 1.1a, early CT scanners captured projection data from parallel rays. This was very time consuming since the source had to travel through all source positions for every projection angle. According to Yang and Firmin [83], Hounsfield recognized early that a considerable increase of data acquisition speed could be achieved by collecting data using fan beams instead of parallel beams. In a fan beam system, every ray originates from the same source position as shown in Figure 1.1b. Later in the thesis it will become apparent that the introduction of a fan beam setup does not complicate the reconstruction problem very much.

- **Helical source path.** Until 1989, the rotating gantry was connected with cables for power supply and data transfer. To avoid self-strangulation, the gantry had to be accelerated and de-accelerated for every reconstructed slice.

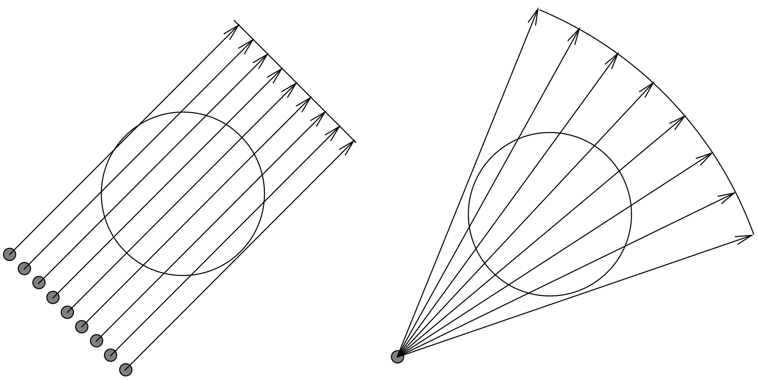

a) Parallel projections b) Fan-beam projections

Figure 1.1: Introduction of fan beam projections

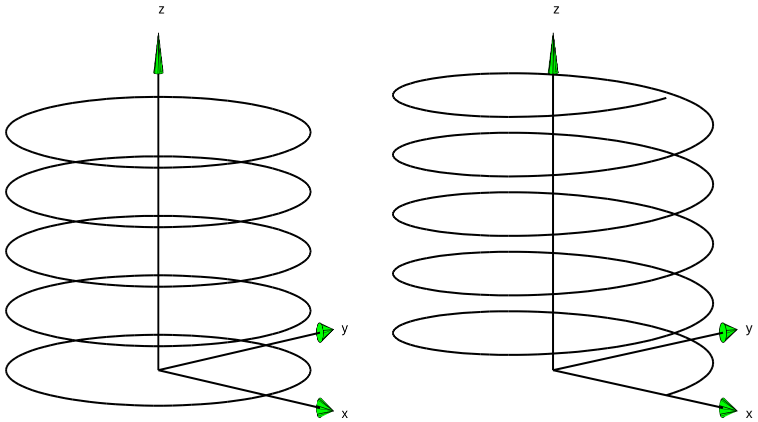

a) Circular source path b) Helical source path

Figure 1.2: Circular versus helical source path geometry. The chosen coordinate system is convenient due to its consistency with other literature in this topic. However, in medical applications the z-axis will of course be directed horizontally.

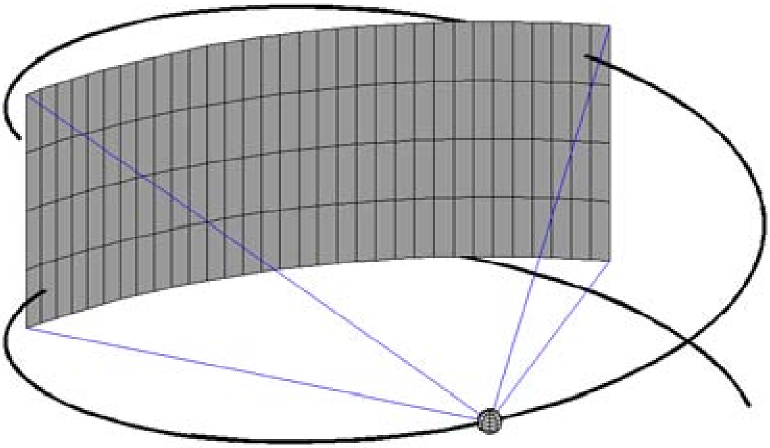

Figure 1.3: The helical cone beam geometry

This resulted in the piecewise circular source path shown in Figure 1.2a. The slip-ring technology, introduced in 1989, made it possible to read and transfer data continuously while rotating the gantry at constant speed. The result is the helical source path shown in Figure 1.2b and a vastly higher data acquisition speed.

- **Cone beam projections.** In the late 1990s, several medical CT manufacturers released so called multi-slice machines, where the single row detector was replaced by a multi-row detector. This resulted in the helical cone beam geometry illustrated in Figure 1.3. In principle, this geometry is identical to the one in Figure 1.2b. However, in combination with the multi-row detector the geometry of Figure 1.3 calls for new reconstruction algorithms.

In helical cone-beam tomography, a difference is made between *exact* and *non-exact* reconstruction methods. Turbell and Danielsson [78] defined exactness of a reconstruction method as follows.

> An exact algorithm is mathematically correct in the following sense. Let ϵ be the largest allowable deviation between the object function and the reconstructed result. Provided there are noise-free projection data, captured with sufficient density along the source trajectory with a detector array having sufficient detector element density, an exact algorithm can deliver the wanted result for any given ϵ.

Another important feature of a helical cone-beam reconstruction method is whether it can handle the so called long object problem. This problem is described by Danielsson *et al.* in [11] and more precisely defined by Defrise *et al.* in [15]. The definition in [15] reads

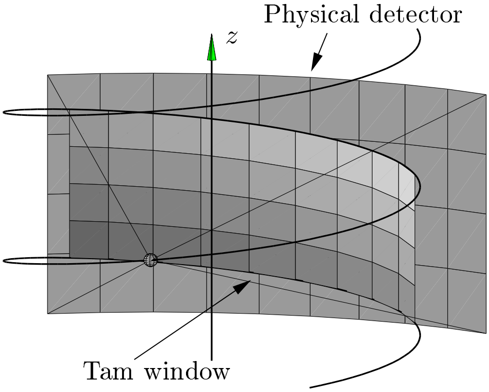

Figure 1.4: Illustration of the Tam-window.

> Long-object problem: given the geometric characteristics of the detector and of the helix, design an exact reconstruction algorithm, which, for reconstruction of a given slice $z = z_0$, only requires CB data to be known in a finite region $\lambda \in [z_0/h - \Delta\lambda, z_0/h + \Delta\lambda]$ with $\Delta\lambda$ independent of the axial extent of the support of $f(\mathbf{r})$.

In this definition, $f(\mathbf{r})$ is the function describing the object to be reconstructed, and λ is the parameter pointing out a certain focus position so that the z-coordinate of the focus is given by $h\lambda$.

The first exact reconstruction methods able to handle the long object problem for helical cone-beam tomography were presented in 1999 by Kudo *et al.* [40], Schaller *et al.* [65] and in 2000 by Defrise *et al.* [15] (see Turbell [77] for a review of these methods). Unfortunately, these methods have a relatively high computational complexity.

In 2001, an exact method, dramatically different method was presented by Katsevich [37, 38]. This algorithm is able to deliver reconstructed output data in a continuous fashion at the same pace as the input scanning, if so required by the application. It has a remarkable simplicity and only one serious drawback. The input data utilized by the reconstruction method is limited to the so called Tam-window. This means that only rays intersecting the area between consecutive turns of the helical source path opposite to the source are used (see Figure 1.4). Therefore, given a fixed speed of rotation for the gantry (the carriage for source and detector) the speed of translation for the patient cannot be varied freely, a feature which seems to be indispensable for most customers of CT-systems.

Since the introduction of the Katsevich method, several improvements of the method have been published. Also other computationally efficient exact methods have been presented by Zou and Pan [88, 89]. One of these methods have the advantage of being able to reconstruct images from data that is truncated in the xy-plane. However, also these methods suffer from the drawback of not being able to utilize redundant data.

For the above-mentioned reasons, contemporary commercial CT scanners all

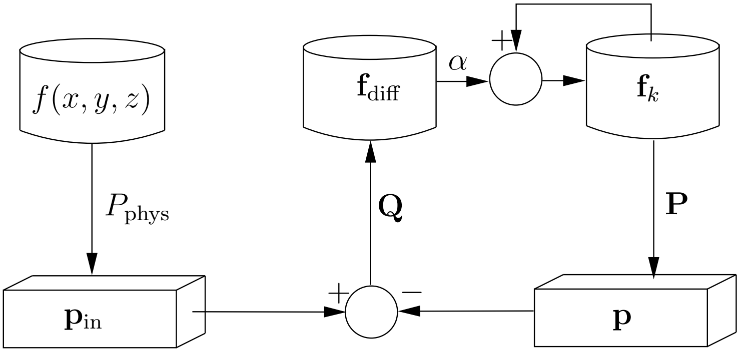

Figure 1.5: The iterative improvement scheme.

employ approximate, i.e. *non-exact* algorithms. These algorithms have relatively low complexity and they allow for high flexibility in terms of translation speed [73], [17]. They seem to produce spotless images for cone angles $|\kappa_{\text{max}}| \leq 2^\circ$ or thereabout. Beyond 2° non-acceptable artifacts appear gradually with increasing cone angle.

1.2 An iterative improvement scheme

In this section we will present a short introduction to the iterative scheme serving as a main component in all experiments presented in this thesis. The main goal with this method is to improve the reconstruction results by means of an iterative procedure. A more detailed presentation and analysis of this scheme is given in Chapter 3.1.

The scheme is illustrated in Figure 1.5. Suppose that input data are represented by a vector $\mathbf{p}_{\text{in}} = P_{\text{phys}} f$, and that a non-exact reconstruction method is represented by the matrix $\mathbf{Q}$. An approximation of the correct result is then given by $\mathbf{f}_{\text{appr}} = \mathbf{Q}\mathbf{p}_{\text{in}}$. By employing a discrete model $\mathbf{P}$ of the physical projection operator P_{phys}, projections $\mathbf{p} = \mathbf{P}\mathbf{f}_{\text{appr}}$ of the approximative result can be calculated. Now, the difference $\mathbf{p}_{\text{in}} - \mathbf{p}$ can be used to create an approximate correction image $\mathbf{f}_{\text{diff}} = \mathbf{Q}(\mathbf{p}_{\text{in}} - \mathbf{p})$. Finally, addition of $\mathbf{f}_{\text{appr}}$ and $\mathbf{f}_{\text{diff}}$ yields a corrected result $\mathbf{f}_{\text{corr}}$, which under certain circumstances contain less artifacts than $\mathbf{f}_{\text{appr}}$. By iterating this procedure, a sequence of gradually improved results is obtained.

Typically, $\mathbf{Q}$ represents a filtered backprojection method. Then, the resulting iterative method belongs to the class of iterative filtered backprojection (IFBP) methods. These methods has successfully been applied to problems where data are missing due to heavy objects [53] and due to an incomplete source trajectory [86]. Danielsson and Magnusson [12] proposed to use this scheme to suppress artifacts caused by non-exact reconstruction.

1.3 Contributions

The main contributions in the thesis are the following.

- Chapter 5. The improvement loop proposed by Danielsson and Magnusson [12] is evaluated, with **Q** being the non-exact weighted filtered backprojection (WFBP) method proposed by Stierstorfer *et al.* [74]. The iterative loop has also been extended with linear regularization resulting in a more stable behavior and controllable spatial resolution.
- Chapter 6. In 1994, Hudson and Larkin [29] showed how a technique called ordered subsets (OS) can be used for accelerating iterative methods for tomographic reconstruction. Here, we show how this technique can be combined with the iterative scheme examined in Chapter 5, and we evaluate the resulting reconstruction method.
- Chapter 7. A new method called frequency domain partitioning (FDP) is introduced and evaluated. This method starts by dividing projection data into one low-frequency part and one high-frequency part. The iterative scheme is applied to the low-frequency part, while the non-iterative WFBP method is used for reconstructing the high-frequency part. Although not explored in this thesis, the FDP technique could make it possible to accelerate the reconstruction by means of downsampling data used in the low-frequency part.

1.4 Thesis outline

Chapter 2 starts with some basic concepts in CT-reconstruction such as ramp filtering and backprojection. This is followed by a short description of the WFBP method.

The topic of Chapter 3 is iterative methods. As an introduction we describe the Landweber method. This is probably the simplest method for iterative reconstruction. Thereafter follow examples and comments on various parameters and alternative methods. In Section 3.2, the concept of basis and irradiation functions is discussed. This is followed by a simple introduction of least square methods and regularization techniques. The motivation behind this section is that the similarity between least square methods and IFBP methods suggests a way to introduce regularization with penalty terms for the IFBP methods. Section 3.4 describes the ordered subsets acceleration technique. Finally, Section 3.5 present the IFBP methods in more detail and show how regularization can be included in the update step.

In Chapter 4, we describe how input data have been generated in the subsequent chapters. Geometrical parameters and the different phantoms used are specified. The different methods used for assessing spatial resolution and measuring noise are also presented.

Chapter 5 starts with a presentation of the iterative weighted filtered backprojection (IWFBP) scheme. Subsequent sections study the behavior over the number of iterations, effects of different resolutions on image quality, and the spatial resolution properties for different amounts of regularization. In Section 5.5, a possible alternation of the scheme is investigated. This is followed by experiments on low contrast phantoms and conclusions.

The first section in Chapter 6 describes how ordered subsets can be combined with the IWFBP method and the parameters specific to this method. Two-dimensional experiments are then performed in order to examine how two prominent parameters, the number of subsets and ordering scheme, affect the results. In Section 6.3, suppression of high-frequent artifacts characteristic to the OS-IWFBP method is investigated. To examine the acceleration of cone-artifact suppression, three-dimensional experiments are performed with the cone angles $\pm 4.8°$ and $\pm 9.6°$.

Chapter 7 presents the FDP scheme, which could allow for acceleration by downsampling the data used in the iterative loop. In this chapter, it is investigated how the reconstruction results are affected in terms of noise and spatial resolution. Especially we compare the IWFBP method and the FDP method *without* downsampling. We also investigate how the reconstruction of a low contrast phantom is affected by variation in sampling density.

Finally, Chapter 8 provides a summary of conclusions and presents questions remaining to be answered.

Chapter 2

Analytical methods for cone-beam CT

2.1 Two-dimensional image reconstruction

The mathematical problem of two-dimensional image reconstruction from line integrals, was first solved by Johann Radon in 1917 [63]. Practical solutions suitable for computer implementations have been an active research topic since the end of the 1960s. Several text books on the topic exist, see for instance the books by Herman [27], Kak and Slaney [34] and Natterer [56]. Here we will present the reconstruction problem in general and the widely used filtered backprojection (FBP) method by Bracewell and Riddle [5]. The presentation is mainly inspired by the more extensive text in [34] and parts of [77] and [66]. Some parts of the material have been copied from [75].

Consider Figure 2.1 illustrating an x-ray beam with initial photon intensity I_0 traveling through an object described by the linear attenuation function $f(x, y)$. After traveling through the object, the remaining photon intensity $I(t, \theta)$ is given by [56]

$$I(t,\theta) = I_0 e^{-\int_{L_{t,\theta}} f(x,y)dl}. \tag{2.1}$$

Taking the logarithm yields

$$p(t,\theta) = -\log\left(\frac{I(t,\theta)}{I_0}\right) = \int_{L_{t,\theta}} f(x,y)dl. \tag{2.2}$$

The linear operator $\mathcal{R}$ mapping $f(x, y)$ to $p(t, \theta)$ is known as the *Radon transform.* Any method for two-dimensional CT reconstruction faces the problem of inverting this transform.

In order to invert the Radon transform, the *Fourier slice theorem* is very useful. It provides a connection between the Radon transform and the Fourier transform of a two-dimensional function:

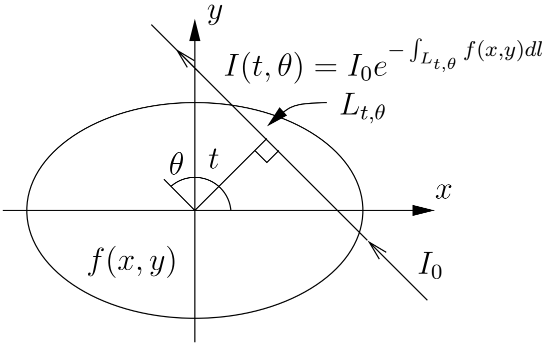

Figure 2.1: The photon intensity of the attenuated and non-attenuated x-ray beams differ by a factor $e^{-\int_{L_{t,\theta}} f(x,y)dl}$.

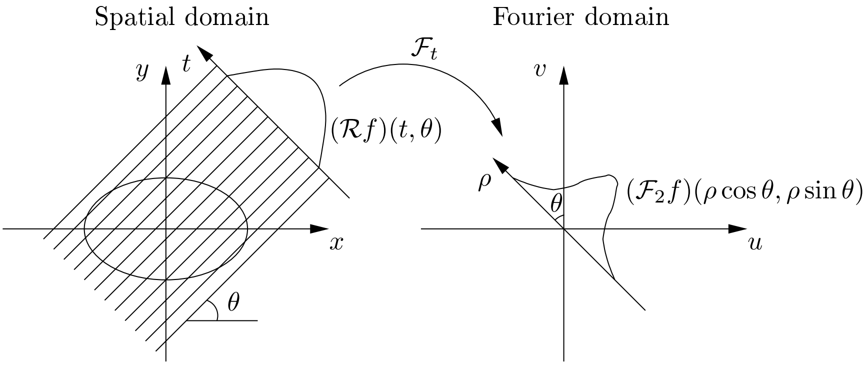

Figure 2.2: Illustration of the Fourier slice theorem.

Theorem 1 (The Fourier slice theorem)**.** *The two-dimensional Fourier transform* $\mathcal{F}_2 f$ *of a function* $f(x,y)$ *along a radial line equals the one-dimensional Fourier transform along the radial direction of the Radon transform:*

$$(\mathcal{F}_2 f)(\rho\cos\theta, \rho\sin\theta) = (\mathcal{F}_t(\mathcal{R}f))(\rho,\theta) = (\mathcal{F}_t p)(\rho,\theta). \tag{2.3}$$

The theorem is illustrated in Figure 2.2 and a formal proof is given by Kak and Slaney in [34].

Theorem 1 can be applied directly to parallel projection data by computing the two-dimensional Fourier transform of $f(x,y)$ through a series of one-dimensional Fourier transforms $\mathcal{F}_t(\mathcal{R}f)$. Performing a final inverse two-dimensional Fourier transform yields the reconstructed result. However, applying Theorem 1 directly is associated with the problem of mapping radially sampled Fourier data to a Cartesian grid. Even if solutions to this problem exist (see Magnusson [66] and O'Sullivan [61]), these *direct Fourier methods* (DFMs) have been less popular than

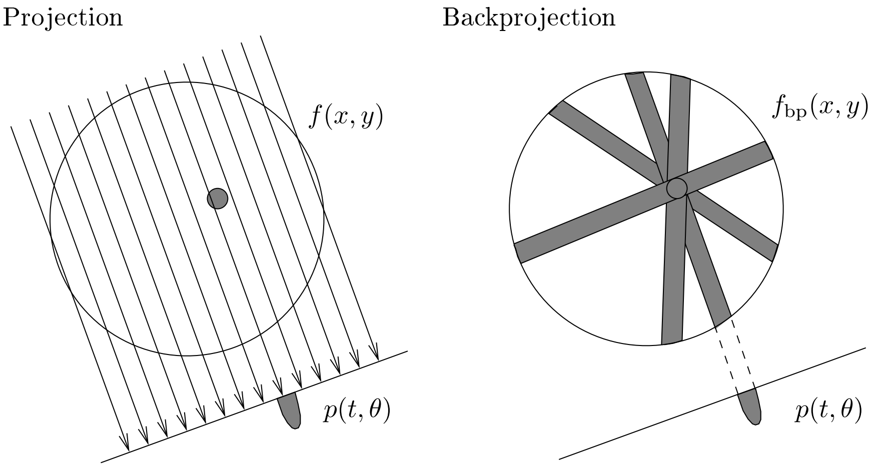

Figure 2.3: Illustration of projection followed by backprojection. Without any filtering of projection data, it is obvious that this has a low-pass filtering effect on the image.

filtered backprojection (FBP).

An FBP method implements the inversion formula

$$f(x,y) = \underbrace{\int_0^{\pi} \underbrace{(p(\cdot,\theta) * g_\infty)}_{\text{filtering}}(x\cos\theta + y\sin\theta,\theta)d\theta}_{\text{backprojection}}\,. \tag{2.4}$$

As a first step, the projection data $p = \mathcal{R}f$ are filtered with a linear and spatially invariant so called *rampfilter* g_∞ in the radial (t) direction. This step is followed by a backprojection, which consists of adding (in the case of a finite number of angles) the filtered projection data to a digital image along the rays from which the projection data has its origin. Projection and backprojection are illustrated in Figure 2.3.

Figure 2.3, inspired by Magnusson [66], also give an intuitive explanation for the point spread function (PSF) of the combined operation projection followed by backprojection. Assume that projections of a small object have been collected and are being backprojected as shown to the right in Figure 2.3. The resulting image $f_{\mathrm{bp}}(x,y)$ is the wanted point spread function. Clearly, this image will non-zero not only on the support of the original object, but also in the rest of the image. In fact, by observing the backprojection contribution to circles centered around the object of interest, we may conclude that $f_{\mathrm{bp}}(x,y)$ decays with $1/\sqrt{(x-x_0)^2+(y-y_0)^2} = 1/d$. Since the 2D Fourier transform of $1/|d|$ is given by $1/|D|$, the inverse filter should look like $|D|$ in the Fourier domain. According to Theorem 1, this filtering can be implemented as an one-dimensional filtering in the radial direction of the projection data $p(t,\theta)$.

Equation 2.4 can be derived mathematically as follows.

$$\begin{aligned}
f(x,y) &= (\mathcal{F}_2^{-1}\mathcal{F}_2 f)(x,y) \\
&= \int_{-\infty}^{\infty} (\mathcal{F}_2 f)(u,v) e^{i2\pi(xu+yv)} du dv \\
&= (\text{Change of vars. :} u = \rho\cos\theta, v = \rho\sin\theta, dudv = |\rho| d\rho d\theta) \\
&= \int_0^{\pi}\int_{-\infty}^{\infty} (\mathcal{F}_2 f)(\rho\cos\theta, \rho\sin\theta) e^{i2\pi\rho(x\cos\theta + y\sin\theta)} |\rho| d\rho d\theta \\
&= (\text{Theorem 1}) \\
&= \int_0^{\pi}\int_{-\infty}^{\infty} (\mathcal{F}_t p)(\rho,\theta)|\rho| e^{i2\pi\rho(x\cos\theta + y\sin\theta)} d\rho d\theta \\
&= \int_0^{\pi} (\mathcal{F}_t^{-1}(\mathcal{F}_t p \cdot \mathcal{F} g_\infty))(x\cos\theta + y\sin\theta) d\theta \\
&= \underbrace{\int_0^{\pi} \underbrace{(p * g_\infty)}_{\text{filtering}}(x\cos\theta + y\sin\theta) d\theta}_{\text{backprojection}} \qquad (2.5)
\end{aligned}$$

Here, g_∞ is a generalized function satisfying $\mathcal{F} g_\infty = |\rho|$. Because of its shape in the Fourier domain, this filter is called a rampfilter.

In a practical implementation, all signals involved are digital. Therefore, the rampfilter g_∞ must be bandlimited and sampled before it can be used. From the theory of sampled signals (see for instance Bracewell [4]), we know that sampling with a distance Δ_t is equivalent to convolution with a Dirac impulse train $\text{III}_{\Delta_t^{-1}}$. Hence, the Fourier transform of the sampled rampfilter is Δ_t^{-1}-periodic. As shown in Figure 2.4, one way to avoid discontinuities in this periodic Fourier transform is to multiply $\mathcal{F} g_\infty$ with a rectangle of width Δ_t^{-1} and sample its inverse Fourier transform. This inverse Fourier transform is given by

$$\begin{aligned}
g(t) &= \mathcal{F}^{-1}\left\{ \frac{\Delta_t^{-1}}{2} \left(\Pi(\rho/\Delta_t^{-1}) - \Lambda(2\rho/\Delta_t^{-1}) \right) \right\} \\
&= \frac{1}{2\Delta_t^2} \operatorname{sinc}(t/\Delta_t) - \frac{1}{4\Delta_t^2} \operatorname{sinc}^2(t/(2\Delta_t)). \qquad (2.6)
\end{aligned}$$

where Π and Λ are rectangle and triangle functions respectively, and

$$\operatorname{sinc}(x) \triangleq \frac{\sin(\pi x)}{\pi x}. \qquad (2.7)$$

Sampling of g with sampling distance Δ_t results in the sequence

$$g_s[k] = g(k\Delta_t) = \begin{cases} \frac{1}{4\Delta_t^2} & k = 0 \\ 0 & k \text{ even} \\ -\frac{1}{k^2\pi^2\Delta_t^2} & k \text{ odd} \end{cases}. \qquad (2.8)$$

Rampfiltered projection data can now be calculated as

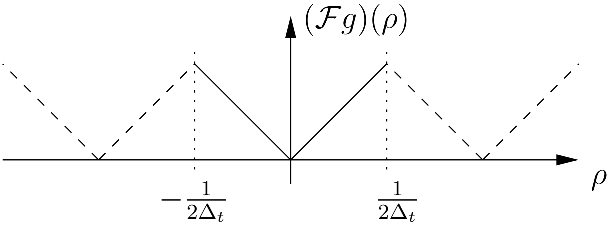

Figure 2.4: By bandlimiting the rampfilter so that no frequencies higher than $\Delta_t^{-1}/2$ exist, the Fourier transform of the bandlimited and sampled rampfilter becomes continuous.

$$q[k,\theta] = \Delta_t \sum_{l=-\infty}^{\infty} g_s[l]p[k-l,\theta] \tag{2.9}$$

where $p[k,\theta]$ are the original projection data for a certain angle θ. We are only interested in the result of this convolution in the interval where $p[k,\theta]$ is non-zero. Therefore, the summation in (2.9) can be made finite by truncating $g_s[k]$ to the double length of this interval.

Discretization of the backprojection operation is done in the following way. Suppose that projection data have been collected for the angles $\theta_0,...,\theta_{N_\theta-1}$, and radial coordinates $t_0,...,t_{N_t-1}$. For each angle θ_l, a continuous projection $q(t,\theta_l)$ is created by means of linear interpolation, *i.e.*

$$q(t,\theta_l) = \sum_{k=0}^{N_t-1} q[k,\theta_l]\Lambda\left(\frac{t-t_k}{\Delta_t}\right). \tag{2.10}$$

The final image can now be created by approximating the integration over angles with a summation, resulting in

$$\begin{aligned} f_{\text{rec}}(x,y) &= \int_0^\pi q(x\cos\theta + y\sin\theta,\theta)d\theta \\ &= \frac{\pi}{N_\theta}\sum_{l=0}^{N_\theta-1} q(x\cos\theta + y\sin\theta,\theta_l). \end{aligned} \tag{2.11}$$

2.2 Weighted filtered backprojection

The weighted filtered backprojection method (WFBP) by Stierstorfer *et al.* [74], is an approximative reconstruction method for helical cone-beam CT, and a main component in the iterative methods examined in Chapter 5, 6 and 7. In the following, we give a presentation of the WFBP method, mainly based on [74].

Four main steps can be identified in the WFBP method.

1) Row-wise rebinning of cone-beam data to semi-parallel data.

2) Ramp-filtering of rebinned projection data.

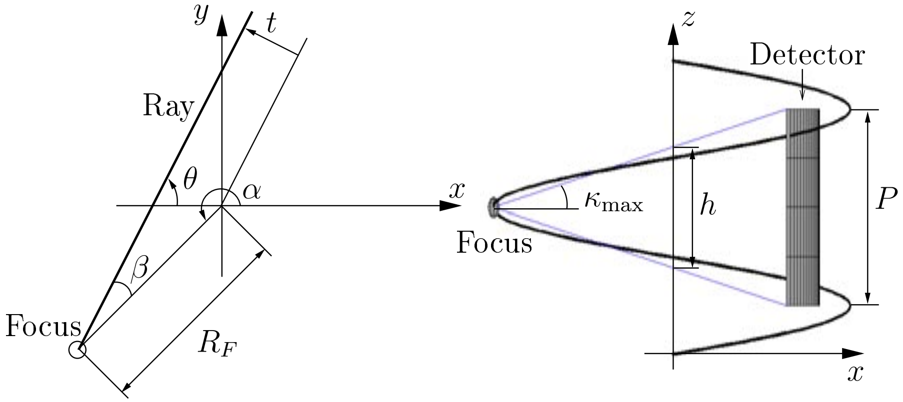

Figure 2.5: Illustration of scanning parameters for the helical cone-beam geometry.

3) Down-weighting of outer detector rows.

4) Normalized backprojection.

Each of these steps will be explained in the following sections.

In order to understand what is done in the different steps, the basic geometry parameters illustrated in Figure 2.5 must be well understood. Given a certain focus angle α, the location of the focal spot is determined by

$$\begin{aligned} x_f(\alpha) &= R_F \cos\alpha \\ y_f(\alpha) &= R_F \sin\alpha \\ z_f(\alpha) &= \frac{P\alpha}{2\pi}. \end{aligned} \tag{2.12}$$

In the helical cone-beam geometry, an arbitrary ray is determined by the angles α, β and a continuous variable $q \in [-1, 1]$ describing the slope of the ray, where $q = \pm 1$ corresponds to rays hitting the top and bottom of the detector respectively. Given these parameters, arbitrary points along the ray can be calculated by

$$\begin{aligned} x_{\alpha,\beta,q}(l) &= x_f(\alpha) - l\cos(\alpha+\beta) \\ y_{\alpha,\beta,q}(l) &= y_f(\alpha) - l\sin(\alpha+\beta) \\ z_{\alpha,\beta,q}(l) &= z_f(\alpha) + ql\tan\kappa_{\max}. \end{aligned} \tag{2.13}$$

Figure 2.5 shows how an arbitrary ray is uniquely determined in the xy-plane, either by specifying α and β or by specifying the angle θ and the orthogonal distance t to the isocenter. Given α and β, the parameters θ and t can be calculated from

$$\theta = \alpha + \beta, \quad t = R_F \sin\beta, \tag{2.14}$$

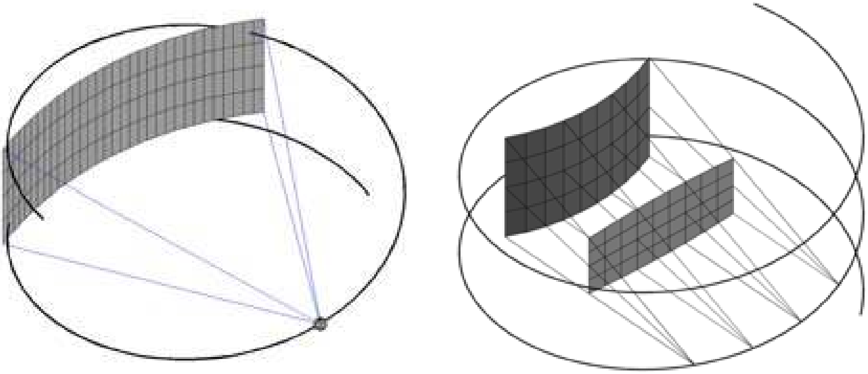

Figure 2.6: The left image shows the helical cone-beam geometry, in which the original projection data have been captured. To the right, the semi-parallel geometry obtained after row-wise rebinning is shown.

or the other way around, if θ and t are known, α and β can be obtained by using the relation

$$\alpha = \theta - \beta, \quad \beta = \sin^{-1}\left(\frac{t}{R_F}\right). \tag{2.15}$$

The procedure of calculating projection data parametrized with θ, t and q from cone-beam data is referred to as row-wise rebinning, meaning that the resampling from a (α, β)-grid to a (θ, t)-grid is done independently for each row. This is the first step in the WFBP method. The resulting geometry is illustrated in the right image in Figure 2.6. Projected onto the xy-plane, the rebinned projections look perfectly parallel. However, the rays diverge in the z-direction and the rebinned projections are therefore called semi-parallel projections.

As a second step in the WFBP method, rampfiltered projections $p_{\text{conv}}(\theta, t, q)$ are obtained from $p(\theta, t, q)$ by applying the rampfilter from the previous section.

Stierstorfer *et al.* [74] showed experimentally that if the outermost detector rows are backprojected with the same strength as the central rows, severe artifacts appear in the result. In order to suppress these artifacts, projection data are weighted with a function of q that approaches zero as q approaches ± 1. More specifically, weighted projection data are calculated as

$$p_W(\theta, t, q) = W_Q(q) p_{\text{conv}}(\theta, t, q) \tag{2.16}$$

where the function $W_Q(q)$ is given by

$$W_Q(q) = \begin{cases} 1 & |q| < Q \\ \left(\cos\left(\frac{\pi}{2}\frac{|q|-Q}{1-Q}\right)\right)^2 & Q \leq |q| < 1 \end{cases} \tag{2.17}$$

Similar to two-dimensional backprojection, the WFBP backprojection constructs a voxel volume as a sum of partial backprojections

$$V_{x,y,z} = \sum_{\tilde{\theta}=0}^{\pi-\Delta_\theta} V_{x,y,z}(\tilde{\theta}) \tag{2.18}$$

over different angles $\tilde{\theta}$. However, in contrast to Equation 2.11, each term in this equation contain contributions from several θ-angles, namely $\theta = \tilde{\theta} + k\pi, k = 0, 1, ...$ The reason for dividing the backprojection in such partial backprojections is connected to what is shown in Figure 2.7. This figure shows how a certain voxel may receive one, two or three contributions from one $\tilde{\theta}$-angle depending on the location of the voxel. Because of this, and the weighting described in the previous paragraph, normalization must be performed for each individual $\tilde{\theta}$-angle. We will describe how the contribution from one such angle is calculated. Given a point (x, y, z) in which we want to know the backprojected values, a first step is to calculate the projection $(\hat{t}, \hat{q}, \hat{l})$ of this point onto the virtual detector plane illustrated in Figure 2.6. This is given by

$$\begin{aligned} \hat{t} &= x\sin(\tilde{\theta} + k\pi) - y\cos(\tilde{\theta} + k\pi), \\ \hat{q} &= \frac{z - P\left(\tilde{\theta} + k\pi - \sin^{-1}\frac{\hat{t}}{R_F}\right)/2\pi}{\hat{l}\tan\kappa_{\max}} \qquad (2.19) \\ \hat{l} &= \sqrt{R_F^2 - \hat{t}^2} - x\cos(\tilde{\theta}) - y\sin(\tilde{\theta}), \end{aligned}$$

$$(2.20)$$

where $k = 0, 1, ...$ Knowing $\hat{t}$ and $\hat{q}$, the normalized partial contribution can be calculated as

$$V_{x,y,z}(\tilde{\theta}) = \frac{1}{H_{x,y,z}(\tilde{\theta})} \sum_k p(\tilde{\theta} + k\pi, \hat{t}, \hat{q}), \tag{2.21}$$

where the normalization sum is given by

$$H_{x,y,z}(\tilde{\theta}) = \sum_k W_Q(\hat{q}). \tag{2.22}$$

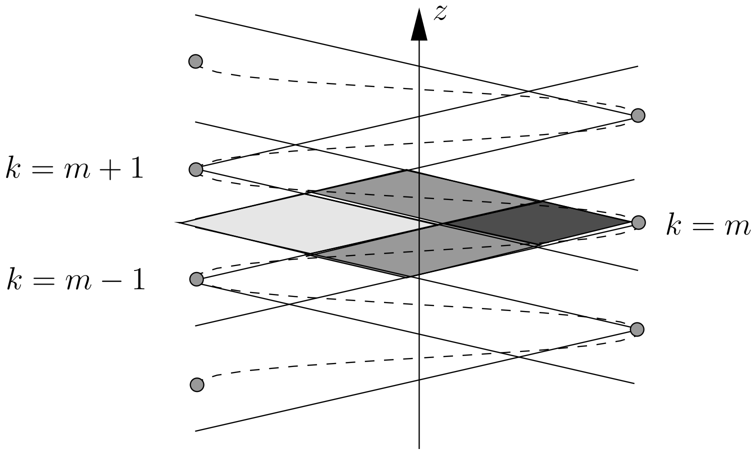

Figure 2.7: Example of how different voxels receive different numbers of contributions during backprojection from a certain angle $\tilde{\theta}$. Voxels located in the lightly shaded area receive a contribution from one focus position. In the medium and dark shaded areas, voxels receive two and three contributions respectively.

Chapter 3

Iterative methods

3.1 Introduction

While analytical reconstruction methods typically implements some analytical inversion formula for the cone-beam transform, iterative methods generate a sequence of estimates that eventually should converge towards a good solution. How this works in principle is illustrated here with the Landweber method, originally developed for iteratively solving Fredholm equations of the first kind [41].

Let the estimates of linear x-ray attenuation coefficients be represented by vectors $\mathbf{f}_k \in \mathbb{R}^N$, and let $\mathbf{p}_{\text{in}} \in \mathbb{R}^M$ represent input projection data. Here, k refers to a certain iteration and each component in $\mathbf{f}_k$ represents a certain voxel. A detailed discussion of the relation between the vector $\mathbf{f}_k$ and corresponding image by means of basis functions is contained in the following section. The update formula for the Landweber method is given by

$$\mathbf{f}_{k+1} = \mathbf{f}_k - \alpha_k \mathbf{P}^T(\mathbf{P}\mathbf{f}_k - \mathbf{p}_{\text{in}}) \tag{3.1}$$

and is illustrated in Figure 3.1. The matrix $\mathbf{P} \in \mathbb{R}^{M\times N}$ is representing a linear model of the physical acquisition process. Thus, $\mathbf{P}$ maps the estimate $\mathbf{f}_k$ onto $\mathbf{P}\mathbf{f}_k$, the projection of the estimate. The difference $\mathbf{P}\mathbf{f}_k - \mathbf{p}_{\text{in}}$ is then used for creating a new estimate by backprojection with the adjoint operator $\mathbf{P}^T \in \mathbb{R}^{N\times M}$, multiplication with the step length α, and finally subtraction from the old estimate.

By keeping α_k constant with respect to k and letting $\mathbf{\Delta} = \mathbf{I} - \alpha\mathbf{P}^T\mathbf{P}$, we see that

$$\begin{aligned}
\mathbf{f}_{k+1} &= \mathbf{\Delta}\mathbf{f}_k + \alpha\mathbf{P}^T\mathbf{p}_{\text{in}} \\
&= \mathbf{\Delta}^2\mathbf{f}_{k-1} + (\mathbf{\Delta}+\mathbf{I})\alpha\mathbf{P}^T\mathbf{p}_{\text{in}} \\
&\vdots \\
&= \mathbf{\Delta}^{k+1}\mathbf{f}_0 + (\mathbf{\Delta}^k + \cdots + \mathbf{\Delta} + \mathbf{I})\alpha\mathbf{P}^T\mathbf{p}_{\text{in}}.
\end{aligned} \tag{3.2}$$

If $\mathbf{\Delta}_k \to \mathbf{0}$, the first term become zero and the expression $(\mathbf{\Delta}^k + \cdots + \mathbf{\Delta} + \mathbf{I})$

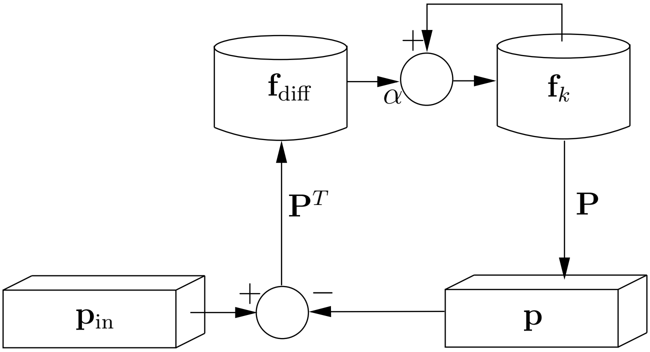

Figure 3.1: Illustration of the Landweber method. In order to calculate a new estimate $\mathbf{f}_{k+1}$, projection data $\mathbf{P}\mathbf{f}_k$ are first calculated. These are then subtracted from the input data and a difference image (gradient) is obtained by back-projection with the adjoint operator $\mathbf{P}$. This difference image is finally multiplied with a step length α and added to the old estimate $\mathbf{f}_k$.

converges to $(\mathbf{I}-\boldsymbol{\Delta})^{-1}$, so that

$$\mathbf{f}_\infty = \lim_{k\to\infty} \mathbf{f}_k = (\mathbf{I}-\boldsymbol{\Delta})^{-1}\alpha\mathbf{P}^T\mathbf{p}_{\text{in}} = (\mathbf{P}^T\mathbf{P})^{-1}\mathbf{P}^T\mathbf{p}_{\text{in}}. \tag{3.3}$$

In the updating formula (3.1), let

$$\mathbf{P}^T(\mathbf{P}\mathbf{f}-\mathbf{p}_{\text{in}}) = \nabla z(\mathbf{f}). \tag{3.4}$$

Since $z(\mathbf{f})$ can be identified as

$$z(\mathbf{f}) = \frac{1}{2}\|\mathbf{P}\mathbf{f}-\mathbf{p}_{\text{in}}\|_2^2, \tag{3.5}$$

the method (3.1) is recognized as a steepest descent method for minimizing $z(\mathbf{f})$ [57]. A presentation of methods that minimize $z(\mathbf{f})$ in (3.5) and variations of this function will be given in section 3.3.

Compared to analytical reconstruction, most iterative methods are painfully slow. However, there are cases where this drawback is outweighed by the relative ease by which the iterative methods handle the *modeling problem*. Any analytical method faces the problem of modeling the *inverse* of every physical phenomenon involved in the data capture. In contrast, iterative methods require an emphasis primarily on modeling the forward version of all such processes. Some examples where iterative methods have been found worthwhile to explore are listed below.

Redundant data: In helical cone-beam tomography, at this time of writing and to the best of our knowledge, there is no exact method able to exploit redundant data for noise reduction, a fact which has forced the CT-industry to rely on non-exact methods. Iterative techniques seem to be able to make these non-exact methods nearly exact, which is precisely the subject of this thesis.

Missing data: One example of how to diminish artifacts due to missing data is given by Zeng *et al.* [86]. Here the Feldkamp method is applied iteratively to reduce errors due to the incomplete circular trajectory data capture.

Resolution recovery: In a simulation study by Nuyts *et al.* [59], iterative methods were shown to increase the spatial resolution in comparison to filtered backprojection.

Beam hardening correction: It has been showed by De Man *et al.* [52] and Elbakri and Fessler [16] that by simulating multienergetic x-rays in the acquisition model, beam hardening artifacts can be significantly reduced.

Metal artifact reduction: De Man *et al.* [51] showed that iterative methods can be used to reduce artifacts caused by the presence of strongly attenuating objects.

Modeling of focus, detector and gantry rotation: In single photon emission tomography (SPECT), modeling of the blurring caused by sources with a non-neglectable spatial extent have successfully been used to recover higher resolution [3]. One could expect the same technique to be applicable to compensate for azimuthal blur caused by the gantry rotation during projection data acquisition in CT.

Primarily, an iterative reconstruction method is characterized by the projection operator and the updating step. Different aspects of the design of the projection operator will be discussed in the next section. Based on how various update steps lead to different results, Xu *et al.* [82] classifies iterative methods as follows.

Conventional algebraic reconstruction techniques include algebraic reconstruction technique (ART) [22], simultaneous algebraic technique (SART) [1], simultaneous iterative reconstruction technique (SIRT) [21] and the Landweber method presented above among others. It was shown by Jiang and Wang [31] that all of them under certain circumstances minimize weighted square norms similar to (3.5). A detailed presentation of these methods is found in Section 3.3.

Iterative filtered backprojection (IFBP) methods: The convergence rates of the above mentioned Landweber and SIRT methods are slow. The number of iterations required to reach the wanted residual error level may exceed 500, where each iteration is more than two times as expensive as one single backprojection step. One way to increase the rate of convergence is to replace the adjoint projection operator $\mathbf{P}^T$ with an analytical, possibly non-exact reconstruction operator $\mathbf{Q}$ including filtered backprojection (FBP). This results in the so called IFBP methods, which are special cases of the "iterative data refinement" scheme proposed by Censor *et al.* [7]. For attenuation correction in SPECT, IFBP was proposed by Chang [8], and Walters *et al.* [81], while Medoff. *et al.* [53] used IFBP for improved reconstruction from limited angles. It was later shown by Xu *et al.* [82] that for emission tomography, the IFBP methods have computational advantages over the conventional and statistical methods. Furthermore, the signal to noise ratio (SNR) in relation to contrast recovery coefficients (CRC) of IFBP methods were comparable to those of regular FBP. Similar results for transmission tomography were later presented by Nuyts *et al.* [59]. Recently, Zeng *et al.* [86] employed an IFBP method for reduction of circular trajectory artifacts in the Feldkamp algorithm. A general presentation of these methods is contained in Section 3.5.

Statistical methods: Statistical image reconstruction methods are based on the Poisson model for the photon density. This is used for deriving the conditional likelihood $P(\mathbf{p}_{\text{in}}|\mathbf{f})$ for the acquired input data given a certain vector $\mathbf{f}$ of linear attenuation coefficients. Bayes rule gives an expression for the reciprocal conditional likelihood

$$P(\mathbf{f}|\mathbf{p}_{\text{in}}) = \frac{P(\mathbf{p}_{\text{in}}|\mathbf{f})P(\mathbf{f})}{P(\mathbf{p}_{\text{in}})}. \tag{3.6}$$

This aim of statistical methods is to maximize this likelihood. If $P(\mathbf{f})$ is assumed to be constant, the method is called a maximum likelihood (ML) method. Otherwise, the method is called a maximum a posteriori (MAP) method. There is an abundance of methods for maximizing the ML and MAP functions. Examples of these are the MLEM method [42], the convex method [43] and the corresponding ordered subsets method [36]. The ML and MAP methods are known to produce images with better signal to noise ratio, and many recent developments toward faster methods make these methods promising. However, since the theory for these methods has little to do with IFBP, statistical reconstruction will not be further discussed in this treatise.

3.2 The projection operator

3.2.1 Basis functions, irradiation functions, and footprints

The following derivation of a matrix formulation of the projection operation $\mathbf{P}$ has mainly been inspired by a paper on local basis functions by Hanson and Wecksung [24]. A continuous three-dimensional image, i.e. a not necessarily continuous function that maps $\mathbb{R}^3$ into $\mathbb{R}$, can be represented as a linear combination of *basis functions* as

$$f_c(\mathbf{r}) = \sum_{j=1}^{N} f_j b_j(\mathbf{r}) \tag{3.7}$$

where $\mathbf{r} \in \mathbb{R}^3$ is a coordinate vector and $b_j : \mathbb{R}^3 \to \mathbb{R}$ are the basis functions (for the 2D case, see Figure 3.2). Usually, these basis functions are translated copies of a single basis function $b(\mathbf{r})$ so that expression (3.7) becomes

$$f_c(\mathbf{r}) = \sum_{j=1}^{N} f_j b(\mathbf{r} - \mathbf{r}_j). \tag{3.8}$$

Here, each $\mathbf{r}_j$ corresponds to the center of a certain voxel. Following this notation, the vectors $\mathbf{f}_k$ from the previous section contain the coefficients f_j in (3.8).

Figure 3.3 shows an illustration of a linear model for the acquisition process in the case of two-dimensional functions. In the three-dimensional case, if non-linear effects in the acquisition process are neglected, the contribution from a continuous three-dimensional image $f_c : \mathbb{R}^3 \to \mathbb{R}$ to a certain detector reading i can be calculated as

$$p_i = \int_{\mathbb{R}^3} w_i(\mathbf{r}) f_c(\mathbf{r}) d\mathbf{r}. \tag{3.9}$$

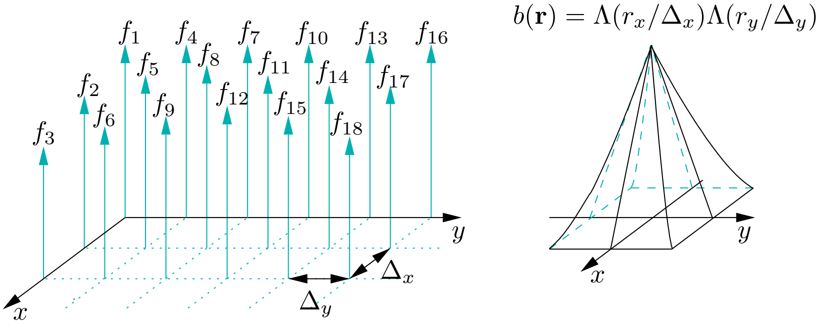

a) **Image coefficients** f_j

b) **Bilinear basis function**

$b(\mathbf{r}) = \Lambda(r_x/\Delta_x)\Lambda(r_y/\Delta_y)$

c) **Interpolated image**

$f_c(\mathbf{r}) = \sum_{j=1}^{18} f_j b(\mathbf{r} - \mathbf{r}_j)$

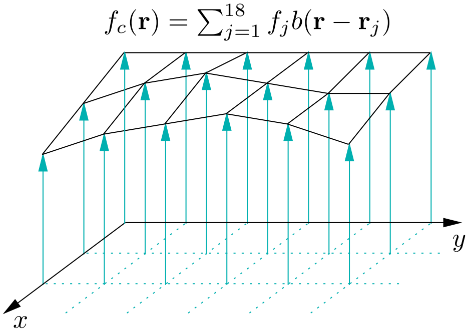

Figure 3.2: Illustration of how a two-dimensional array of image coefficients are mapped onto a continuous function by interpolation with a bilinear basis function.

a) The function $f_c(\mathbf{r})$ **b**) The irradiation function $w_i(\mathbf{r})$

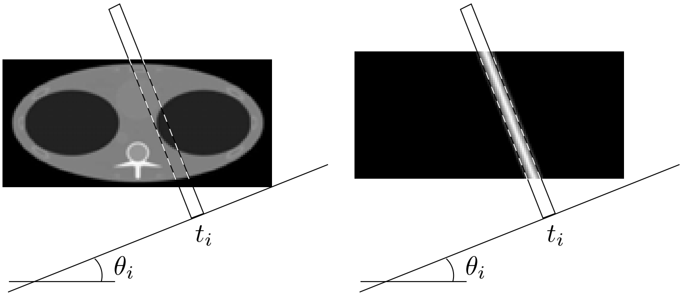

c) The product $w_i(\mathbf{r})f_c(\mathbf{r})$

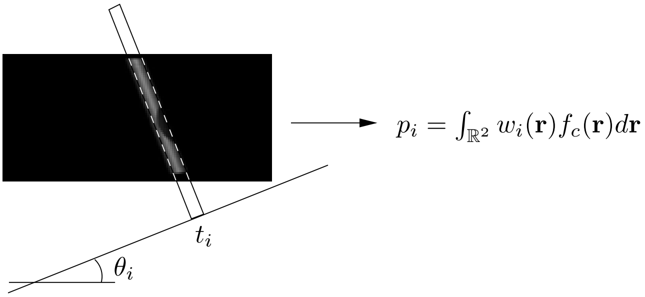

Figure 3.3: Illustration of a linear model for projection generation in the case of two dimensions. The image $f_c(\mathbf{r})$ is first multiplied with an irradiation function specifying the photon flux in different areas of the image. The result is then integrated to get the final result $p_i = \int_{\mathbb{R}^2} w_i(\mathbf{r})f_c(\mathbf{r})d\mathbf{r}$.

The three-dimensional functions $w_i(\mathbf{r})$ will throughout this thesis be called *irradiation functions*. They constitute a model for the source and detector system and contain values of the photon flux for a certain reading i in a certain point $\mathbf{r}$. The simplest and most common choice of functions w_i are Dirac lines, resulting in pure line integral contributions. More elaborate functions such as strips or sums of several Dirac lines can be used to create more realistic models of the acquisition process (to be discussed below in Section 3.2.3.

Insertion of (3.8) into (3.9) yields

$$p_i = \int_{\mathbb{R}^3} w_i(\mathbf{r}) \sum_{j=1}^{N} f_j b(\mathbf{r} - \mathbf{r}_j) d\mathbf{r} = \sum_{j=1}^{N} f_j \int_{\mathbb{R}^3} w_i(\mathbf{r}) b(\mathbf{r} - \mathbf{r}_j) d\mathbf{r} \tag{3.10}$$

From this expression, we see that the projection data $\mathbf{p} = \begin{pmatrix} p_1 & \cdots & p_M \end{pmatrix}^T$ can be calculated by a matrix multiplication $\mathbf{p} = \mathbf{P}\mathbf{f}$ where the components of $\mathbf{P} \in \mathbb{R}^{M \times N}$ are given by

$$p_{ij} = \int_{\mathbb{R}^3} w_i(\mathbf{r}) b(\mathbf{r} - \mathbf{r}_j) d\mathbf{r}. \tag{3.11}$$

For simple irradiation functions such as Dirac lines and strips, the above computation can be efficiently implemented as a simple lookup in a table of pre-computed values (see for instance [87] and [55]). Clearly, if $w_i(\mathbf{r})$ is a Dirac line, (3.11) yields a line integral taken through the basis function. This observation takes us to the important notion of *footprints*. Let $\mathbf{s} \in S^2 \subset \mathbb{R}^3$ be a direction vector and let $\mathbf{t} \in \mathbf{s}^\perp \subset \mathbb{R}^3$ describe a displacement in the orthogonal complement of $\mathbf{s}$. Then the footprint $f(\mathbf{s}, \mathbf{t})$ is defined by

$$f(\mathbf{s}, \mathbf{t}) = \int_{\mathbb{R}} b(\mathbf{t} + t\mathbf{s})dt. \tag{3.12}$$

According to the Fourier slice theorem, the Fourier transform of $f(\mathbf{s}, \mathbf{t})$ with respect to $\mathbf{t}$ equals the Fourier transform of $b(\mathbf{r})$ on $\mathbf{s}^\perp$. Thus, the footprint can be used to study Fourier domain properties of a basis function. Later in this section, examples will be given of basis functions that are defined by specifying their footprints rather than directly specifying $b(\mathbf{r})$. In cases where the footprint is invariant to changes in direction $\mathbf{s}$ and the irradiation functions $w_i(\mathbf{r})$ are Dirac lines, footprint tables can be used for efficient implementations of $\mathbf{P}$ [55].

3.2.2 Basis function properties

Both the choice of basis function $b(\mathbf{r})$ and irradiation functions $w_i(\mathbf{r})$ affect the result of an iterative method. A number of desirable properties for the basis function are listed below.

Accurate representation of constant functions: The basis function should be able to represent a constant function with high accuracy. This property can be described in the Fourier domain by considering the Fourier transform of repeated copies of a basis function b. Let Δ be the repetition distance and let III_Δ be a train of impulses located Δ length units apart from each other. Then, the Fourier transform of the repeated basis functions is given by

$$(\mathcal{F}(\mathrm{III}_\Delta * b))(\mathbf{u}) = (\mathrm{III}_{\Delta^{-1}} \cdot \mathcal{F}b)(\mathbf{u}). \tag{3.13}$$

Assume that we have sampled a constant function. To be able to represent the underlying constant function, the basis function (to be convolved with the samples) must fulfill the following criterion. *Its Fourier transform $\mathcal{F}b$ must be close to zero in all points where the impulses of $\mathrm{III}_{\Delta^{-1}}$ are located, except in the origin.* Otherwise, not only a DC-component will appear in the result, but also false high frequency components.

In one dimension, it is easy to find a function that satisfies the condition above, for instance the standard linear interpolation basis function which is a special case of the so called B-spline functions (see Unser [79]). This can easily be extended to higher dimensional spaces by using Cartesianly separated basis functions such as the bilinear and trilinear basis functions. However, rotationally symmetric basis functions do not fit the Cartesian grid. A simple example of a basis function that severely violates this requirement is illustrated in Figure 3.4 and 3.5. This basis function, which occurs as a special case of a projection method proposed by Peters

[62], is defined by its rotationally symmetric footprint

$$f(\mathbf{s},\mathbf{t}) = \begin{cases} 1 - \frac{|\mathbf{t}|}{\Delta} & |\mathbf{t}| \leq \Delta \\ 0 & \text{otherwise} \end{cases} . \tag{3.14}$$

The Fourier transform of this basis function is exactly zero in the impulse points of $\text{III}_{\Delta^{-1}}$ along a line aligned to one of the main axes. However, if the Fourier transform is considered along a line tilted 45° away from one of the main axes, it is clear that there are non-zero contributions at the impulse points of $\text{III}_{\Delta^{-1}}$. Thus, false high frequencies appear when this basis function is used for approximating a constant function. Danielsson and Magnusson [13] called this phenomenon DC-aliasing since these repeated DC-components are aliased into the Nyquist domain during the projection process. In the same paper, it was explained how the Joseph interpolation [32] (to be presented later in this section) avoids these severe aliasing artifacts. Ohyama *et al.* [60] made similar investigations for a number of different basis functions. However, the special importance of keeping down frequencies near repeated DC-components was not stressed.

Low amount of false frequency components: Since the highest frequency that can be represented by the sampling grid is the Nyquist frequency $1/(2\Delta)$, the basis function should be close to zero outside this limit.

Low computational cost: Since the projection and backprojection operations are the most expensive parts of an iterative methods, the choice of basis and irradiation function should allow for cheap computation of $\mathbf{P}\mathbf{f}_k$. Therefore, it is desirable that the basis and irradiation functions have only a small support, resulting in a sparse matrix $\mathbf{P}$. However, this is not possible to reconcile with the uncertainty principle [4]. Small support and therefore strong variation in the signal domain will inevitably create long extended non-zero tails in the Fourier domain, *i.e.* high amount of false frequencies.

There exist a number of basis functions that fulfill at least the first property in the above list. Frequently occurring in the literature are the square basis function used in the Siddon algorithm [68], the basis function induced by the Joseph projection method [32] and the generalized Kaiser-Bessel basis functions by Lewitt [45, 46]. It was shown by Danielsson and Magnusson [13], and Sunnegårdh [75] that the basis function induced by the SinCot filter by Magnusson [66] yields better results than the Joseph method at the same sampling resolution.

Generally, there is a conflict between the two requirements low aliasing and low cost. Computationally cheap methods often produce more aliasing artifacts and slow methods often produce better image quality. Since Joseph is a good compromise, this method has been used extensively for projection generation in later chapters.

For simplicity, we describe the Joseph method in two dimensions. An extension to three dimensions is straightforward but more difficult to illustrate. In See Figure 3.6. Suppose that the line integral through an image along a line L is to be calculated. The first step in the Joseph method is to divide the image in to a set of lines, parallel either to the x-axis or y-axis, so that the line L is as perpendicular as possible to the lines in the set. The next step is to calculate contributions from each intersection between L and the set of vertical lines. Finally, a length

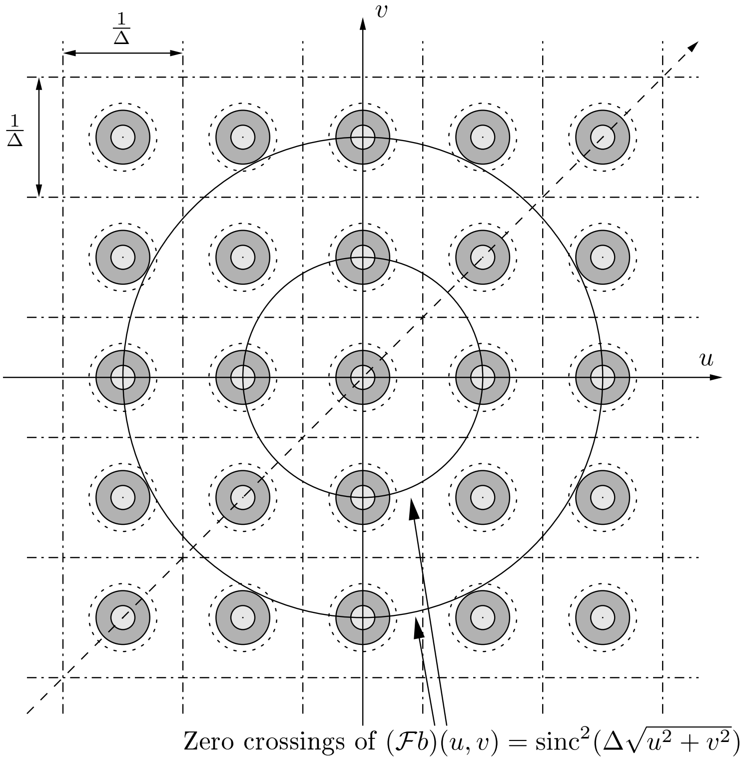

Figure 3.4: Illustration of the periodic Fourier transform of a sampled image and zero crossings for the function $\mathrm{sinc}^2(\Delta\sqrt{u^2+v^2})$.

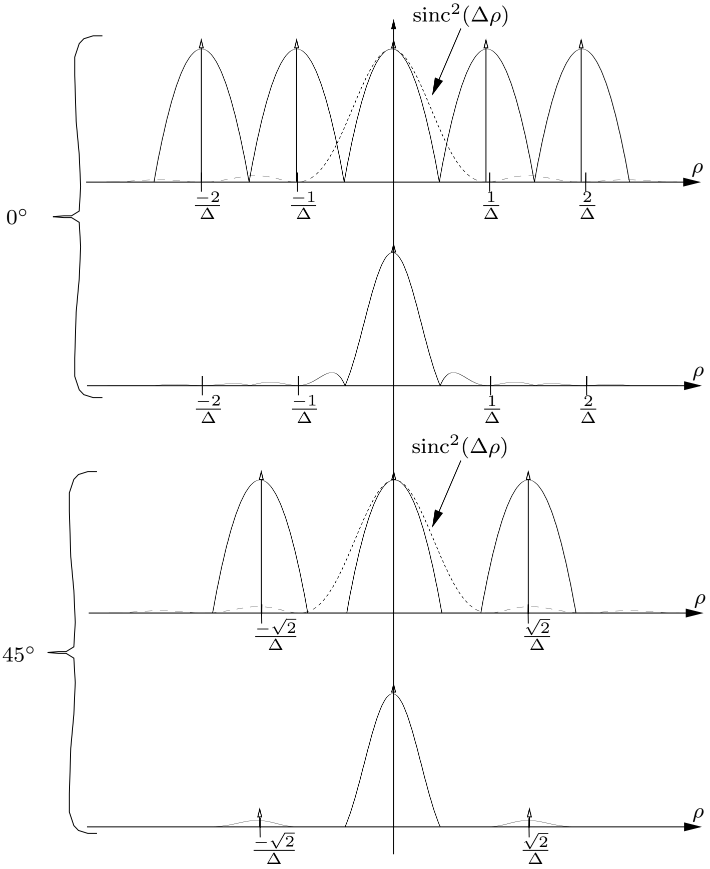

Figure 3.5: Two intersections through the Fourier transform shown in Figure 3.4. Since $\mathcal{F}b$ is zero for $\rho = \sqrt{u^2+v^2} = ..., -\Delta^{-1}, 0, \Delta^{-1}, ...$, the repeated DC-components are perfectly eliminated. However, this is not true in the 45° direction where false high frequency components are introduced.

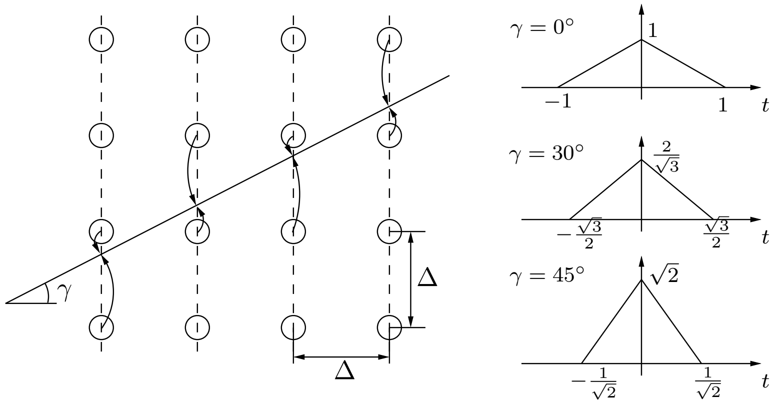

Figure 3.6: Illustration of the Joseph projection method. Depending on the slope of the line integral to be calculated, the image is divided into a set of lines such that the angle γ does not exceed 45°. At each intersection between the line and this set of lines, a contribution is calculated by means of linear interpolation. This results in a triangular footprint $f(\mathbf{s}, \mathbf{t})$ with a width that varies between Δ and $\frac{\Delta}{\sqrt{2}}$. When all contributions have been added, a final division by $\cos(\gamma)$ is made to normalize the integral of the convolution kernel to unity.

correction is made by division with $\cos(\gamma)$ where γ is the angle between L and the normal to the images.

As mentioned before, the Joseph method does not suffer from DC-aliasing. Danielsson and Magnusson [13] showed this by studying the footprint

$$f(\mathbf{s}, \mathbf{t}) = \begin{cases} \frac{1}{\cos(\gamma(\mathbf{s}))}\left(1 - \frac{|\mathbf{t}|}{\Delta\cos(\gamma(\mathbf{s}))}\right) & |\mathbf{t}| \leq \Delta\cos(\gamma(\mathbf{s})) \\ 0 & \text{otherwise} \end{cases} \tag{3.15}$$

where $\gamma(\mathbf{s})$ is the angle in Figure 3.6. Except for the compression factor $\cos(\gamma(\mathbf{s}))$, this expression is identical to (3.14). By reasoning in the same way as in that example, we see that since the footprint is compressed with a factor $\frac{1}{\sqrt{2}}$ in the 45°-direction, the Fourier transform is stretched with a factor $\sqrt{2}$. Therefore, all non-central repetitions of the DC-component are eliminated also in the 45°-directions, and in the directions $\arctan(\pm 1/2)$ as well.

3.2.3 Irradiation functions

In the previous section, the irradiation function w_i was a single Dirac line. There are at least two reasons to consider other types of irradiation functions.

1) In order to capture all information delivered by the input data, it is desirable to use a relatively high voxel density in comparison to the ray density. During projection generation, such a relation between the detector and voxel density may give rise to aliasing. This is realized by first studying the continuous

projection of the continuous image obtained by convolution by the basis function. The next step is to see whether the assumptions of the sampling theorem [4] are violated during sampling of this continuous projection. As illustrated in Figure 3.8, this type of aliasing will occur for a wide range of sampling densities Δ_z in a situation where the rays are diverging, like in the z-direction in the semi-parallel geometry after rebinning in the WFBP method.

To use an irradiation function that consists either of several Dirac lines or a strip is equivalent to convolve the continuous projection with a certain low-pass filter prior to sampling. Therefore, these types of irradiation functions can be used for suppressing aliasing in the projection generation process.

2) The line integral model of the acquisition process is rather crude since the gantry rotation and size of focus and detectors is neglected. A better model would take into account the smoothing caused by these elements.

Various examples of irradiation functions other than Dirac lines exist in the literature. In the papers by Hanson and Wecksung [24], and Ohyama *et al.* [60], strip integrals (see Figure 3.7) were used in combination with the square basis function in two dimensions. In both papers, better results were achieved with strips than with Dirac lines. The problem of aliasing was pointed out by Mueller *et al.* [54] and a space variant scaling of the basis functions (in this case blobs) was suggested to suppress aliasing artifacts. Later, Ziegler *et al.* showed that suppression of these artifacts can be done by using divergent strip irradiation functions in combination with blob basis functions [87]. De Man and Basu [50] proposed a technique for generating projections that resembles the Joseph interpolation but instead of a triangular interpolation function uses two rectangles with different widths convolved with each other. These widths were chosen to be the image sampling distance and the spatial dependent ray distance respectively. Thus, in terms of basis and irradiation functions, the first rectangle would correspond to the basis function and the second to the irradiation function. We believe that this idea should be highly beneficial to apply in the divergent projection field in Figure 3.8.

3.3 Least squares methods. Regularization

Least squares methods for image reconstruction are iterative methods designed to find the $\mathbf{f} \in \mathbb{R}^N$ that minimizes

$$z(\mathbf{f}) = \frac{1}{2}\|\mathbf{P}\mathbf{f} - \mathbf{p}_{\text{in}}\|^2_{\mathbf{W}} = \frac{1}{2}\|\sqrt{\mathbf{W}}(\mathbf{P}\mathbf{f} - \mathbf{p}_{\text{in}})\|^2 \tag{3.16}$$

where the square root $\sqrt{\mathbf{W}}$ exists since the matrix $\mathbf{W}$ is assumed to be positive semidefinite. The matrix $\mathbf{W}$ can be used either to assign individual weight to each detector element, or it could be a ramp-filter that rescales the problem and makes it easier to find a solution.

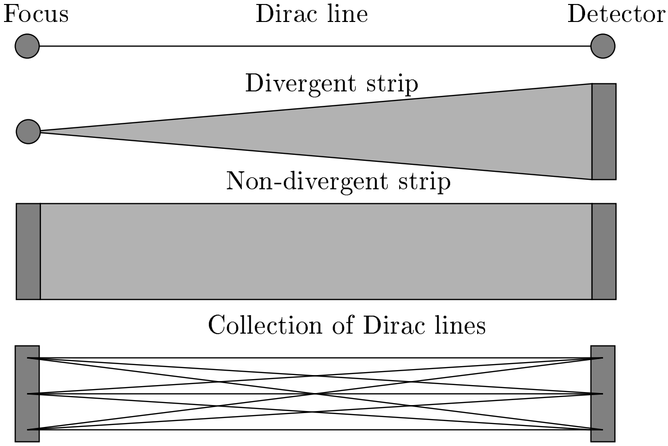

Figure 3.7: Examples of different irradiation functions.

a) High frequencies located close to the focus

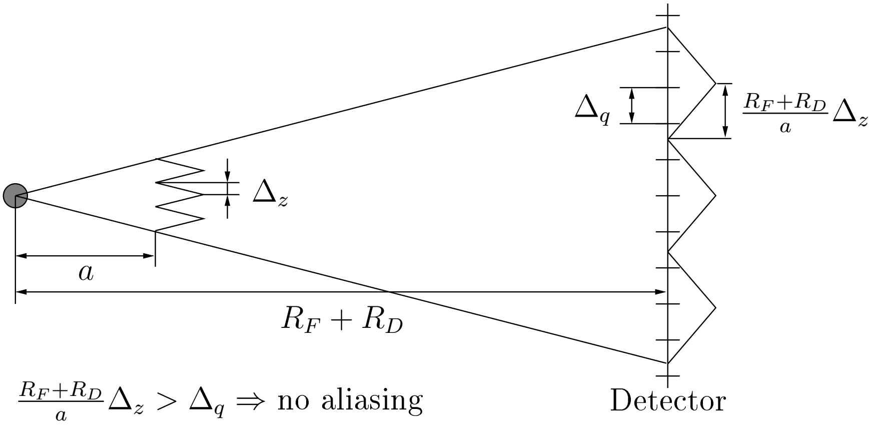

b) High frequencies located far from the focus

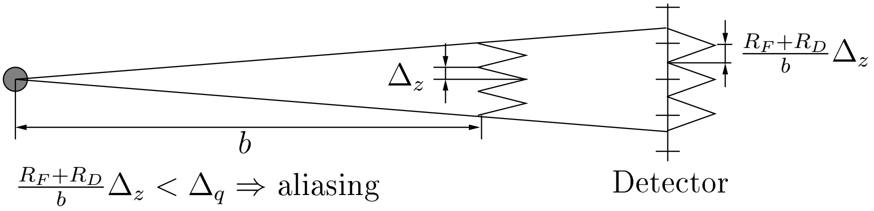

Figure 3.8: An illustration of how aliasing occur during projection generation. High frequencies located close to the focus are projected to relatively low frequencies on the detector, while high frequencies located far from the focus are projected to relatively high frequencies on the detector.

Since $z(\mathbf{f})$ is convex and bounded below, there exists a solution to the problem (3.16). However, if the number of voxels, i.e., the number of components N in $\mathbf{f}$ is chosen high enough, the matrix $\mathbf{P}$ will not have full column rang and the solution will not be unique. One way to ensure uniqueness is to add a minimum norm constraint and solve

$$\text{argmin}_{\mathbf{f}\in\mathcal{S}} \|\mathbf{f}\|, \ \mathcal{S} = \{\mathbf{f} \in \mathbb{R}^N, \|\mathbf{P}\mathbf{f} - \mathbf{p}_{\text{in}}\|^2_{\mathbf{W}} \text{ is a minimum}\} \tag{3.17}$$

instead of (3.16).

The analytical solution of this problem is given by $\mathbf{f} = \mathbf{P}^\dagger \mathbf{p}_{\text{in}}$ where $\dagger$ denotes the pseudoinverse (see Heath [25]). In this case, since the number of variables is huge, the analytical solution is only theoretically interesting. In practice, iterative methods must be employed. Many methods, for example the steepest descent and conjugate gradient methods (see Nocedal and Wright *et al.* [57]), exist for this purpose. The simplest method is probably the steepest descent method introduced in Section 3.1. The gradient $\nabla z(\mathbf{f})$ is given by

$$\nabla z(\mathbf{f}) = \mathbf{P}^T\mathbf{W}(\mathbf{P}\mathbf{f} - \mathbf{p}_{\text{in}}). \tag{3.18}$$

Inserted in the steepest descent update formula $\mathbf{f}_{k+1} = \mathbf{f}_k - \alpha_k \nabla z(\mathbf{f}_k)$, this yields

$$\mathbf{f}_{k+1} = \mathbf{f}_k - \alpha_k \mathbf{P}^T\mathbf{W}(\mathbf{P}\mathbf{f}_k - \mathbf{p}_{\text{in}}). \tag{3.19}$$

If the method is initialized with $\mathbf{f} = \mathbf{0}$ and the step-lengths α_k are chosen appropriately, this method converges to the solution of (3.17). That the minimum norm solution is indeed achieved is realized by looking at the update step; when $\|\sqrt{\mathbf{W}}(\mathbf{P}\mathbf{f} - \mathbf{p}_{\text{in}}\|$ is a minimum, contributions from the nullspace $N(\mathbf{P}) = R(\mathbf{P}^T)^\perp$ can be added without changing the value of $\|\sqrt{\mathbf{W}}(\mathbf{P}\mathbf{f} - \mathbf{p}_{\text{in}}\|$. Since the update step only add contributions from $R(\mathbf{P}^T)$ to the iterates, the limit point will lie precisely in $R(\mathbf{P}^T)$, while any change of components in $R(\mathbf{P}^T)^\perp$ would increase the norm $\|\mathbf{f}\|$.

In order to be a descent direction (a direction that decrease the objective $z(\mathbf{f})$), a search direction $\mathbf{d}$ must fulfill the relation

$$\mathbf{d}^T\nabla z(\mathbf{f}) < 0. \tag{3.20}$$

If $\mathbf{V}$ is a symmetric positive definite matrix, we see that not only the negative gradient $-\nabla z(\mathbf{f})$ but also $\mathbf{d} = -\mathbf{V}\nabla z(\mathbf{f})$ satisfies the condition (3.20). Therefore, the update step (3.19) can be replaced by the more general update step

$$\mathbf{f}_{k+1} = \mathbf{f}_k - \alpha_k \mathbf{V}\mathbf{P}^T\mathbf{W}(\mathbf{P}\mathbf{f} - \mathbf{p}_{\text{in}}). \tag{3.21}$$

The matrix $\mathbf{V}$ can be used to improve the rate of convergence. For instance, if $\mathbf{V} = (\mathbf{P}^T\mathbf{P})^\dagger, \mathbf{f}_0 = \mathbf{0}$ and $\alpha_0 = 1$, the method will converge to the least square minimum norm solution in only one iteration. Changing the search direction with a matrix $\mathbf{V}$ as in (3.21) is called *preconditioning*. Clinthorne *et al.* [9] showed that convergence rates for iterative reconstruction can be improved without changing the ultimate solution by preconditioning with an approximation of $(\mathbf{P}^T\mathbf{P})^\dagger$.

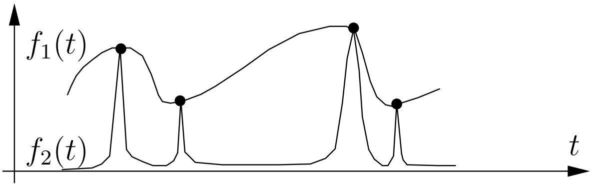

Figure 3.9: A simple example of fitting a function $f : \mathbb{R} \to \mathbb{R}$ to a number of measurements. The filled circles illustrate the measured points and the curves illustrate two possible functions f_1 and f_2 that interpolate the measured data.

The well-known SIRT is achieved if $\mathbf{V}$ and $\mathbf{W}$ in 3.21 are diagonal matrices with diagonal elements $v_j = (\sum_{i=1}^{M} p_{ij})^{-1}$ and $w_i = (\sum_{j=1}^{N} p_{ij})^{-1}$. It was shown by Jiang and Wang [30] that this method converges to the least square minimum norm solution plus a contribution depending on $\mathbf{f}_0$ for $\alpha \in (0, 2)$.

ART and SART are sequential methods in the meaning that a full update consist of a sequence of subupdates. Jiang and Wang [31] showed how such sequential methods can be expressed with formulas similar to (3.21) when $\mathbf{V}$ and $\mathbf{W}$ are positive *diagonal* matrices. It was also shown that if the parameters α_k satisfy certain conditions, these methods also converge to a least square minimum norm solution plus a contribution that depends on the initial reconstruction volume $\mathbf{f}_0$. These results will be presented in more detail in Section 3.4 when discussing convergence of the ordered subsets methods.

A common problem with iterative image reconstruction methods is that the iterates tend to become distorted by high frequency artifacts and noise as the number of iterations grows. One reason for this is that the restrictions on the space of possible reconstruction results are inappropriate. A simple example is given in Figure 3.9. The space of functions that maps the real line to itself is too large and contains many solutions that we would consider incorrect or noisy. Therefore, constraints must be added to restrict the solution space to certain wellbehaived functions. This is called *regularization.* In the context of image reconstruction, at least four different regularization techniques appear in the literature.

Bandlimiting with smooth basis functions: Since the input data have not been acquired with an infinite resolution, it seems reasonable to limit the bandwidth of the reconstruction result. One way to do this is to use basis functions that are effectively bandlimited, for instance the generalized Kaiser-Bessel functions by Lewitt [45].

Bandlimiting with sieves: Snyder and Miller [70], and Snyder *et al.* [71] proposed the use of sieves to suppress the enhancement of noise as the number of iteration is increased. This means that the iterative method is designed so that the result will lies in the sieve

$$S = \left\{ f(\mathbf{r}) : f(\mathbf{r}) = \int_{\mathbb{R}^3} K(\mathbf{r} - \mathbf{r}') f'(\mathbf{r}') d\mathbf{r}', K > 0, f' > 0 \right\} \tag{3.22}$$

where $K(\mathbf{r})$ is called the sieve kernel and is usually a smooth function, for instance a Gaussian. The iterative method is designed to estimate f' by introducing a convolution with the sieve kernel before projection as well as after backprojection in each iteration. As a final step (after convergence), f' is convolved with the sieve kernel to get f. Note that the continuous formulation (3.22) leaves room for principally different implementations. For instance, f' can be identified as the Dirac impulse train corresponding to the coefficients of the **f** vector, and K can be identified as the basis functions. Then, sieve regularization would be identical to regularization with a smooth basis function. Another, perhaps more common interpretation is to design the iterative method so that the resulting coefficient vector **f** lie in the sieve

$$S_{\text{discrete}} = \left\{\mathbf{f} \in \mathbb{R}^N : \mathbf{f} = \mathbf{K}\mathbf{f}', \mathbf{K} > 0, \mathbf{f}' \in \mathbb{R}^{N+}\right\} \tag{3.23}$$

where **K** correspond to a convolution with a discrete sieve kernel. This was implemented in combination with Joseph interpolation by De Man [49] for z-resolution constraining.

Early stopping: Since the noise level increases with increasing number of iterations, a popular method for avoiding enhancement of noise is to stop the method before the fixed point has been reached (see for instance Veklerov and Llacer [80] and Hebert *et al.* [26]). The practical problem with this method is to determine a good stopping criterion.

Penalty functions: Stopping an iterative method before convergence is theoretically unsatisfactory, since this means that a sub-optimal point is preferred over the optimal solution to the problem as it has mathematically been formulated. The conclusion is that the mathematical problem formulation lacks some feasibility parameter not yet accounted for. One way to improve the problem formulation is to add a penalty term to the objective function in (3.16). This term is designed so that certain structures and properties considered likely to appear are penalized less than other less likely structures.

One class of penalty terms is based on a Markov Random Field (MRF) model of the reconstructed image. For statistical motivation of this penalty term in a MAP reconstruction framework, see for instance Geman and McClure [20] and Liang *et al.* [47]. The new function to be minimized is given by

$$z(\mathbf{f}) = \frac{1}{2}\|\sqrt{\mathbf{W}}(\mathbf{P}\mathbf{f} - \mathbf{p}_{\text{in}})\|^2 + \beta \sum_{i=1}^{N}\sum_{j=1}^{N} d_{ij} V(f_i - f_j) \tag{3.24}$$

where

f_i are components of **f**,

d_{ij} are given by the inverse distances between the voxels i and j in a small neighborhood,

V is the so called potential functions, and

β is a parameter that determines the amount of smoothing.

Depending on the choice of potential function, this term will penalize certain local structures more than others. Figure 3.10 show examples of different potential functions. Non-quadratic potential functions are interesting because of their edge-preserving smoothing properties. Unfortunately, they result in non-linear methods with a behavior that is rather difficult to understand and interpret.

A quadratic potential function in combination with a least square term results in a linear method which follows by the following reasoning. Differentiation of (3.24) and insertion of the quadratic potential function $V(f) = f^2$ yields

$$\begin{aligned}\nabla z(\mathbf{f}) &= \mathbf{P}^T\mathbf{W}(\mathbf{Pf}-\mathbf{p}_{\text{in}}) + 2\beta \sum_{i=1}^{N}\left(\sum_{j=1}^{N} d_{ij}\frac{d}{df}V(f_i-f_j)\right)\mathbf{e}_i \\ &= \mathbf{P}^T\mathbf{W}(\mathbf{Pf}-\mathbf{p}_{\text{in}}) + 4\beta \underbrace{\sum_{i=1}^{N}\left(\sum_{j=1}^{N} d_{ij}(f_i-f_j)\right)\mathbf{e}_i}_{=:\mathbf{Rf}} \\ &= \mathbf{P}^T\mathbf{WPf} - \mathbf{P}^T\mathbf{W}\mathbf{p}_{\text{in}} + 4\beta\mathbf{Rf} \\ &= (\mathbf{P}^T\mathbf{WP} + 4\beta\mathbf{R})\mathbf{f} - \mathbf{P}^T\mathbf{W}\mathbf{p}_{\text{in}} \qquad (3.25)\end{aligned}$$

where $\mathbf{R}$ is given by

$$\mathbf{R} = \begin{pmatrix} \sum_{j=1}^N d_{1j} - d_{11} & -d_{12} & \cdots & -d_{1N} \\ -d_{21} & \sum_{j=1}^N d_{2j} - d_{22} & & \\ \vdots & & \ddots & \vdots \\ -d_{N1} & \cdots & & \sum_{j=1}^N d_{Nj} - d_{NN} \end{pmatrix}. \qquad (3.26)$$

Hence, the analytical expression

$$\mathbf{f}^* = (\mathbf{P}^T\mathbf{WP} + 4\beta\mathbf{R})^{\dagger}\mathbf{P}^T\mathbf{W}\mathbf{p}_{\text{in}} \qquad (3.27)$$

for the minimizer of $z(\mathbf{f})$ reveals that the optimum depends linearly on the input data $\mathbf{p}_{\text{in}}$.

In practice, the minimization of the penalized least square problem can be done using the same techniques as for the non-penalized. The term $4\beta\mathbf{Rf}$ grows linearly with the total number of voxels. Therefore, the additional computational cost due to this term is neglectable in comparison with the projection and backprojection operations.

3.4 Ordered subsets acceleration

The ordered subsets technique for emission tomography was introduced in 1994 by Hudson and Larkin [29]. They showed that this technique could improve the rate of convergence for the emission tomography MLEM algorithm [67] with at least a factor 16 without any appreciable loss of image quality. Later, the ordered subsets technique was applied to algorithms for transmission tomography by Kamphuis and Beekman [36] and Erdogan and Fessler [19].

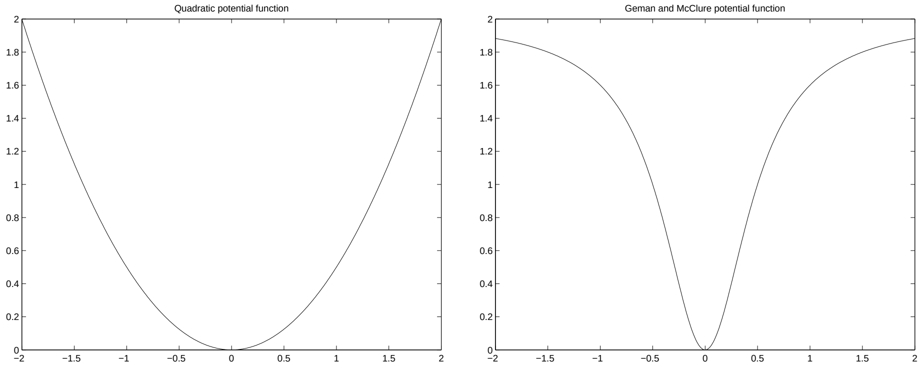

(a) $V(f) = f^2$ (b) $V(f) = \frac{f^2}{f^2+\delta^2}$

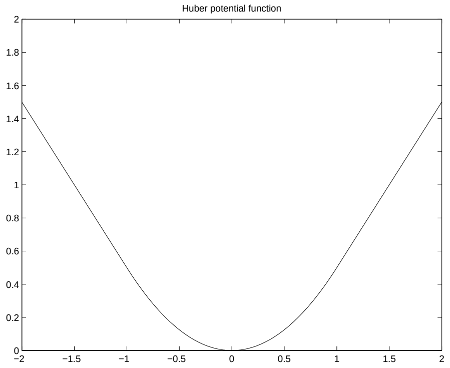

(c) $V(f) = \begin{cases} \frac{f^2}{2\delta^2} & |f| \leq \delta \\ \frac{|f|-\delta/2}{\delta} & |f| > \delta \end{cases}$

Figure 3.10: Three examples of potential functions. (a) The quadratic prior produces smooth images without any edge preservation. It has the advantage of being convex and results in a linear method when combined with a least square data term. (b) This non-convex edge preserving prior was proposed by Geman and McClure [20]. (c) The Huber prior has the advantage of being both edge preserving and convex.

Simultaneous update mode:

$\mathbf{p}_{\text{in}} = (\mathbf{p}_{\theta_1}, \mathbf{p}_{\theta_2}, \mathbf{p}_{\theta_3}, \mathbf{p}_{\theta_4}, \mathbf{p}_{\theta_5}, \mathbf{p}_{\theta_6}, \mathbf{p}_{\theta_7}, \mathbf{p}_{\theta_8})$

Ordered subsets mode:

$\mathbf{p}_{\text{in},1} = (\mathbf{p}_{\theta_1}, \mathbf{p}_{\theta_3}, \mathbf{p}_{\theta_5}, \mathbf{p}_{\theta_7})$

$\mathbf{p}_{\text{in},2} = (\mathbf{p}_{\theta_2}, \mathbf{p}_{\theta_4}, \mathbf{p}_{\theta_6}, \mathbf{p}_{\theta_8})$

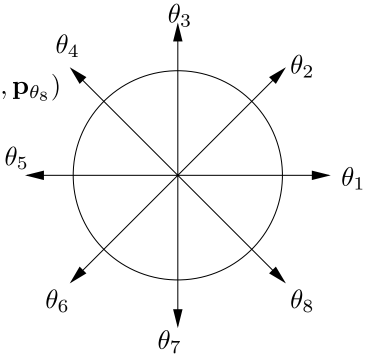

Figure 3.11: Simple illustration with only 8 projection angles for illustrating the ordered subsets technique. Here, each arrow represents a parallel projection angle θ. A simultaneous method would use all projection data $\mathbf{p}_{\text{in}}$ in each update. In an ordered subsets method, the full update would be split into two partial updates, first with $\mathbf{p}_{\text{in},1}$ and then with $\mathbf{p}_{\text{in},2}$.

Mathematical descriptions and proofs of convergence for sequential methods such as ART, SART and OS methods were given by Jiang and Wang [31]. Here we give a simple presentation of the ordered subsets technique as it is used in tomographic reconstruction and repeat one of the main results from [31].

First, the input data $\mathbf{p}_{\text{in}}$ are partitioned into equidistantly sampled subsets $\mathbf{p}_{\text{in},l}, l = 1, ..., L$ with respect to the rotation angle θ (see Figure 3.11). Now, presuming that $\mathbf{W}$ does not mix data between these subsets, we can define new matrices $\mathbf{W}_l$, $\mathbf{P}_l$ and $\mathbf{P}_l^T$ acting only on the subsets. With an index sequence $\{i_k\}_{k=1}^{\infty}$ specifying the order in which the subsets shall be applied, the update step becomes

$$\mathbf{f}_{k+1} = \mathbf{f}_k + \alpha_k \mathbf{V}\mathbf{P}_{i_k}^T \mathbf{W}_{i_k}(\mathbf{P}_{i_k}\mathbf{f}_k - \mathbf{p}_{\text{in},i_k}). \tag{3.28}$$

In the case of disjoint subsets, Jiang *et al.* showed that if the index sequence is periodic, *i.e.* $i_{k+nL} = i_k, n \in \mathbb{N}$, and the step lengths α_k satisfy the conditions

$$\lim_{k\to\infty} \alpha_k = 0, \text{ and } \sum_{k=0}^{\infty} \alpha_k = +\infty, \tag{3.29}$$

then the method defined by (3.28) converge toward a minimum norm minimizer of $\|\sqrt{\mathbf{W}}(\mathbf{P}\mathbf{f} - \mathbf{p}_{\text{in}})\|^2$ plus an oblique projection of the initial image $\mathbf{f}_0$ on the null space $N(\mathbf{P}) = R(\mathbf{P}^T)^{\perp}$.

Although the above result holds independently of subset ordering, this ordering affects the rate of convergence. Therefore it is of interest to find an ordering scheme that minimizes the number of necessary iterations. Different ordering schemes will be presented and explored in Section 6.

3.5 Iterative filtered backprojection (IFBP) methods

The IFBP method in its most basic form is given by

$$\mathbf{f}_{k+1} = \mathbf{f}_k - \alpha_k \mathbf{Q}(\mathbf{P}\mathbf{f}_k - \mathbf{p}_{\text{in}}). \tag{3.30}$$

where $\mathbf{Q}$ is the matrix representation of an analytical reconstruction method. Formula (3.30) differs from the Landweber method (3.1) in that the adjoint projection operator matrix $\mathbf{P}^T$ has been replaced with the analytical reconstruction operator matrix $\mathbf{Q}$. This is motivated by the fact that an analytical reconstruction method produces a result that resembles the original object to be reconstructed much more than a result produced by $\mathbf{P}^T$. Therefore, it is likely that an IFBP method would converge much faster than the Landweber method.

In the following, we will study the more general IFBP method defined by

$$\mathbf{f}_{k+1} = \mathbf{f}_k - \alpha_k \mathbf{Q}(\mathbf{P}\mathbf{f}_k - \mathbf{p}_{\text{in}}) - \alpha_k \beta \mathbf{R}\mathbf{f}_k. \tag{3.31}$$

Here, the matrix $\mathbf{R} \in \mathbb{R}^{N\times N}$ is the same matrix as the one introduced and motivated for least squares methods in (3.24), (3.25) and Figure 3.10.This can be used to reduce unwanted enhancement of high frequencies in the final result.

Here follows a convergence discussion similar to the convergence discussion for the Landweber method in the beginning of Section 3.1. This discussion was mainly inspired by the similar discussion for the non-regularized case in [85]. Suppose that $\alpha_k = \alpha$ is constant with respect to k and let

$$\mathbf{\Delta} = \mathbf{I} - \alpha(\mathbf{Q}\mathbf{P} + \beta\mathbf{R}). \tag{3.32}$$

If the eigenvalues of the matrix $\mathbf{\Delta}$ are contained in the interior of the unit circle $\{\lambda \in \mathbb{C} : |\lambda| < 1\}$, or equivalently

$$|\text{eig}(\alpha(\mathbf{Q}\mathbf{P} + \beta\mathbf{R})) - 1| < 1, \tag{3.33}$$

then

$$\begin{aligned}
\mathbf{f}_{k+1} &= \mathbf{f}_k - \alpha\mathbf{Q}(\mathbf{p}_{\text{in}} - \mathbf{P}\mathbf{f}_k) - \alpha\beta\mathbf{R}\mathbf{f}_k \\
&= \mathbf{f}_k - \alpha(\mathbf{Q}\mathbf{P} + \beta\mathbf{R})\mathbf{f}_k + \alpha\mathbf{Q}\mathbf{p}_{\text{in}} \\
&= \mathbf{\Delta}\mathbf{f}_k + \alpha\mathbf{Q}\mathbf{p}_{\text{in}} \\
&= \mathbf{\Delta}^2\mathbf{f}_{k-1} + (\mathbf{\Delta} + \mathbf{I})\alpha\mathbf{Q}\mathbf{p}_{\text{in}} \\
&\;\vdots \\
&= \mathbf{\Delta}^{k+1}\mathbf{f}_0 + (\mathbf{\Delta}^k + \mathbf{\Delta}^{k-1} + \cdots + \mathbf{I})\alpha\mathbf{Q}\mathbf{p}_{\text{in}} \\
&\overset{k\to\infty}{\longrightarrow} (\mathbf{I} - \mathbf{\Delta})^{-1}\alpha\mathbf{Q}\mathbf{p}_{\text{in}} = (\mathbf{Q}\mathbf{P} + \beta\mathbf{R})^{-1}\mathbf{Q}\mathbf{p}_{\text{in}}.
\end{aligned} \tag{3.34}$$

When no regularization is present, *i.e.* $\mathbf{R} = \mathbf{0}$, there are a number of cases when the nullspace $N(\mathbf{Q}\mathbf{P})$ is nonempty and equality holds in (3.33). For instance, this happens when the number of voxels is chosen to be larger than the total number

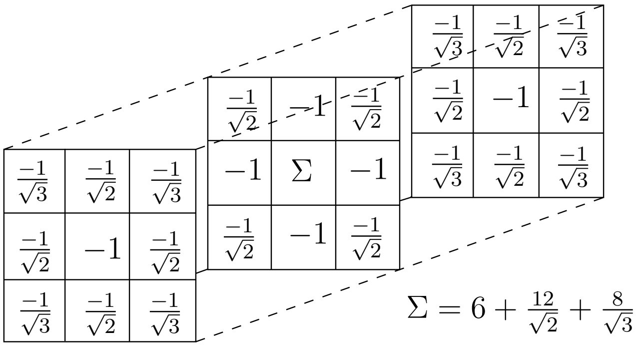

Figure 3.12: Illustration of the 3-D convolution kernel corresponding to the regularization matrix $\mathbf{R}$.

of detector readings in order to preserve all information contained in the input data. In this case $N(\mathbf{P}) \neq \emptyset$ and the sum in (3.34) would diverge. However, the following argument suggests that this convergence problem can be solved with the regularization term $\mathbf{Rf}$ from Equation (3.25). Since the nonempty nullspace of $\mathbf{P}$ arises when the voxel density is increased above a certain level, this nullspace must consist of high-frequency structures. By inspection of equation (3.25), we see that multiplication with $\mathbf{R}$ is equivalent to convolution with the kernel illustrated in Figure 3.12, *i.e.* a high-pass filter. It is therefore unlikely that the matrix $(\mathbf{QP} + \beta\mathbf{R})$ would have a non-empty nullspace.

Zeng and Gullberg [85] numerically investigated the property (3.34) for a number of operators $\mathbf{Q}$ that can be used for single photon emission computed tomography (SPECT). Under the assumption that $\mathbf{QP}$ was symmetric, its smallest eigenvalue was found by using the power method (see [25]). For the initial 500 iterations, the normalized mean square error was also studied and it was concluded that a ramp filter can be used to reduce the number of iterations by an order of magnitude. However, the WFBP method used in the following chapters differs from the transposed projection operator $\mathbf{P}^T$ with respect to interpolation and normalization so that $\mathbf{QP}$ becomes non-symmetric. Because of this and differences between x-ray CT and SPECT, the results from this paper are not directly transferable to the methods studied in the following chapters.

Chapter 4

Simulation and evaluation

4.1 Generation of input projection data

Noise-free input data for the experiments in the later Chapters 5, 6 and 7 were generated with the CTSIM program package (Siemens Medical, Forchheim). This program takes scanning parameters and a mathematical description of a phantom as input data. It simulates the finite extension of focus and detector by dividing these into $N_{\text{sub}-\text{xy}} \times N_{\text{sub}-\text{z}}$ and $N_{\text{sub}-\text{ch}} \times N_{\text{sub}-\text{rows}}$ equidistantly sampled points respectively (see Figure 4.1), and calculating a mean of line integrals instead of just one single line integral. To make the physical model more realistic, modeling of the gantry rotation have been added. Thus, CTSIM in combination with the additional gantry rotation model calculates the contributions after taking logarithms as

$$p_i = -\log\left(\frac{1}{N}\sum_{j=1}^{N}\exp\left(-\int_{\Gamma_{i,j}} f_{\text{pha}}(\mathbf{r})dl\right)\right) \tag{4.1}$$

where

$$N = N_{\text{sub}-\text{xy}} \times N_{\text{sub}-\text{z}} \times N_{\text{sub}-\text{ch}} \times N_{\text{sub}-\text{rows}} \times N_{\text{sub}-\alpha}. \tag{4.2}$$

As shown in Table 4.1, typically $N = 3^5 = 243$, which makes the computation of these simulated projection data very heavy. However, since the same input data can be used for several different experiments, this is not a problem in practice.

Noise were added using the procedure suggested by Fuchs [18]. Let I_0 be the expected number of non-attenuated photons traveling along the ray i from Equation (4.1). Then, the number of attenuated photons I is approximately Poisson distributed with

$$E[I] = Var[I] = I_0 k, \tag{4.3}$$

where $k = \exp(-p_i)$. When this number is large, the distribution of I is approximately Gaussian with variance k and standard deviation $\sqrt{k}$. Then, a noisy

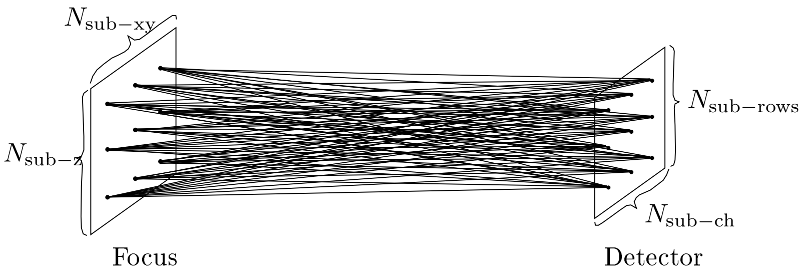

Figure 4.1: In order to realistically simulate the physical acquisition process, both focus and detector are divided into subunits. The final contribution is calculated as the mean of all sub-contributions.

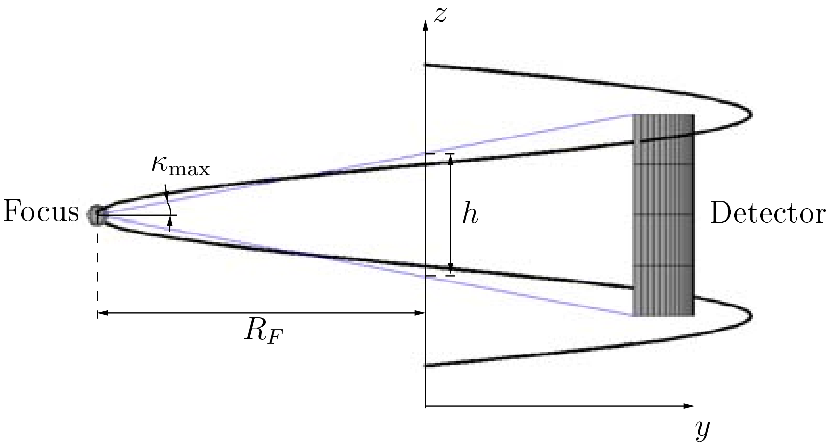

Figure 4.2: Explanation of some of the scanning geometry parameters in Table 4.1.

contribution $\tilde{p}_i$ can be calculated as

$$\tilde{p}_i = -\log\left(k + \sqrt{k}N\left(0, \frac{1}{\sqrt{I_0}}\right)\right). \tag{4.4}$$

where $N(\mu, \sigma)$ is a sample from the Gaussian distribution with expectation μ and standard deviation σ.

The scanning parameters for the experiments in Chapter 5 to 7 are given by Table 4.1, and an illustration of the geometry and corresponding parameters is shown in Figure 4.2. In some cases, two-dimensional rather than three-dimensional experiments have been performed. In these cases, all parameters regarding lengths in the z-direction have been set to zero and the number of rows have been reduced to one.

As a first step in all experiments presented in this treatise, input data are rebinned to semi-parallel geometry. In the rebinning process, new parameters describing sampling in the new semi-parallel geometry are introduced. These pa-

Table 4.1: Scanning parameters for experiments in Chapter 5 to 7.

Source-Isocenter distance	R_F	570mm
Number of channels (Quarter offset)	N_{ch}	336
Number of rows	N_{rows}	64
Number of projections per turn	N_{proj}	580
Detector subsampling in channel dir.	$N_{\text{sub-ch}}$	3
Detector subsampling in row dir.	$N_{\text{sub-row}}$	3
Focus subsampling along xy-plane	$N_{\text{sub-xy}}$	3
Focus subsampling in z-dir	$N_{\text{sub-z}}$	3
Angle subsampling	$N_{\text{sub-}\alpha}$	3
Focus width (xy)	w_f	1.3mm
Effective focus length (z)	l_f	1.2mm
Slicewidth	S	1.5mm
Detector height	h	$S \times N_{\text{rows}} = 96\text{mm}$
Table-feed	P	96mm
Maximal fan angle	$\beta_{\max}$	26°
Maximal cone angle	$\kappa_{\max}$	$\frac{180}{\pi} \times \tan^{-1}\left(\frac{h/2}{R_F}\right) \approx 4.8°$

Table 4.2: Parameters introduced in the rebinning step.

Number of channels	N_t	672
Number of projections	N_θ	580
Parallel displacement per channel	Δ_t	$\frac{\pi R_F \beta_{\max}}{180 N_{\text{ch}}} \approx 0.77\text{mm}$
Maximal parallel displacement	$t_{\max}$	$\frac{N_t \Delta_t}{2} \approx 259\text{mm}$

rameters are shown in Table 4.2. The alternative would be to move the rebinning step forward and include this process in the reconstruction operator **Q**. As a consequence the projection operator **P** should be redesigned to generate true cone-beam data. This possibility is investigated in Section 5.5.

4.2 Phantoms and error measurements

In earlier experiments, the Turbells clock phantom [77] was used because of its ability to reveal the effects of non-exactness in a cone-beam reconstruction algorithm, the so-called cone artifacts. This phantom has now been replaced by the Thorax phantom by Sourbelle [72] since the thorax phantom contains more complex shapes including edges and corners. Besides emphasizing cone artifacts, such shapes are more likely to produce streak artifacts and non-linear partial volume artifacts existing already in 2D-reconstruction. The Thorax phantom is illustrated in Figure 4.3 and 4.4. The sharp transitions in the z-direction near the vertebra borders usually give rise to severe cone artifacts when reconstructed with non-exact methods at high cone angles.

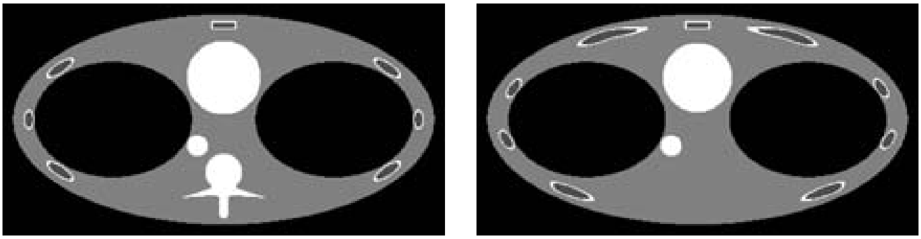

(a) $z = 0$mm (b) $z = -12$mm

(c) $y = -48$mm (d) $x = -33$mm

Figure 4.3: Four different slices of the thorax phantom. The greyscale window is ±50 HU. The first row consists of two axial slices at different z-levels. The right slice is located close to the border of one vertebra. Non-exactness in a reconstruction algorithm usually results in cone artifacts in this area. The bottom row show coronal and saggital slices respectively.

Under certain circumstances, the iterative experiments to be reported in the following sections give rise to high-frequent low-contrast artifacts. To study these artifacts, a low contrast phantom by Schaller [64], scaled to twice its original size, was used. This phantom is shown in Figure 4.5.

For each reconstructed result presented in the following chapters, the deviation from the original phantom has been calculated as the root mean squared error (RMSE)

$$\sigma_e = \sqrt{\frac{1}{|\Omega|}\sum_{i\in\Omega}((\mathbf{f}_{\text{rec}})_i - (\mathbf{f}_{\text{phan}})_i)^2}. \tag{4.5}$$

Here, $\mathbf{f}_{\text{phan}}$ is a vector containing sampled values of the original phantom and Ω is the set of voxels taken into account for the measurement. Depending on how this set is chosen, different types of deviation are measured. For instance, if high-contrast edges are included in Ω, σ_e will be dominated by errors caused by smoothing of edges. Figure 4.6 shows two different sets that have been considered for the thorax and low-contrast phantom, one for measuring the amount of cone artifacts, the other for measuring the overall RMSE. RMSE measurements for the low contrast phantom were calculated using all voxels except those located close to or outside the cylinder edge.

Noise in the reconstructed images was calculated with the formula

$$\sigma_n = \sqrt{\frac{1}{|\Omega|}\sum_{i\in\Omega}((\mathbf{f}_{\text{noisy}})_i - (\mathbf{f}_{\text{noise-free}})_i)^2} \tag{4.6}$$

where $\mathbf{f}_{\text{noisy}}$ represents a reconstruction from noisy data and $\mathbf{f}_{\text{noise-free}}$ represents a reconstruction from noise-free data. In the same way as for equation (4.5),

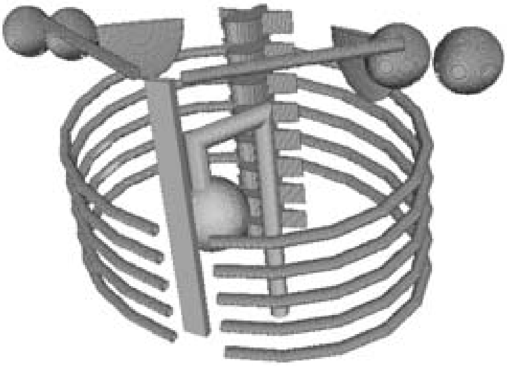

Figure 4.4: Illustration of the thorax phantom. This image was created from a sampled voxel volume by a program called MCIV (Matlab Connecting ITK and VTK) developed by Larsson *et al.* [44].

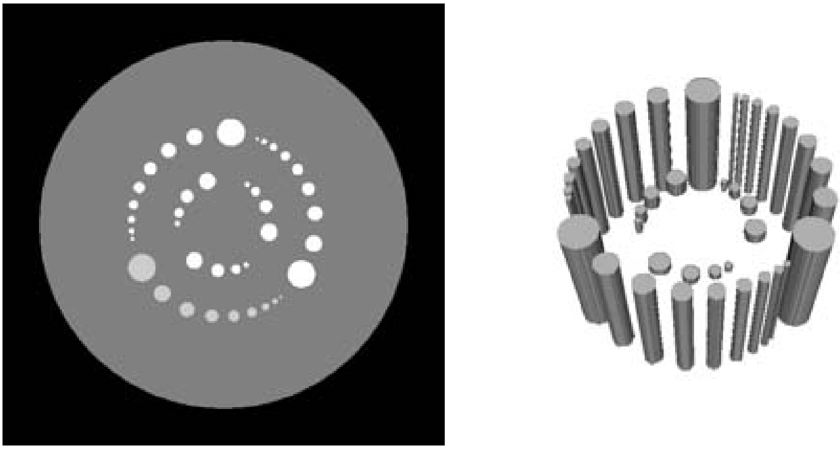

Figure 4.5: Illustration of the low contrast phantom. The left image shows an axial section of the phantom at $z = 0$mm with a greyscale window of ±10HU. The right image is a 3D-view created by MCIV (see Figure 4.4).

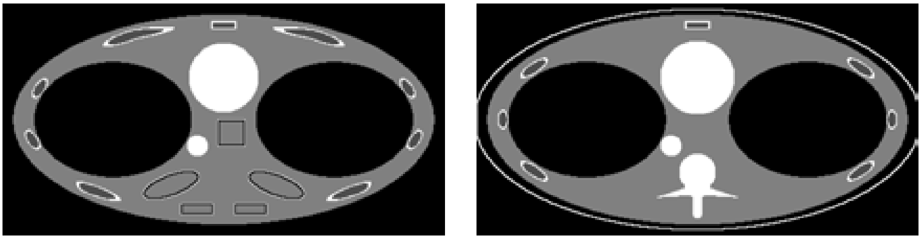

(a) Original phantom, $z = -12$mm
"Cone artifact areas" indicated in lower middle part of the image

(b) Original phantom, $z = 0$mm
"Whole image area" indicated

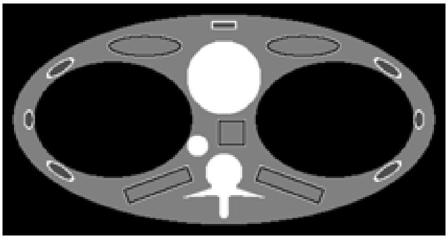

(c) Original phantom, $z = 0$mm
Areas for noise measurements indicated

Figure 4.6: The marked areas show different Ω sets for measuring the error σ_e and σ_n. The cone artifact areas in (a), consisting of one square, two ellipses, and two rectangles, are designed for measuring presence of cone artifacts. The whole image area in (b) measures the error over the whole image. The area for noise measurement in (c) consists of one square, two ellipses and two rectangles. Depending on the reconstruction resolution, these sets extend over one to five slices in the z-direction. The difference in z between (a) and (b) stems from the fact that cone artifacts arise at $z = 12$mm but not at $z = 0$mm. For *two-dimensional* experiments, (c) is used both for measuring σ_e and σ_n.

Ω is the set voxels, which over the summation takes place. The sets used for noise measurements are shown in Figure 4.6c. These sets are also used for σ_e measurements in two-dimensional experiments.

Even if the purpose of the iterative methods studied in the following chapters is to produce good results after few iterations, it is interesting to see what the methods deliver after many iterations. Besides error and noise measures described above, we have calculated the Euclidean norm

$$\|\mathbf{Q}\mathbf{p}_{\text{in}} - (\mathbf{Q}\mathbf{P} + \beta\mathbf{R})\mathbf{f}_k\| = \|\mathbf{f}_{k+1} - \mathbf{f}_k\|. \tag{4.7}$$

Obviously, a necessary condition for the iterative method to converge is that this norm tends to zero as $k \to \infty$.

4.3 Spatial resolution

Images reconstructed by analytical and iterative methods respectively differ in many ways *e.g.* in sensitivity to noisy input data. Another feature, which often can be traded for noise is the ability to preserve high frequencies throughout the reconstruction (high spatial resolution). This section describes how spatial resolution can be and has been experimentally measured in the experiments to be found in the following chapters. We will make a difference between spatial resolution in the xy-plane, represented by modulation transfer functions (MTFs), and spatial resolution in the z-plane, represented by slice sensitivity profiles (SSPs).

The method that has been used to measure the MTF of the virtual CT and its reconstruction algorithm is called the edge method and was first presented by Judy [33]. It is based on the assumption that the MTF is space invariant or at least only slowly varying in space. A phantom containing a sharp edge, is slightly tilted to form angle γ with the x-axis as illustrated in Figure 4.7. By measuring points along the x-axis, in the reconstructed result, we obtain an oversampled edge response of the system. The amount of oversampling is determined by the value of γ. In the MTF measurements, we used an angle of $\gamma = 3°$. From the edge response, the line spread function (LSF) is obtained by differentiation. This differentiation was made by simple central difference calculations instead of the least square line fitting described by Judy [33]. This can be justified by looking at the oversampling density, which is almost 20 times higher than the image matrix sampling density. Thus, the errors introduced by differentiation are not likely to affect the area where the MTF exceeds 10% of its maximum value. Finally, the MTF is calculated as the modulus of the Fourier transform of the LSF.

In the books by Hsieh [28] and Kalender [35], the wire method is presented as a standard method for measuring MTFs. Unfortunately, this method requires reconstruction to a fine grid, often finer than what is used in practice. In iterative methods, the MTF is dependent on the image matrix resolution (see Chapter 5). Therefore, to enable studies of MTFs also at lower image matrix resolutions, the edge method was chosen in favor of the wire method.

The *slice sensitivity profile* (SSP) is the tomographic system response in the z-direction. For helical CT, so called delta phantoms are used for measuring the SSP

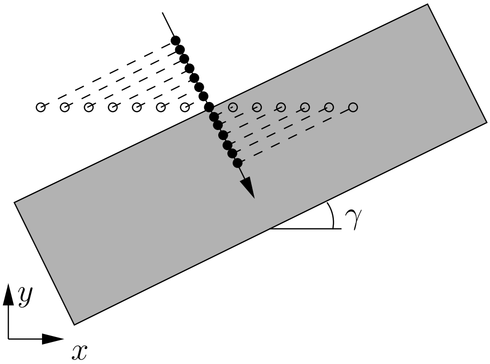

Figure 4.7: Illustration of the edge method. If the edge response does not vary along the edge, an oversampled edge response can be obtained by sampling along the x-axis. The angle γ is exaggerated here. In the experiments presented later, a value of 3° was used.

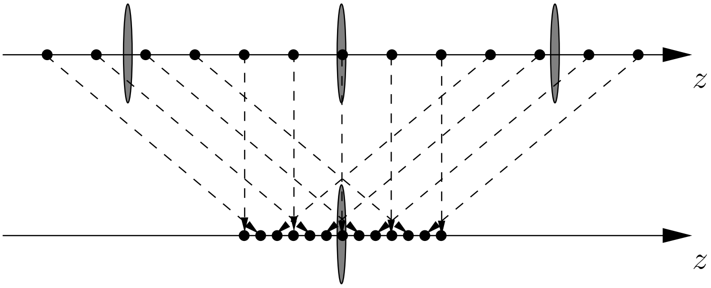

Figure 4.8: Measurement of the SSP of a system. By merging responses from a number of discs, whose exact positions are known, an oversampled SSP is obtained.

[35]. Again, such measurements require extra high resolution. Hence, proper SSP measures are difficult to obtain in our experiments on iterative methods, where the SSPs are dependent on the resolution. We have circumvented this problem by assuming that the SSP in the isocenter does not vary in the z-direction, and using a phantom consisting of a number of very thin (0.2mm) discs. Since the exact location of each disc is known, measurements from all discs can be merged (see Figure 4.8) into one oversampled SSP.

4.4 Noise versus spatial resolution

Let ρ be the highest frequency the tomographic system is able to reconstruct in the xy-plane, and let S be the slice thickness of the system. It was shown by Brooks and Di Chiro [6] that the variance σ^2 of the reconstructed voxels is related to ρ and S as

$$\sigma^2 \propto \frac{1}{\rho^{-3}S}. \tag{4.8}$$

Furthermore, due to the Poisson nature of the photon density, the variance in the reconstruction result is related to the dose D (attenuated energy per mass unit) as

$$\sigma^2 \propto \frac{1}{D}. \tag{4.9}$$

These relations imply that the factor $\sigma^2\rho^{-3}SD$ should be constant for a tomographic system. Clearly, given the same dose and resolution requirement, a system that can produce an image with a lower noise level must be better than another system producing noisier images. This is the motivation for the figure of merit

$$Q_1 = \frac{c}{\sigma^2\rho_{10\%}^{-3}SD}. \tag{4.10}$$

presented by Kalender [35]. Here, $\rho_{10\%}$ is the frequency where the MTF has dropped to 10% of its maximum value, and c is an arbitrary scaling factor. An alternative to this ρ is the mean value

$$\rho_M = \frac{\rho_{10\%} + \rho_{50\%}}{2} \tag{4.11}$$

resulting in the figure of merit

$$Q_2 = \frac{c}{\sigma^2\rho_M^{-3}SD}. \tag{4.12}$$

In our experiments accounted for in the following chapters, c and D will be ignored, since these entities are constant during each comparison. It turns out that direct WFBP differs from IWFBP both with respect to noise σ and spatial resolution (ρ, S). The Q_1- and Q_2−value might allow for an investigation of whether a certain increase of both noise and spatial resolution is reasonable (Q_1 and Q_2 remain unchanged), or if it corresponds to a significant change of available information (Q_1 and Q_2 are changed).

We have also examined the quality of the reconstruction results by finding and employing regularization parameters $\beta\mathbf{R}$ that leave the spatial resolution unaffected by the iterative procedure. Clearly, this allows for noise comparisons at constant spatial resolution.

Chapter 5

Iterative Weighted Filtered Backprojection (IWFBP)

5.1 Introduction

In this chapter, we investigate the possibility to use an iterative scheme for reducing cone artifacts caused by the non-exact weighted filtered backprojection (WFBP) reconstruction method.

The procedure is illustrated in Figure 5.1. As an initial step, input data $\mathbf{p}_{\text{in}}$ are rebinned to semi-parallel geometry with double resolution in the radial direction as described in Section 2.2, resulting in $\mathbf{p}_{\text{reb}}$. This means that the projection and backprojection operators in the iterative scheme are working only on semi-parallel projection data. The rest of the method is principally the same as the IFBP method described in Section 3.5, with the matrix $\mathbf{Q}$ being equal to matrix representation $\mathbf{Q}_{\text{WFBP}}$ of the WFBP method without the initial rebinning step. As described in Section 2.2, the detector rows are down-weighted near the border of the detector. The Q-factor characteristic for this down-weighting is 0.7 throughout this chapter. Assuming that the method is initialized with $\mathbf{f}_0 = \mathbf{0}$, and that the iterates $\mathbf{f}_0, ..., \mathbf{f}_k, k \in \{0, 1, ...\}$ have been calculated, the next iterate is calculated as

$$\mathbf{f}_{k+1} = \mathbf{f}_k - \alpha_k \mathbf{Q}_{\text{WFBP}}(\mathbf{P}\mathbf{f}_k - \mathbf{p}_{\text{reb}}) - \alpha_k \beta \mathbf{R}\mathbf{f}_k \tag{5.1}$$

where $\mathbf{P}$ is the Joseph projection operator (see Section 3.2.2), and $\mathbf{R}$ is the matrix representation of the linear operation

$$\sum_{i=1}^{N} \left(\sum_{j=1}^{N} d_{ij}(f_i - f_j) \right) \mathbf{e}_i \tag{5.2}$$

from Equation (3.25).

The main body of experiments in this Chapter are motivated by results presented by Sunnegårdh *et al.* already in [76] and shown in Figure 5.2. The test

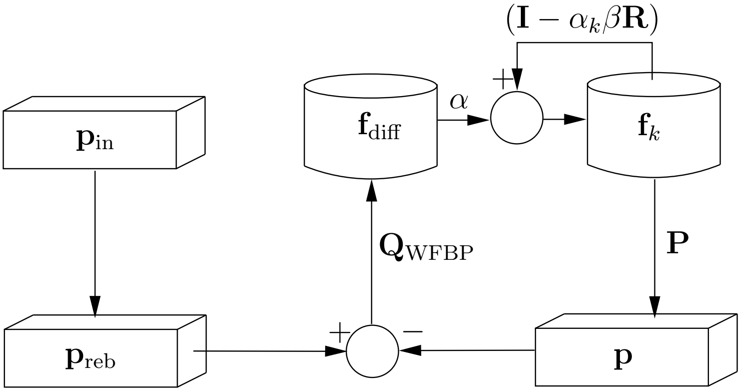

Figure 5.1: Illustration of the IWFBP method. Given the iterates $\mathbf{f}_0, \mathbf{f}_1, ..., \mathbf{f}_k$, the updated image is calculated as follows. First, the projections $\mathbf{P}\mathbf{f}_k$ are calculated and subtracted from the input data $\mathbf{p}_{\text{reb}}$. The difference $\mathbf{p}-\mathbf{P}\mathbf{f}_k$ is then reconstructed using $\mathbf{Q}_{\text{WFBP}}$. From this difference image, the result $\beta\mathbf{R}\mathbf{f}_k$ is subtracted. A final scaling with α_k is then made before addition to the previous iterate.

object is Turbell´s clock phantom [77] and the cone angle is ±9°. A clear suppression of the artifacts caused by WFBP can be observed after one iteration in Figure 5.2b. The IWFBP method was also accelerated with the ordered subsets technique (see Section 3.4 and the next chapter). With this technique, the cone artifacts were almost perfectly suppressed after one single iteration (see Figure 5.2c). However, the ability to handle inconsistent data due to noise, and low contrast properties were not examined in [76].

In the next section, we investigate the behavior of the IWFBP method with and without regularization as a function of the number of iterations. Noisy input data are generated as described in Section 4.1. The investigations are designed to address the following salient questions.

- How much will the image quality improve during the first few iterations?
- Will the method converge?
- Will the noise level increase?

From Section 3.5, we know that if the method converges, the limit point is given by

$$\mathbf{f}_\infty = (\mathbf{Q}\mathbf{P} + \beta\mathbf{R})^{-1}\mathbf{Q}\mathbf{p}_{\text{in}}. \tag{5.3}$$

Unfortunately, this expression is difficult to interpret, and an experimental evaluation is needed. It turns out that the iterative procedure does not only suppress cone artifacts, but also changes the spatial resolution and noise properties of the reconstruction results. Therefore, it is of interest to compare these new properties with those of the non-iterative WFBP method. This is done in Section 5.3.

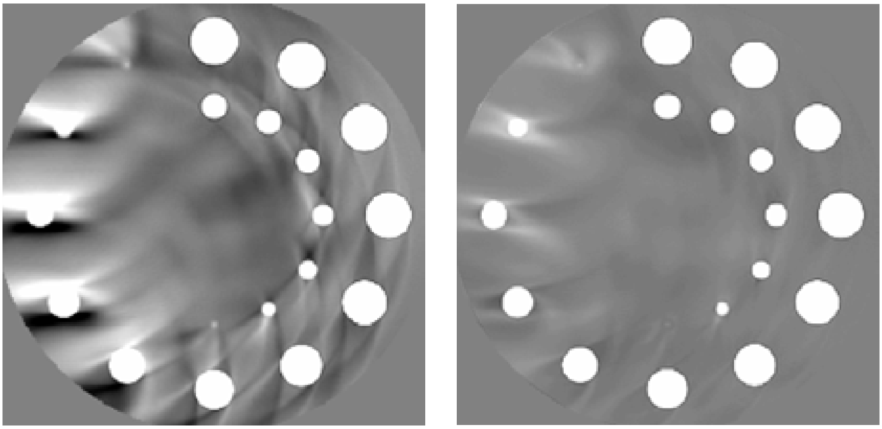

(a) WFBP reconstruction

(b) IWFBP after one iteration

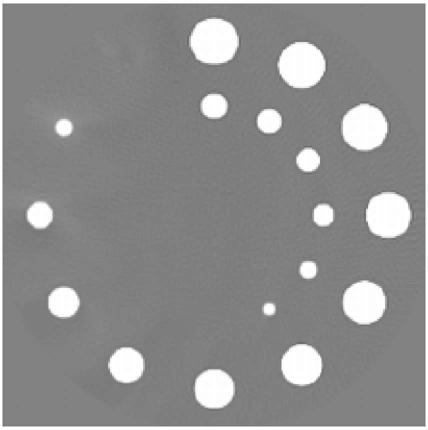

(c) OS-IWFBP after one iteration

Figure 5.2: Three reconstructions of the Turbell clock phantom. The cone angle is ±9°. Grey scale window: $[-1050, -950]$ HU.

In Section 5.4, reconstructions of the low contrast phantom from Section 4.2 are studied with a very narrow grey scale window.

5.2 Cone artifact reduction and convergence

In the experiments presented here, noisy input data were used for IWFBP reconstruction to a 513^3 volume with dimensions $L_x = L_y = 500$mm and $L_z = 387$mm. Thus, corresponding sampling distances are $\Delta_x = \Delta_y \approx 0.98$mm and $\Delta_z \approx 0.75$mm. For comparison we investigated a non-regularized method ($\beta = 0$ in the last term of Equation 5.1) as well as a regularized method with $\beta = 0.0005$. Most cone artifact reduction takes place within the first five iterations. However, to investigate the stability of the methods and to see how the reconstructions change over time, up to 40 iterations were calculated.

Figure 5.3, 5.4 and 5.5 show result images from the first six iterations. It is clear from these images that the cone artifacts present in $\mathbf{f_1}$ to a large extent are suppressed after one iteration and hardly recognizable after five iterations.

As the number of iterations increases for the non-regularized IWFBP, we observe not only suppression of cone artifacts, but also an increase of overshoots, spatial resolution, and noise. Fortunately, by choosing an appropriate value for the regularization parameter β, the frequency and noise characteristics of the original WFBP method can be approximately preserved. This is demonstrated in the right columns of Figure 5.3 and 5.5 showing results from IWFBP with $\beta = 0.0005$.

The quantity $\|\mathbf{f}_{k+1} - \mathbf{f}_k\|$ can be used as an indicator of convergence (or divergence) since the sequence $\{\mathbf{f_0}, \mathbf{f_1}, ...\}$ converges only if $\|\mathbf{f}_{k+1} - \mathbf{f}_k\| \to 0$. In Figure 5.6, the update norms $\|\mathbf{f}_{k+1} - \mathbf{f}_k\|$ calculated over "whole image" is shown. For the non-regularized IWFBP, the norm is reduced to about 1/30 in the first five iterations. However, even after 40 iterations the norm does not fall below 1/50 of the first iteration. Therefore, it is difficult to tell anything about the convergence in the unregularized case. In contrast, the corresponding norm of the regularized IWFBP with $\beta = 0.0005$ falls down to 1/50th in the first five iterations and continues to drop down to 1/100000th after 30 iterations. After 30 iterations, no further reduction can be observed. What remains is so little that it may depend on the finite precision in the calculation. We therefore conclude that the regularized method converges to its fixed point after approximately 30 iterations.

Figure 5.7c shows the RMSEs, that is

$$\sigma_e = \sqrt{\frac{1}{|\Omega|}\sum_{i\in\Omega}((\mathbf{f}_{\text{rec}})_i - (\mathbf{f}_{\text{phan}})_i)^2} \tag{5.4}$$

calculated over the cone artifact measurement set shown in Figure 4.6c (repeated in Figure 5.7a). Even if the RMSE does not only measure cone artifacts, but also noise and aliasing artifacts, the initial reduction for the non-regularized IWFBP is due to diminishing cone artifacts. After a few iterations, however the noise and aliasing artifacts are amplified, resulting in an increasing RMSE. For the regularized IWFBP, the cone artifact mask RMSE drops during the first seven iterations and then remains practically unchanged. Figure 5.7d shows the RMSE of the

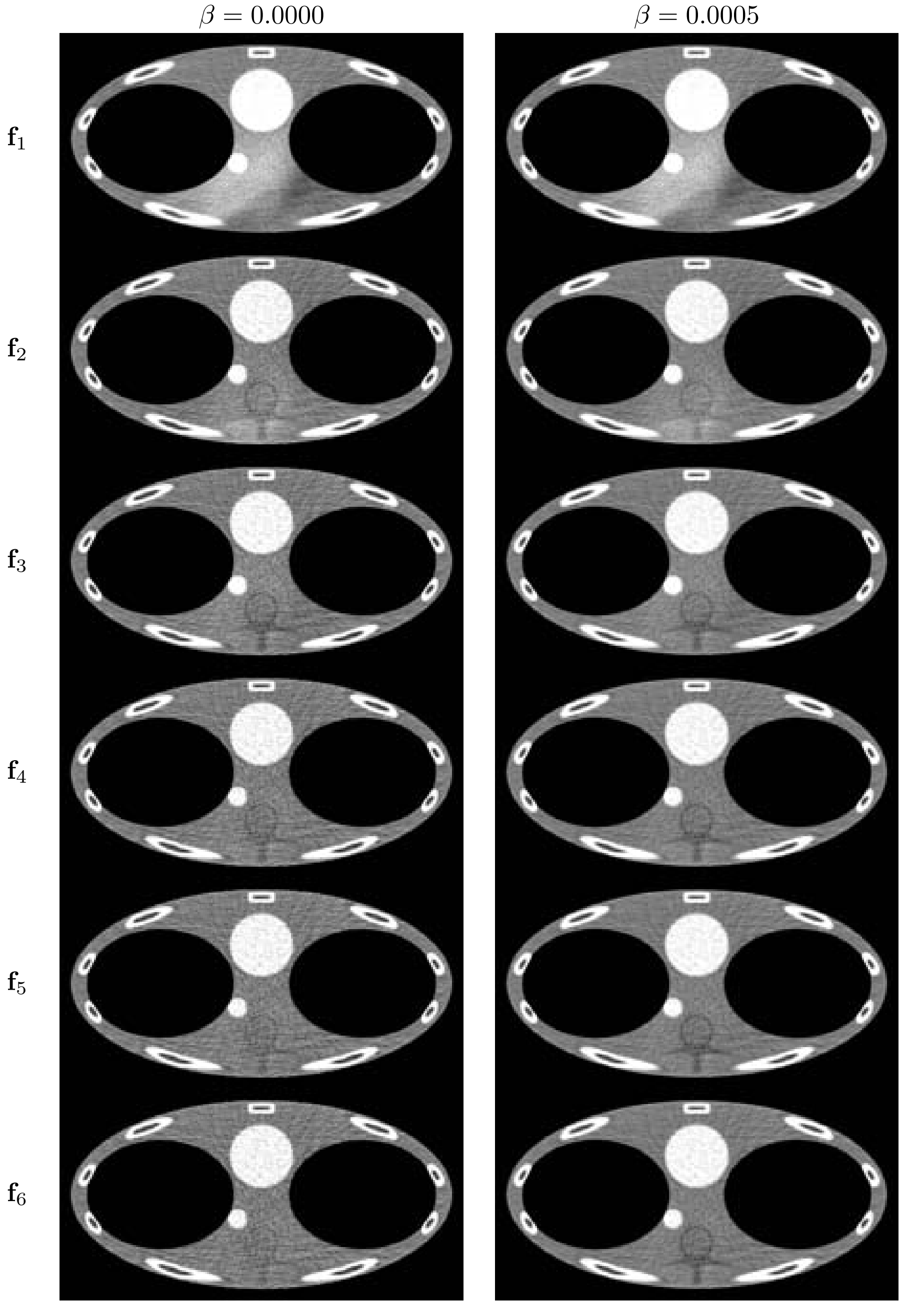

Figure 5.3: Axial slices first six results of IWFBP reconstructions with and without regularization. Enlarged images of the area around the spine can be found in Figure 5.4. Grey scale window: ±50 HU.

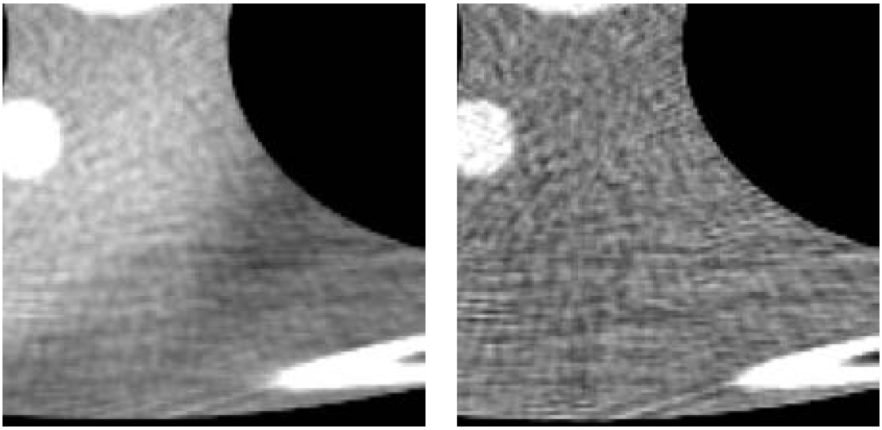

(a) WFBP reconstruction (b) IWFBP, $\mathbf{f}_6$, $\beta = 0.0000$

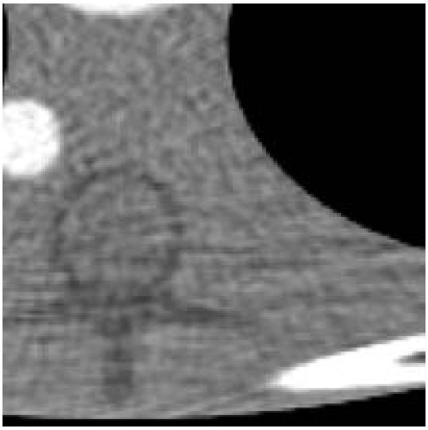

(c) IWFBP, $\mathbf{f}_6$, $\beta = 0.0005$

Figure 5.4: Axial slices of the first six results of IWFBP reconstructions with and without regularization. The dark vertebra like structure is an overshoot from a real vertebra located very close to this slide. This overshoot is apparently stronger for $\beta = 0.0000$ than for $\beta = 0.0005$. However, looking at Figure 5.15 we see that the maximum amplitude of the overshoots is actually higher for $\beta = 0.0000$. Grey scale window: ±50 HU.

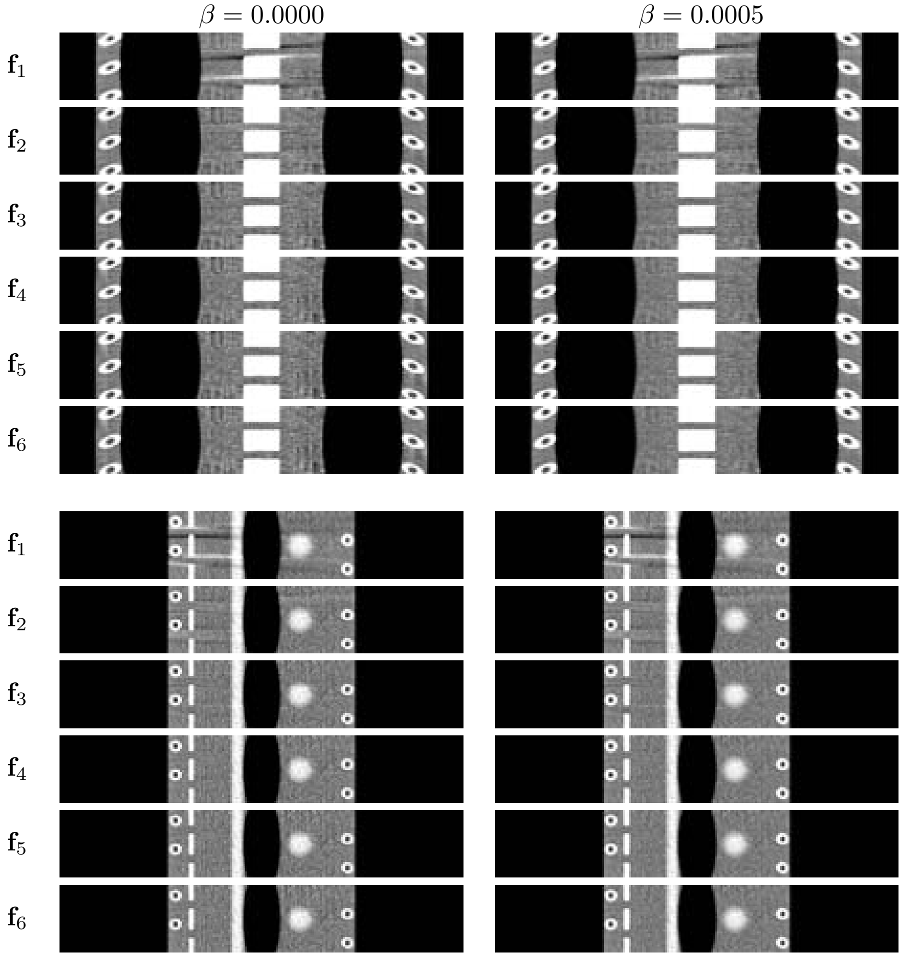

Figure 5.5: Coronal and saggital slices of the first six results of IWFBP reconstructions with and without regularization. Grey scale window: ±50 HU.

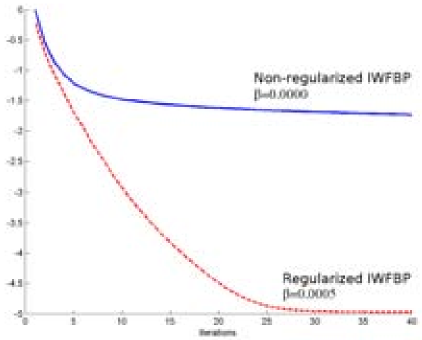

Figure 5.6: The sequence $\log_{10}(\|\mathbf{f}_{k+1} - \mathbf{f}_k\|/C)$ used for measuring convergence. The value of C was chosen so that the largest value of the sequence became zero.

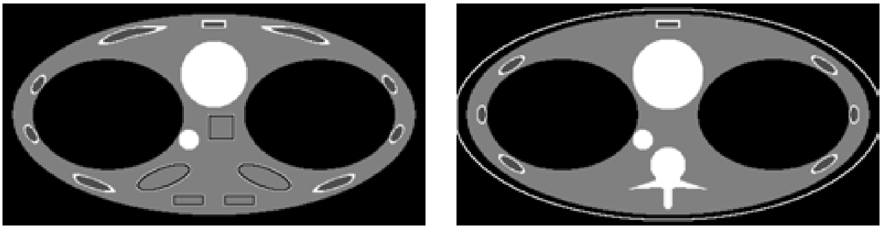

(a) Cone artifact area. $z = 12$mm (b) Whole image area. $z = 0$mm

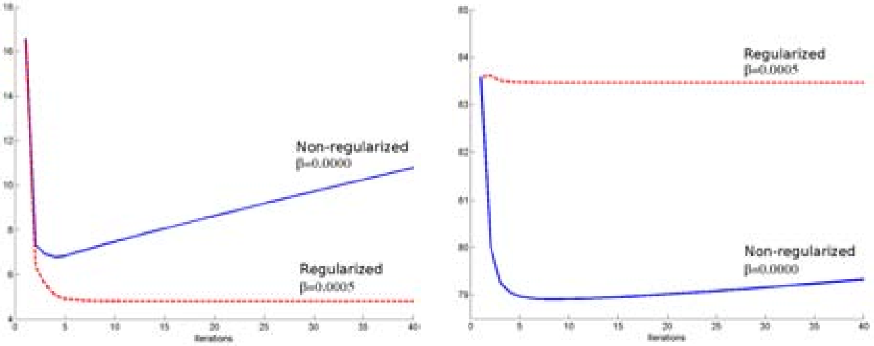

(c) RMSE - cone artifact area (d) RMSE - whole image

Figure 5.7: Root mean squared errors (RMSEs) as a function of the number of iterations. These measures have been calculated over the two different sets shown in (a) and (b).

whole image. Here the RMSE mainly represents differences near edges. This is realized by observing that the overall RMSE values in Figure 5.7d are approximately ten times larger than the values of the cone mask RMSE in Figure 5.7c taken over areas without sharp edges. Here, the non-regularized IWFBP improves the RMSE during the first five iterations, while the RMSE for the regularized IWFBP remains at a constant level, close to that of the WFBP. One similarity between Figure 5.7c and 5.7d is that in both cases, the non-regularized IWFBP keep changing, while the regularized version converges to a practically constant result after a few iterations.

Since the patient usually is longer than the length of the examined area, there are locations that can not be correctly reconstructed. It is not trivial to see how this will affect the results in the iterative loop. Luckily, it was shown by Magnusson *et al.* [48] that if the reconstruction and projection is performed on a voxel grid that fully covers the path of all rays involved, the result will improve rather than degrade near the border of the region of interest(ROI). The result from [48] is fully verified in Figure 5.8.

5.3 Spatial resolution and noise

As showed in the previous section, the frequency characteristics of the IWFBP after a few iterations are different from those of the WFBP. This means not only that the spatial resolution changes during iteration, but also the noise properties. Two parameters that affect the frequency characteristics are the value of the regularization parameter β and the resolution of the image matrix, characterized by the sampling distances Δ_x and Δ_z. In this section, experiments are presented with β ranging from 0 to 0.0007 and image matrix configurations as shown in Table 5.1. The size of the image matrix follows suite with the sampling distance since we are using a phantom of the same size.

Figure 5.10 and 5.11 show axial and coronal slices of the results obtained with non-regularized ($\beta = 0$) IWFBP for the three different configurations listed in Table 5.1. The noise levels, calculated as in Section 4.2 are equal to 6.37 HU for $\mathcal{C}_1$, 6.34 HU for $\mathcal{C}_2$ and 5.78 HU for $\mathcal{C}_3$. Measurements of SSPs show that the amplitude of the overshoots observed for the $\mathcal{C}_1$ resolution are reduced to less than half of its original value when increasing the resolution to the $\mathcal{C}_3$-configuration. The overshoots are caused by the inability of a basis function, or rather a set of weighted basis functions to compose an edge represented by input data. Only if the edge is bandlimited, and the spacing and frequency characteristics of the

Table 5.1: Image matrix and sampling distances.

Conf.	Image matrix	Sampling distances
$\mathcal{C}_1$	$N_x = N_y = 257, Nz = 129$	$\Delta_x = \Delta_y = 1.95\text{mm}, \Delta_z = 1.50\text{mm}$
$\mathcal{C}_2$	$N_x = N_y = 385, Nz = 193$	$\Delta_x = \Delta_y = 1.30\text{mm}, \Delta_z = 1.00\text{mm}$
$\mathcal{C}_3$	$N_x = N_y = 513, Nz = 257$	$\Delta_x = \Delta_y \approx 0.98\text{mm}, \Delta_z = 0.75\text{mm}$

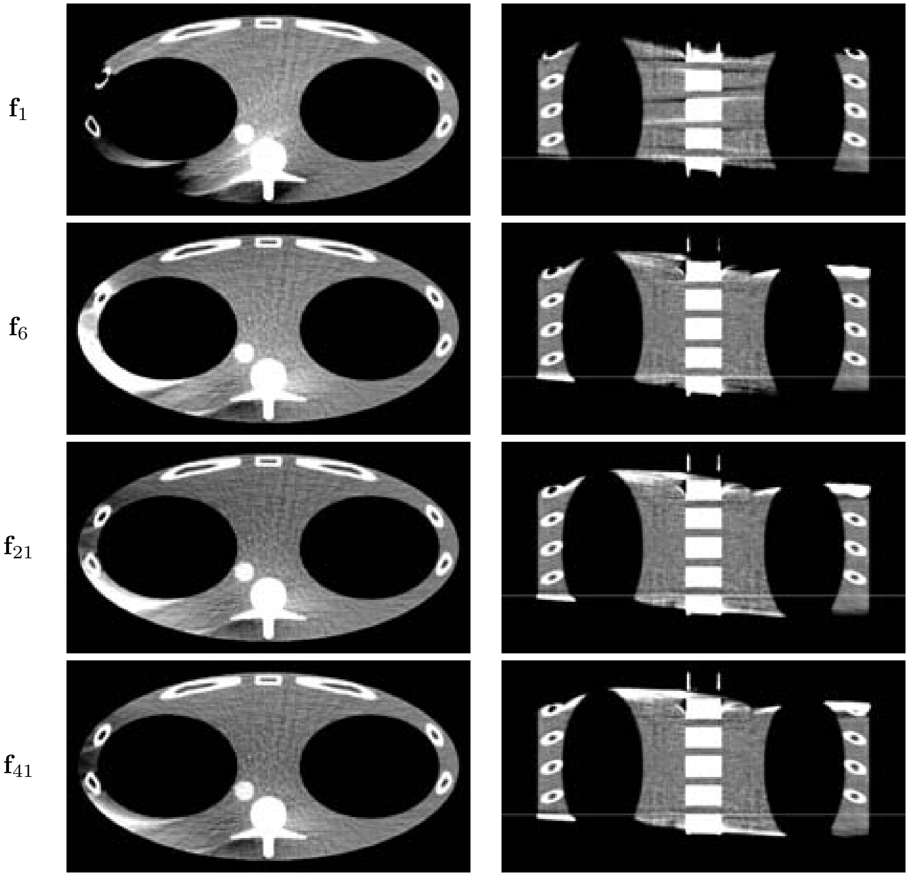

Figure 5.8: Axial and coronal slices of the regularized IWFBP results showing a slice that can barely be reconstructed with the available data. No propagation of truncation artifacts in the z-direction even after 41 iterations. The lines in the coronal slices show the location of corresponding axial slices. Grey scale window: ±50 HU.

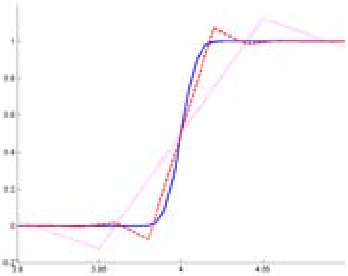

Figure 5.9: Illustration of least square fitting to a *bandlimited* edge with two linear interpolation basis functions with different widths. The solid line show the bandlimited input data and the dashed and dotted lines show the least square fits. Clearly, a better fit with lower overshoots is obtained for the set with small basis function width and spacing. Note that this is true only for bandlimited input data. For an ideal edge, the overshoots would be of same amplitude independent of width and spacing.

basis function set match the highest non-zero frequency component of the input data, a result without overshoots can be obtained (see Figure 5.9 for an one-dimensional example). Since this set in the $\mathcal{C}_1$ configuration contain less high-frequency components than the basis function set in the $\mathcal{C}_3$ configuration, the overshoots are less pronounced for the $\mathcal{C}_3$ configuration.

Even when reconstructing to a relatively high resolution such as the $\mathcal{C}_3$-configuration from Table 5.1, the overshoot amplitudes are significant. In the z-direction, the maximum amplitude is 5% of the edge amplitude. The amplitude of the noise is also markedly higher: 5.78 HU compared to 3.50 HU for the WFBP reconstruction. By changing the value of β, it is possible to alter the frequency characteristics of the final result. Figure 5.12 and 5.13 show axial and coronal slices from results with β ranging from zero to 0.007. As β is increased, both the amplitudes of the overshoots and the noise are reduced. The σ_e and σ_n values for different values of β are given in Table 5.2. From this table, an IWFBP reconstruction with $\beta = 0.0005$ comes closest to the original WFBP reconstruction in terms of noise and overall RMSE.

Comparing noise levels for different reconstruction methods only makes sense if the spatial resolution properties simultaneously are taken into account. Therefore, modulation transfer functions (MTFs) and slice sensitivity profiles (SSPs) have been calculated for different values of β and for the direct WFBP reconstruction.

The MTFs are shown in Figure 5.14. Compared to the WFBP, clearly $\beta = 0.0000$ and $\beta = 0.0003$ results in higher spatial resolution in the xy-plane, while $\beta = 0.0007$ results in a slightly lower resolution. For $\beta = 0.0005$, the MTF of IWFBP after 6 iterations is approximately equal to the MTF of WFBP.

Figure 5.15 show SSPs for different values of β. Examining the full widths at half maximum (FWHM), the IWFBP with $\beta = 0.0007$ comes closest to the WFBP method. However, in terms of low overshoots in the z-direction, none of

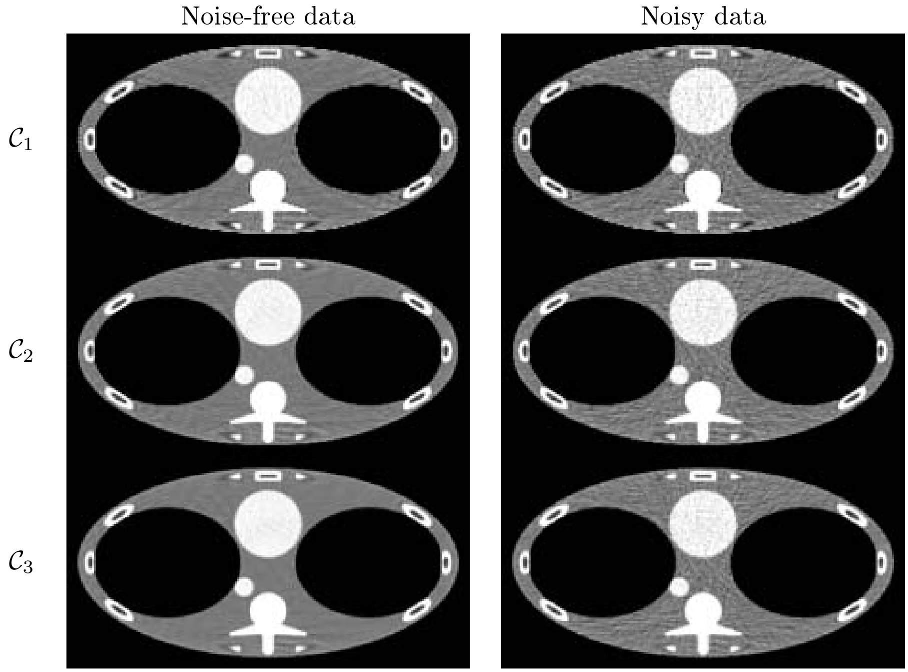

Figure 5.10: Axial slices of non-regularized ($\beta = 0$) IWFBP $\mathbf{f}_6$ reconstructions with different resolutions of the image matrix (see Table 5.1 for a specification). Grey scale window: ±50 HU.

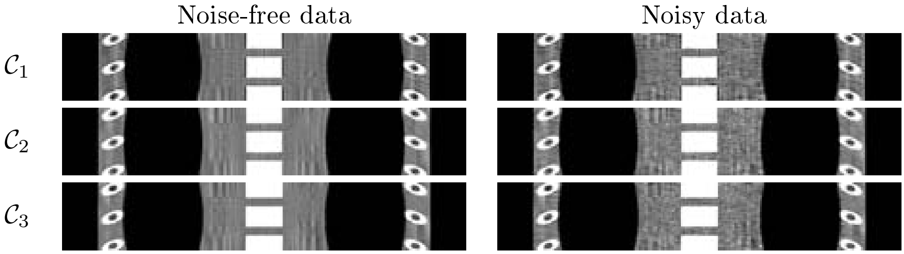

Figure 5.11: Coronal slices of non-regularized ($\beta = 0$) IWFBP $\mathbf{f}_6$ reconstructions with different resolutions of the image matrix (see Table 5.1 for a specification). Grey scale window: ±50 HU.

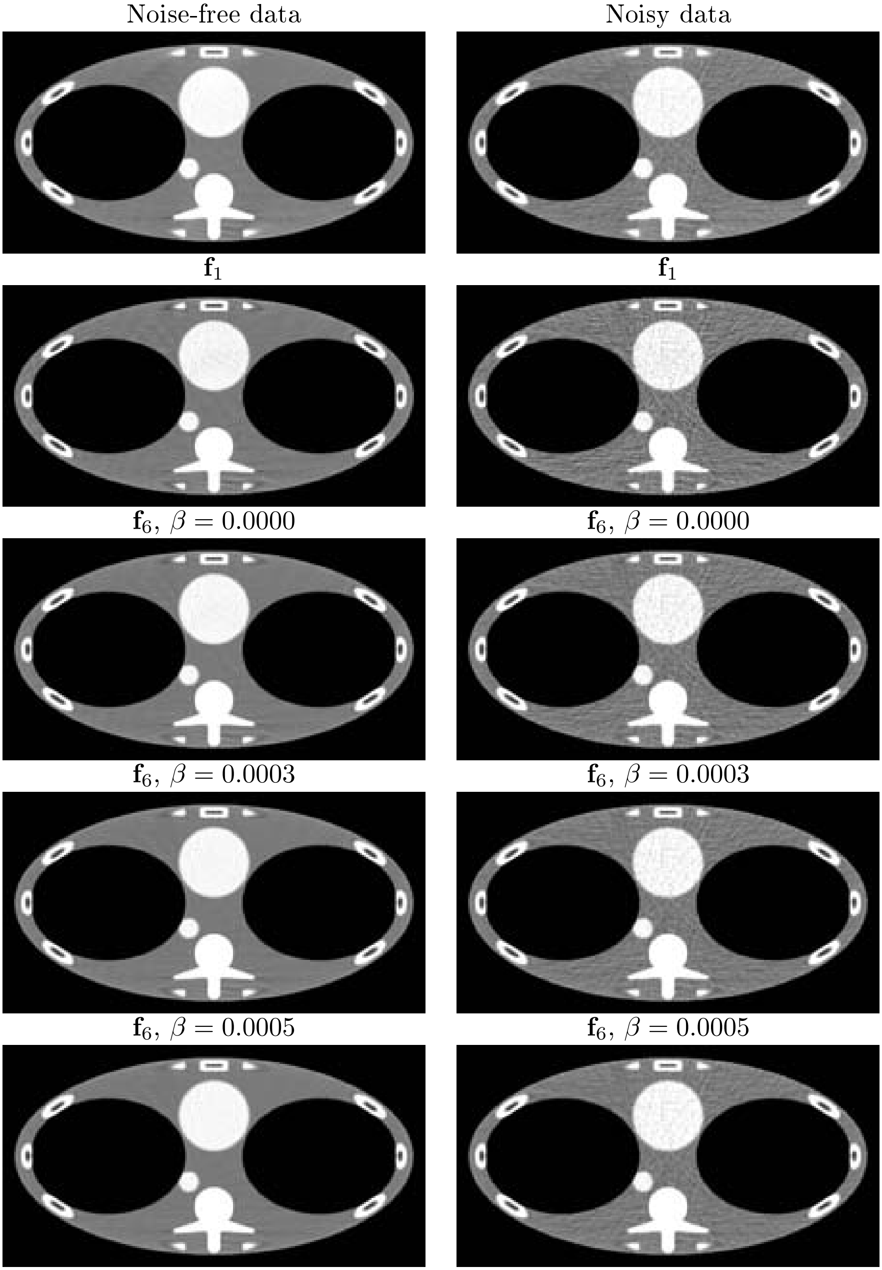

$\mathbf{f}_1$ $\mathbf{f}_1$

$\mathbf{f}_6$, $\beta = 0.0000$ $\mathbf{f}_6$, $\beta = 0.0000$

$\mathbf{f}_6$, $\beta = 0.0003$ $\mathbf{f}_6$, $\beta = 0.0003$

$\mathbf{f}_6$, $\beta = 0.0005$ $\mathbf{f}_6$, $\beta = 0.0005$

$\mathbf{f}_6$, $\beta = 0.0007$ $\mathbf{f}_6$, $\beta = 0.0007$

Figure 5.12: Axial slices of IWFBP reconstructions with different values of the regularization parameter β. Grey scale window: ±50 HU. See also table 5.2.

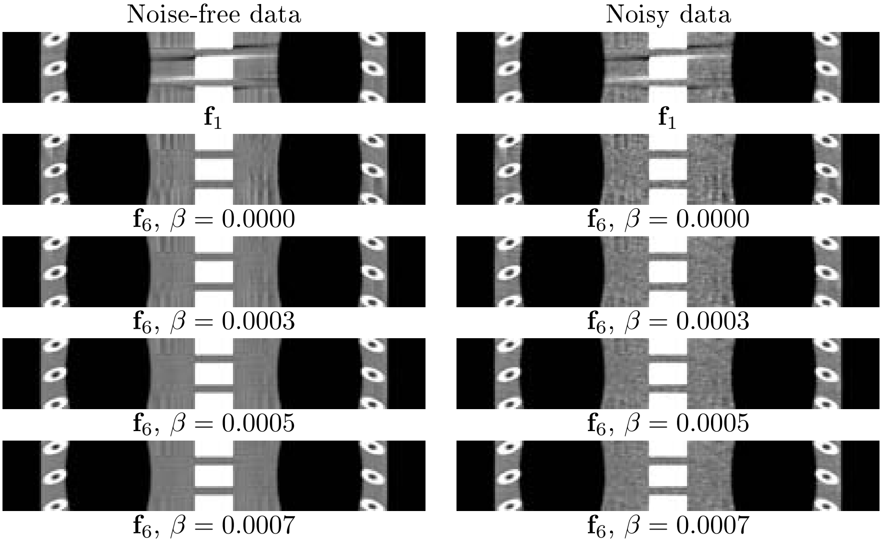

Figure 5.13: Coronal slices of IWFBP reconstructions with different values of the regularization parameter β. Grey scale window is ±50 HU. See also table 5.2.

Table 5.2: σ_e and σ_n values after five iterations for different values of β. The sampling distances are $\Delta_x = \Delta_y = 0.98$mm and $\Delta_z = 0.75$mm. Images shown in Figure 5.12 and 5.13.

β	σ_e (HU) cone artifact areas	σ_e (HU) whole image	σ_n (HU)
WFBP	16.21	83.54	3.50
0.0000	4.00	78.80	5.78
0.0003	3.41	81.57	4.43
0.0005	3.27	83.41	3.79
0.0007	3.21	85.24	3.28

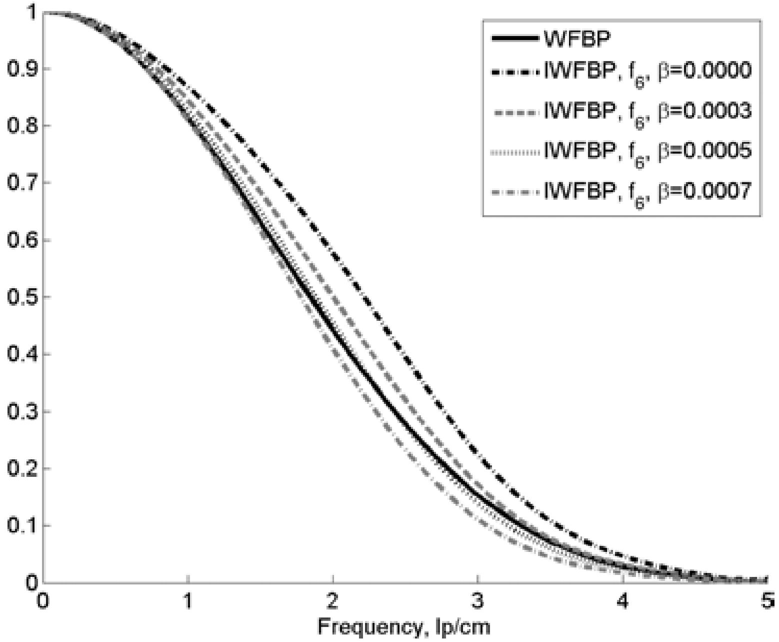

Figure 5.14: Modulation transfer functions (MTFs) measured for WFBP and IWFBP with $\beta = 0.0000, 0.0003, 0.0005$ and 0.0007.

the IWFBP reconstructions match the original WFBP reconstruction very well. For $\beta = 0.0005$, which resulted in an MTF similar to the WFBP MTF, the SSP FWHM of the IWFBP is slightly smaller than that of the WFBP method. On the other hand, overshoots appear in the IWFBP results but not in the WFBP results. In Table 5.2, we see that the noise properties for WFBP and IWFBP with $\beta = 0.0005$ are quite similar.

In Table 5.3, the values of the figures of merit Q_1 and Q_2 introduced in Section 4.2 are shown. For $\beta = 0.0005$, we see that the Q_1 and Q_2 values for WFBP are slightly higher than for the IWFBP.

It does not seem reasonable to use Q_1 or Q_2 to compare methods at different spatial resolutions, since these figures of merit clearly vary with the value of β. Even simple low-pass filtering of the result from non-regularized IWFBP with a Gaussian with $\sigma = 1.40\Delta_{xyz}$ yields an improvement of Q_1 from 0.83 to 1.33.

5.4 Low contrast images

For statistical reconstruction using the Siddon projection operator [68], Zbijewski and Beekman [84] showed that image quality is improved by reconstructing to higher sampling density. This was partially verified in the last section, where it was observed that edge overshoots and noise became more pronounced if the resolution was too low. On the other hand, the grey scale window was too large

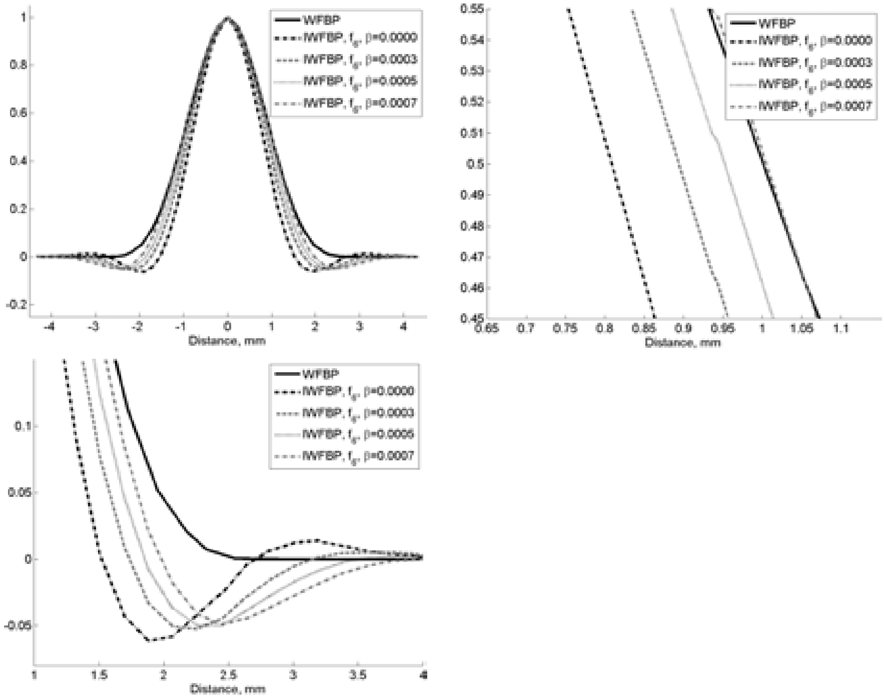

Figure 5.15: Slice sensitivity profiles (SSPs) measured for WFBP and IWFBP with $\beta = 0.0000, 0.0003, 0.0005$ and 0.0007.

Table 5.3: $Q_1 = c/(\sigma^2 \rho_{10\%}^{-3} SD)$, $Q_2 = c/(\sigma^2 \rho_M^{-3} SD)$ and the entities used for caluculating these figures of merit for different values of β. The dose is excluded, since it is kept constant.

β	σ_n (HU)	$\rho_{10\%}$ (cm^{-1})	$\rho_{50\%}$ (cm^{-1})	S (mm)	Q_1	Q_2
WFBP	3.50	3.30	1.84	2.01	1.47	0.69
0.0000	5.78	3.55	2.22	1.62	0.83	0.44
0.0003	4.43	3.35	2.00	1.79	1.07	0.55
0.0005	3.79	3.21	1.88	1.90	1.21	0.60
0.0007	3.28	3.06	1.78	2.01	1.32	0.65
0.0009	2.87	2.91	1.69	2.12	1.41	0.70

to detect artifacts that could disturb the detection of low contrast objects.

In this section, the low-contrast phantom from Section 4.2 has been two-dimensionally reconstructed to different resolutions with the WFBP and IWFBP algorithms. As shown at the end of Section 2.1, backprojection can be seen as a procedure which samples a continuous function. In fact, this is the point where the sampling density of the image matrix comes into play. Hence, the artifact level of the WFBP method at constant regions does not depend on this sampling density. For IWFBP, this is not true. Suppose that an area in an image, for instance due to an insufficient sampling density (illustrated for the one-dimensional case in Figure 5.9), cannot be properly reconstructed by an iterative method. Then the error in this area will introduce errors in all projection data to which this area contributes. When these data are subtracted from input data and backprojected, since the basis function is unable to represent the correct result in the area of interest, erroneous "corrections" will be made outside the area of interest along every ray that travels through this area. Therefore, errors caused by an insufficient sampling density will be less local than in the one-dimensional case illustrated in Figure 5.9.

Figure 5.16 shows one WFBP reconstruction and three IWFBP reconstructions to image matrices with dimensions $N_x = N_y = 385,\ 513,\ 1025$ respectively. At the lower resolutions, errors caused by imperfect image representation clearly propagates into the interior of the water cylinder and disturbs the detection of the smallest low contrast objects. If the dimension of the image matrix is increased to 1025×1025, even for the small gray scale window ±5HU, artifacts are practically invisible.

5.5 Rebinning inside versus outside the iterative loop

In all experiments presented so far, rebinning to a semi-parallel geometry has been performed before entering the iterative loop. This makes implementation of the projection operator slightly simpler and enable us to use ordered subsets together with IWFBP (see Chapter 6). However, low-pass filtering as well as artifacts caused by the rebinning process will appear also in the final result $\mathbf{f}_\infty$. Also, accurate modeling of focus, detector elements, and gantry rotation in the projection operator $\mathbf{P}$ is more difficult. Therefore, in spite of the increased complexity, it is tempting to place the rebinning operation inside the iterative loop and replace the semi-parallel projection operator $\mathbf{P}$ with an operator $\mathbf{P}_{\text{cone}}$ generating true cone beam projections.

Figure 5.17a and 5.17b show images reconstructed with IWFBP. The image in Figure 5.17a was reconstructed with the rebinning process placed outside the iterative loop as in previous experiments and in Figure 5.17b, the rebinning was placed inside the iterative loop. Visual inspection reveals a clear difference in edge response between the two methods. This difference is even more obvious when studying the values of the images along a centered horizontal line as in Figure 5.17c and 5.17d. The amplitude of the overshoot near the edge of the water cylinder is around 8 times higher when the rebinning is placed inside the iterative

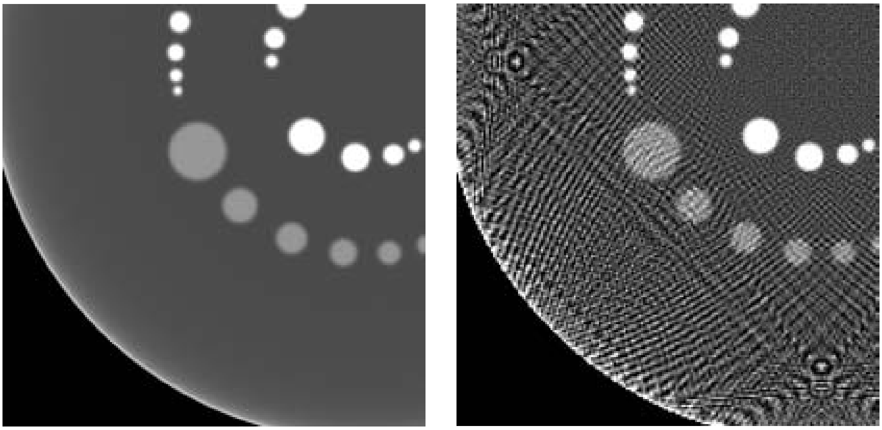

(a) WFBP reconstruction

(b) IWFBP, $\mathbf{f}_6$, $N_x = N_y = 385$

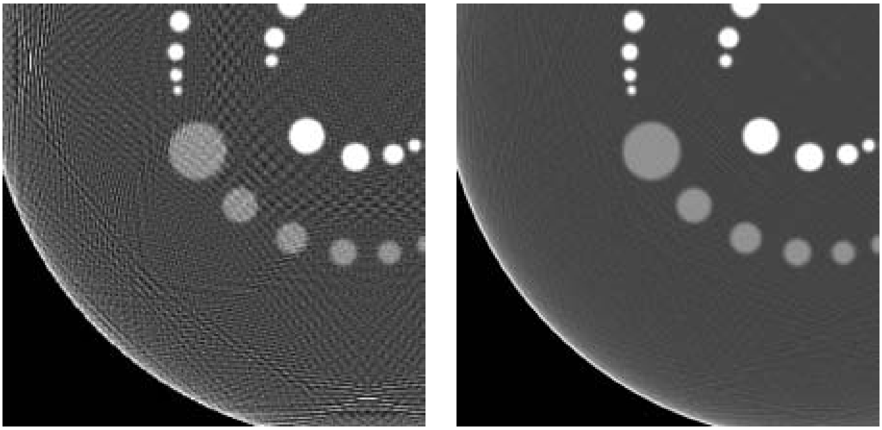

(c) IWFBP, $\mathbf{f}_6$, $N_x = N_y = 513$

(d) IWFBP, $\mathbf{f}_6$, $N_x = N_y = 1025$

Figure 5.16: Noise-free WFBP and IWFBP reconstructions of the low contrast phantom. The resolution in (b) corresponds to configuration $\mathcal{C}_2$ and (c) corresponds to $\mathcal{C}_3$ earlier in this section. Grey scale window ±5 HU.

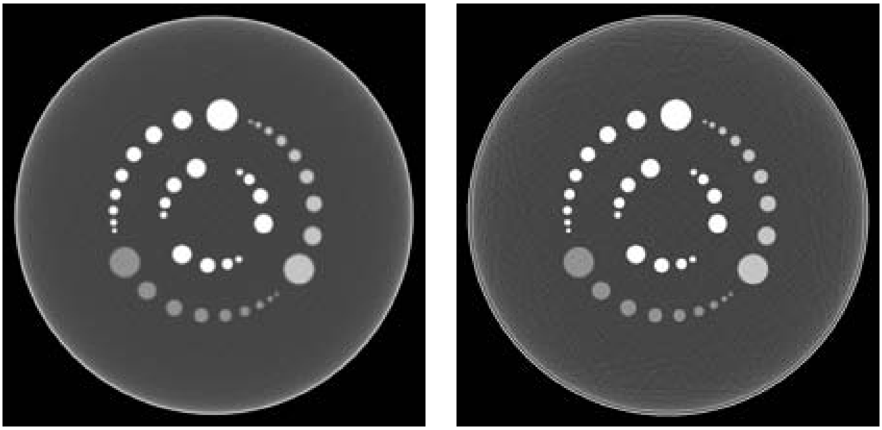

(a) Rebinning outside loop

(b) Rebinning inside loop

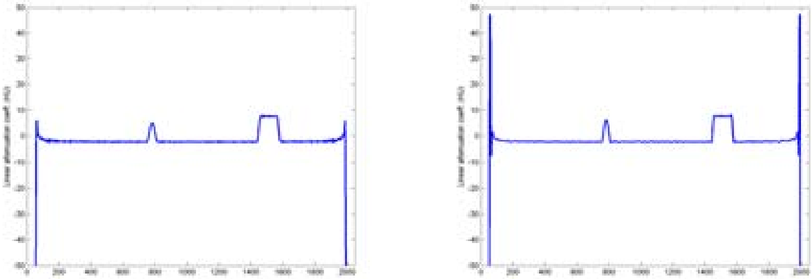

(c) Profile, reb. outside loop

(d) Profile, reb. inside loop

Figure 5.17: Results from IWFBP reconstruction with the rebinning operation located outside and inside the iterative loop respectively. (c) and (d) show the reconstructed linear attenuation coefficients along a horizontal line cutting through the center of the cylinder. Greyscale window ±5 HU.

loop.

It is difficult to draw any strong conclusions regarding the cause of this effect from this experiment. One likely explanation could be that the rebinning operation acts as a low-pass filter, setting a certain high frequency to zero before backprojection. This would cause the MTF of the IWFBP to drop with a steep gradient close to this frequency. Other explanations could be that this effect is caused by the changed geometry of the projection operator $\mathbf{P}$, or the fact that the difference between the adjoint operator $\mathbf{P}^T$ and rebinning followed by backprojection is larger when the rebinning is located inside the iterative loop. In order to further investigate this, a comparison could be made with methods that do not include a rebinning step, for instance SIRT.

5.6 Conclusions

In this chapter we have seen how the IWFBP can be used for suppressing cone-artifacts caused by WFBP at a cone angle of $\pm 4.8^\circ$ in less than five iterations. The question regarding final convergence of the non-regularized IWFBP remains, but it has been shown that the behavior can be stabilized by introducing the regularization matrix $\mathbf{R}$ handled in Section 3.5.

The frequency and noise characteristics of IWFBP obviously changes as a function of the number of iterations. However, by choosing an appropriate value of the regularization parameter β, the characteristics become very similar to those of the WFBP reconstruction. With regularization, the IWFBP reaches the final solution faster than without. It is therefore easier to determine when to terminate the iterative loop.

The experiments on different resolutions show that for the current scanner setup using a detector system with 336 channels with quarter offset, the resolution of the image matrix should be at least 512×512 in order to avoid edge and aliasing artifacts. More improvement can be achieved by an even larger image matrix.

Placing the rebinning operation inside the loop results in strong overshoots. Further investigations must be done in order to find how these results relate to iterative methods where no rebinning operation is present.

One topic that remains to be investigated is whether the weights d_{ij} in the regularization can be changed with respect to the ratio Δ_x/Δ_z in order to gain better control over the spatial resolution in the xy-plane as well as in the z-direction. Another topic is to find out how different choices of Q-weightings in the WFBP reconstruction (not to be confused with the figures of merit Q_1 and Q_2) affect the required number of iterations and noise levels. High Q-values imply low noise, but in ordinary non-iterative WFBP high Q-values are prohibited since they introduce severe artifacts. Possibly, this could be tolerated if the artifacts can be suppressed by the IWFBP scheme.

Chapter 6

Ordered subsets IWFBP (OS-IWFBP)

6.1 Introduction

The IWFBP method described in the last chapter is simultaneous in the sense that all projection data are used in each iteration. In Section 3.4, it was shown how a simultaneous diagonally weighted least squares method can be turned into an ordered subsets method, *i.e.* a method where only a subset of the projection data are employed in each update. For a low number of subsets, the conclusion in several papers ([29, 36, 19] among others) is that by using the ordered subsets technique, an acceleration factor approximately equal to the number of subsets is possible to achieve for statistical reconstruction methods.

In this chapter, experiments on using this technique on the IWFBP method are presented. The basic idea is to divide the projection data $\mathbf{p}_{\text{in}}$ into L equidistantly sampled subsets $\mathbf{p}_{\text{in},1}, ..., \mathbf{p}_{\text{in},L}$ with respect to the rotation angle θ so that two subsets only differ by an offset (see Figure 6.1). For each subset $\mathbf{p}_{\text{in},l}$, new matrices $\mathbf{P}_l$ and $\mathbf{Q}_{\text{WFBP},l}$ are defined. These matrices produce and reconstruct from projection data corresponding to $\mathbf{p}_{\text{in},l}$. After one initial full reconstruction, the update step of the ordered subsets IWFBP (OS-IWFBP) method is given by

$$\mathbf{f}_{k+1} = \mathbf{f}_k + \alpha_k \mathbf{Q}_{\text{WFBP},i_k}(\mathbf{P}_{i_k}\mathbf{f}_k - \mathbf{p}_{\text{in},i_k}) \tag{6.1}$$

where the sequence $\{i_k\}_{k=1}^{\infty}$ defines the ordering of the subsets. We will restrict the discussion to periodic ordering schemes, *i.e.* schemes that satisfy $i_k = i_{k+nL}, n \in \mathbb{N}$. In the case of periodic ordering, assuming that all subsets are used, a *full iteration* is defined as L consecutive sub-updates.

The motivation behind using the ordered subsets technique together with the IWFBP method is that for reconstructing low frequencies, only a small set of projection angles are needed. Since cone artifacts produced by the WFBP method mostly consist of low frequencies, almost the same reduction could be obtained with a partial update employing only a subset of projection angles, as with a full

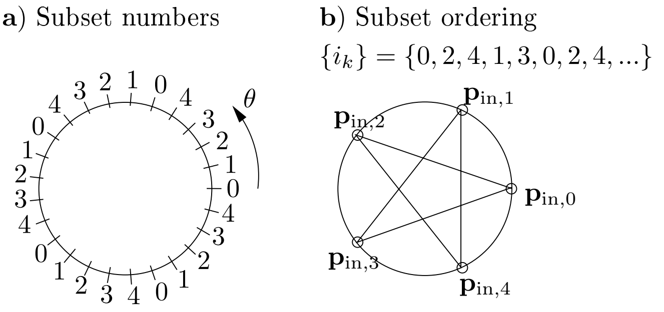

Figure 6.1: **a**) Simple example of how projection data with respect to the rotation angle θ are divided into equidistantly sampled subsets that only differ by an offset. There are 25 projection angles and the number of subsets is 5. **b**) Example of an ordering scheme.

simultaneous update. Thus, suppression of cone artifacts could in best case be accelerated with a factor equal to the number of subsets.

Several new free parameters are introduced when OS is combined with the IWFBP. The most important parameters are

- The number of subsets L.
- The sequence $\{i_k\}$, defining the order in which the subsets are to be applied.
- The step lengths α_k. These are free parameters also for the original IWFBP, but the choice is more important when ordered subsets are used.
- The degree of low-pass filtering of updates. See below and Section 6.3 for details.

In the next section, two different ordering schemes are presented. Two-dimensional experiments are performed to determine reasonable α values for different number of subsets and whether the ordering schemes lead to significantly different results.

It turns out that high-frequent artifacts are introduced when the ordered subsets technique is added to the IWFBP method. This is not surprising since each update uses too few projection angles in relation to the radial resolution of the projection data. In Section 6.3, we investigate the possibility to reduce these artifacts by low-pass filtering the updates either in reconstruction space or in the radial direction of the projection data.

Having determined reasonable values on the step-lengths and low-pass filters, it is time to investigate how well the reduction of cone artifacts work for OS-IWFBP in comparison to ordinary IWFBP. This is done in Section 6.4.

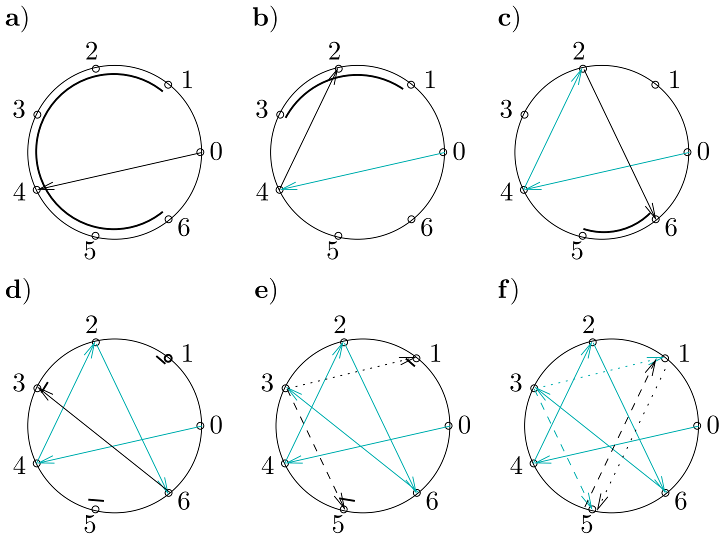

a) $i_0 = 0 \Rightarrow$ largest gap $= \{1...6\} \Rightarrow i_1 = 4$
b) $i_1 = 4 \Rightarrow$ largest gap $= \{1...3\} \Rightarrow i_2 = 2$
c) $i_2 = 2 \Rightarrow$ largest gap $= \{5...6\} \Rightarrow i_3 = 6$
d) $i_3 = 6 \Rightarrow$ equally sized gaps $= \{1\}, \{3\}, \{5\} \Rightarrow i_4 = 3$
e) $i_4 = 3 \Rightarrow$ equally sized gaps $= \{1\}, \{5\} \Rightarrow i_5 = ?$

Figure 6.2: Illustration of the HLBK ordering scheme. Given a number of subset indices $i_1, i_2, ..., i_n$, the largest gaps of unused subsets are identified. The new index i_{n+1} is chosen as close as possible to the gap center located as far away from the subset i_n as possible.

6.2 Number of subsets and ordering schemes. 2D experiments.

The quality of reconstruction results produced with OS-IWFBP depends on the order in which the different subsets are applied. Here, we first present and examine the scheme presented by Beekman and Kamphuis [2] (which is similar to the scheme by Hudson and Larkin [29]) followed by another scheme based on the Golden ratio and originally developed for SART by Köhler [39].

The *Hudson-Larkin-Beekman-Kamphuis (HLBK)* scheme works as illustrated with an example in Figure 6.2. Given a number of subset indices $i_1, i_2, ..., i_n$, next index i_{n+1} is chosen as close as possible to the center of the largest gap of unused subsets. If several gaps of the same size exist, the center set located as far away as possible, *i.e.* as close to $L\Delta_\theta/2$ as possible, is chosen. Sometimes several subsets satisfy the last condition (see for instance Figure 6.2). Then the choice between the remaining centrally located subsets is random.

The greediness of the HLBK ordering scheme sometimes lead to the unfortunate situation illustrated in the Figure 6.2f. Since no subset other than the closest neighbor of the first subset is available, the first subset will consequently be employed directly after its closest neighbor. This can result in image artifacts. A class of ordering schemes not suffering from this drawback can be created by observing that one can visit all available subsets in L steps by choosing subsets according to

$$i_{n+1} = (i_n + m) \mod L \tag{6.2}$$

for any $m \in \mathbb{Z}^+$ such that $\gcd(L, m) = 1$. This is trivial for $m = 1$ and a general proof is found in [23]. When the number of subsets is prime, this means that any increase by m modulo L will create a periodic ordering scheme that employs all subsets.

The *Golden ratio ordering scheme* by Köhler [39] was shown to deliver good results for SART using an angular increment as close as possible to the golden ratio times 2π, *i.e.*

$$2\pi\frac{\sqrt{5}-1}{2}. \tag{6.3}$$

This can be adapted to the ordered subsets technique by choosing the order of subsets so that the angular increment comes as close as possible to

$$L\Delta_\theta\frac{\sqrt{5}-1}{2} \tag{6.4}$$

and satisfies $\text{gcf}(L, m) = 1$. Again, when L is prime, $\text{gcf}(L, m) = 1$ is satisfied for all $m \in \mathbb{Z}^+$ that is not equal to L. We will refer to this scheme as the golden ratio (GR) ordering scheme. In the case of five and seven subsets, the golden ratio scheme becomes as shown in Figure 6.1 and 6.3 respectively.

Experimental investigation of both these methods has been performed for the two-dimensional version of the geometry specified in Section 4.1. The underlying assumption is that unwanted artifacts generated by the OS technique will prevail in the same way in the 3D-case. The space of free parameters was restricted by only considering α_k constant with respect to k, *i.e.* $\alpha_k = \alpha$. In Table 6.1 the different parameters for these experiments are shown. The leftmost and largest α value in each row resulted in a divergent sequence, while the rightmost and lowest lowest resulted in a slow rate of convergence.

Ten iterations per configuration were performed. Visual inspection reveals that for high values of α, certain noise-like artifacts appear in the OS-IWFBP results. As a numerical measure of these artifacts, the error (repetition of equation (4.5))

$$\sigma_e = \sqrt{\frac{1}{|\Omega|}\sum_{i\in\Omega}((\mathbf{f}_{\text{rec}})_i - (\mathbf{f}_{\text{phan}})_i)^2} \tag{6.5}$$

has been calculated over the constant regions shown in Figure 4.6c. These error measurements are presented in Figure 6.4. For comparison, the solid line without any markers in these figures show the corresponding error for ordinary IWFBP.

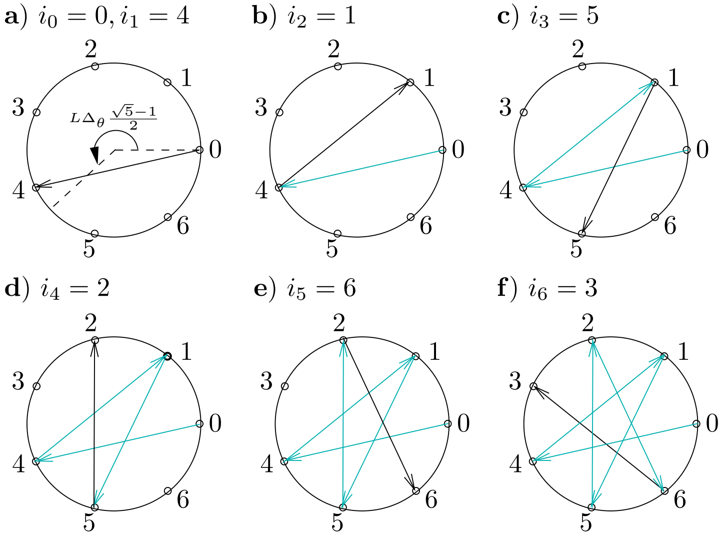

a) $i_0 = 0, i_1 = 4$ **b)** $i_2 = 1$ **c)** $i_3 = 5$

d) $i_4 = 2$ **e)** $i_5 = 6$ **f)** $i_6 = 3$

Figure 6.3: Illustration of the golden ratio ordering scheme when the number of subsets is seven.

Table 6.1: Parameters for two-dimensional experiments with different numbers of subsets, α values, and ordering schemes. The acronyms GR and HLBK refers to the golden ratio and Hudson-Larkin-Beekman-Kamphuis ordering schemes respectively. For two and five subsets, the GR and HLBK schemes are equivalent.

Number of subsets	α values	Ordering schemes
2	1.00,0.70,0.50,0.20	GR
5	0.50,0.35,0.20,0.10	GR
10	0.25,0.15,0.10,0.05	GR,HLBK
29	0.10,0.07,0.05,0.02	GR,HLBK

Obviously, a low α value can be used to avoid introduction of artifacts in constant regions. However, this implies a slow rate of cone artifact reduction. Therefore, it is interesting to see how high α can be chosen without resulting in unacceptable artifacts. These results will be used in Section 6.4 for determining which values of α to use for three-dimensional cone-artifact reduction experiments.

Clearly, the highest allowable α varies strongly with the number of subsets. For the different subset configurations included in this experiment, $\alpha = 1/N_{\text{sets}}$ seem to result in approximately the same error curve as the ordinary IWFBP method. However, higher initial error increase than the one produced by IWFBP may be allowed if the cone artifact reduction is such that the method can be terminated already after a few iterations.

Square norms like σ_e give no information about the structure of the errors. Therefore, to see what the numbers presented in Figure 6.4 mean in terms of "real" image quality, reconstruction results after one and two full iterations with five subsets are presented in Figure 6.5. These images reveal that after one full iteration, circular artifacts emanating from the vertebra are more pronounced for ordered subsets with $\alpha = 0.35$ and $\alpha = 0.5$ than for ordinary IWFBP. After two full iterations, the difference between ordinary IWFBP and OS-IWFBP is diminished for $\alpha = 0.35$, but enhanced for $\alpha = 0.5$.

Regarding the ordering of subsets, we have already concluded that the GR and HLBK ordering schemes are equivalent for two and five subsets respectively. For higher numbers, the differences may be larger. However, with respect to the measures presented in Figure 6.4, the differences between these two schemes seem to be neglectable. In Figure 6.6, results after one full iteration using 10 and 29 subsets with both ordering schemes are shown. The images produced by the two ordering schemes differ slightly. The ringing artifacts are more pronounced for the GR scheme but at least in the case of 29 subsets, the noise-like artifacts are more pronounced for the HLBK scheme.

6.3 Low-pass filtering of updates

High values of α (close to 1) imply efficient suppression of cone artifacts. However, in the previous section it was shown that high α values also result in new artifacts when combined with the ordered subsets technique. These artifacts seem to consist of noise-like high-frequency effects as well as ringings with lower frequency. Since these artifacts occur only for high α values, and are restricted to certain frequency ranges, it might be possible to suppress at least the high-frequent errors by lowering the gain for these frequencies, *i.e.* low-pass filtering the updates.

Here, we examine suppression of the observed artifacts by low-pass filtering in the update step. For efficiency reasons, instead of applying the filter in the reconstruction domain, low-pass filtering has been performed in the radial direction of projection data differences $(\mathbf{P}_{i_k}\mathbf{f}_k - \mathbf{p}_{\text{in},i_k})$. The kernel used for low-pass filtering

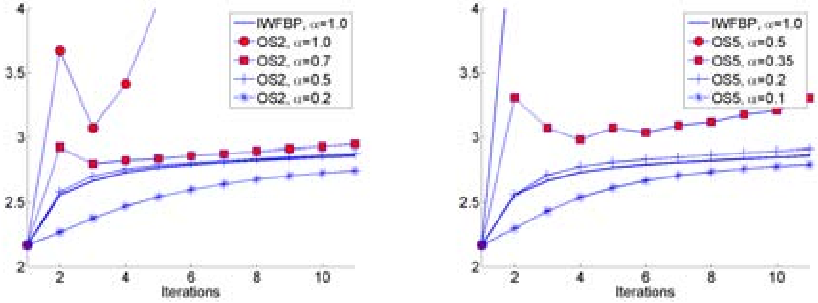

(a) 2 subsets (b) 5 subsets

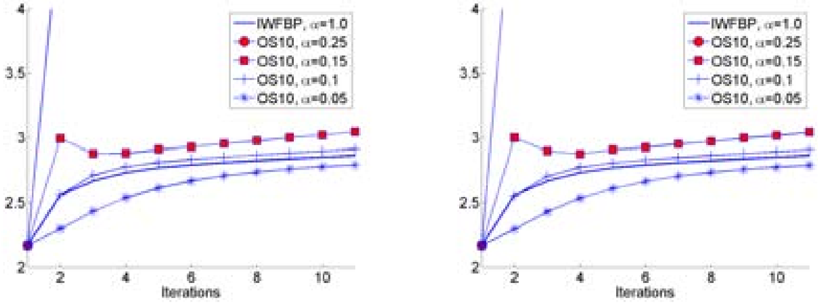

(c) 10 subsets, GR (d) 10 subsets, HLBK

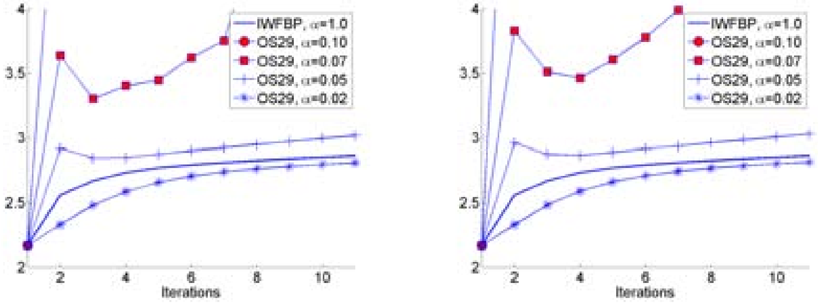

(e) 29 subsets, GR (f) 29 subsets, HLBK

Figure 6.4: 2D experiments. σ_e measurements on constant regions for 2, 5, 10 and 29 subsets. In the case of two and five subsets, the GR and HBL ordering schemes are equivalent.

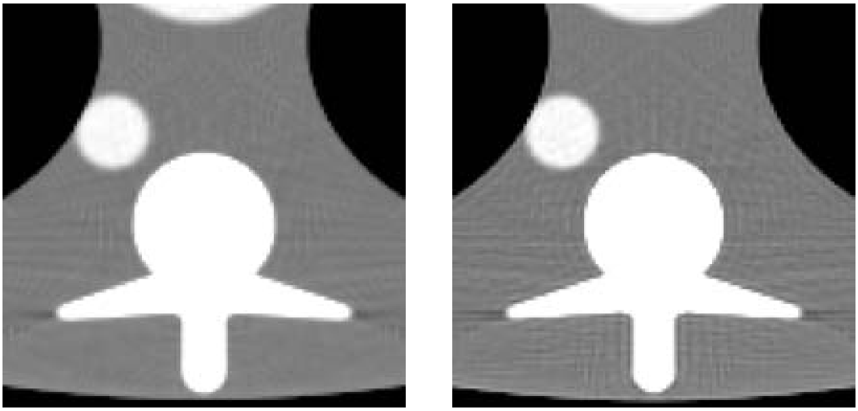

(a) WFBP reconstruction (b) IWFBP, $\mathbf{f}_3$

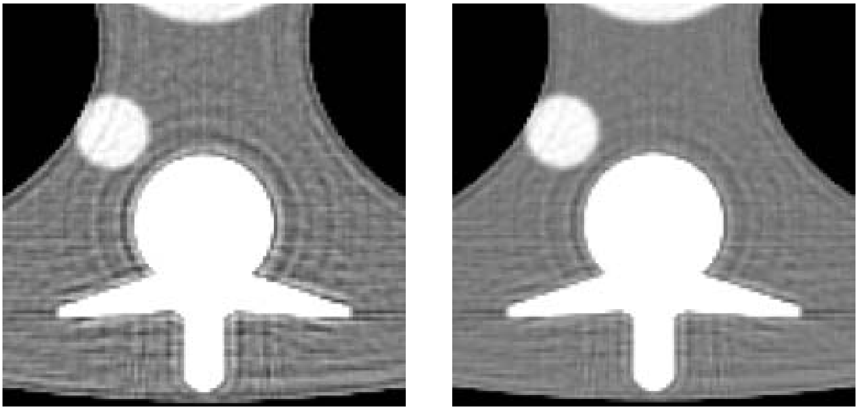

(c) OS5, $\mathbf{f}_6$ (one full iter.), $\alpha = 0.5$ (d) OS5, $\mathbf{f}_6$ (one full iter.), $\alpha = 0.35$

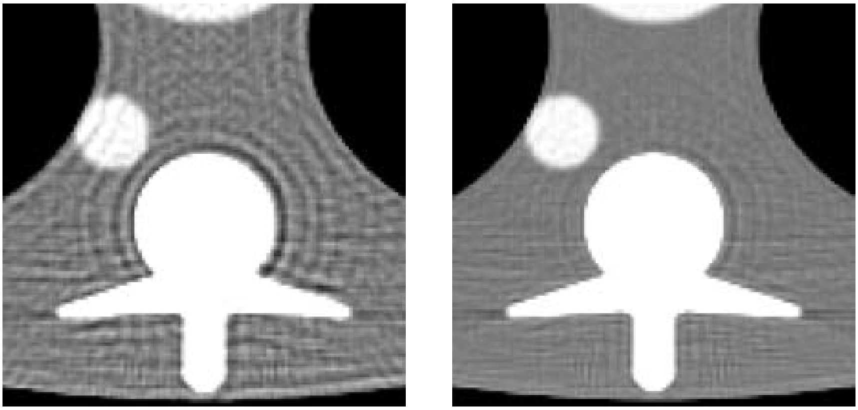

(c) OS5, $\mathbf{f}_{11}$ (two full iter.), $\alpha = 0.5$ (d) OS5, $\mathbf{f}_{11}$ (two full iter.), $\alpha = 0.35$

Figure 6.5: Reconstruction results for non-regularized IWFBP and OS-IWFBP with 5 subsets. Greyscale window ±50HU.

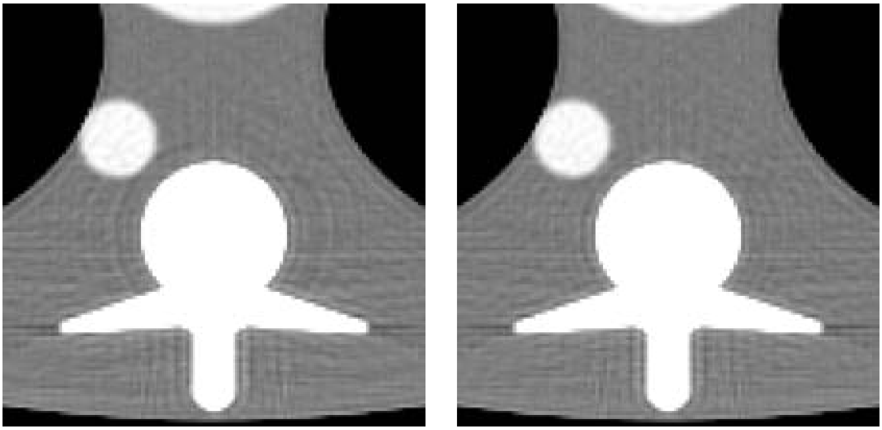

(a) OS10, GR, $\mathbf{f}_{11}$, $\alpha = 0.15$ (b) OS10, HLBK, $\mathbf{f}_{11}$, $\alpha = 0.15$

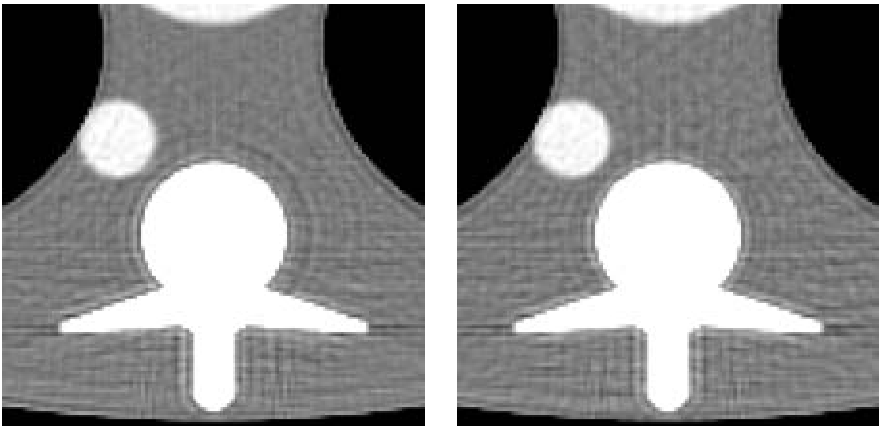

(a) OS29, GR, $\mathbf{f}_{30}$, $\alpha = 0.07$ (b) OS29, HLBK, $\mathbf{f}_{30}$, $\alpha = 0.07$

Figure 6.6: Reconstruction results from OS-IWFBP with 10 and 29 subsets after *one* full iteration. The left images were reconstructed using the GR ordering scheme and the right images using the HLBK ordering schemes. Greyscale window ±50HU.

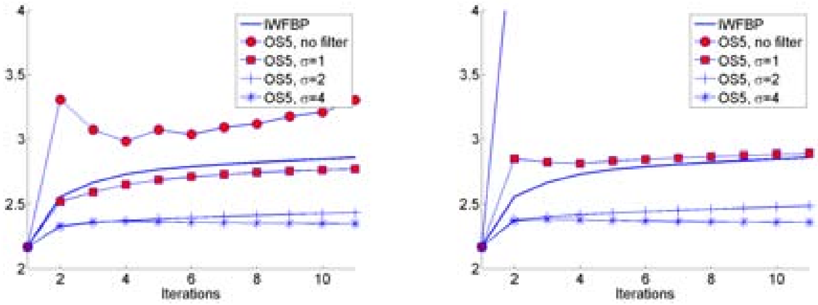

(a) 5 subsets, $\alpha = 0.35$ (b) 5 subsets, $\alpha = 0.50$

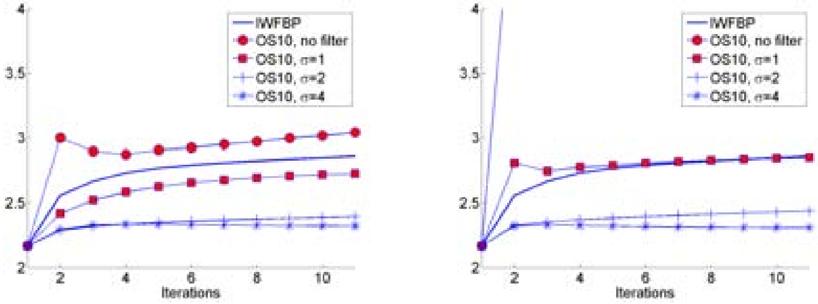

(c) 10 subsets, $\alpha = 0.15$ (d) 10 subsets, $\alpha = 0.25$

Figure 6.7: σ_e measurements on constant regions for five and ten subsets and different values of the low-pass parameter σ. By low-pass filtering projection data differences, the amount of artifacts introduced at constant regions is clearly reduced. This makes it possible to use α-values closer to unity.

is a truncated and sampled Gaussian given by

$$K_\sigma[m] = \begin{cases} \frac{1}{C}\exp\left(-\frac{m^2}{\sigma^2}\right) & , \quad m = -\frac{M-1}{2}, \ldots, \frac{M-1}{2} \\ 0 & , \quad \text{otherwise} \end{cases} \tag{6.6}$$

where $C = \sum_m \exp\left(-\frac{m^2}{\sigma^2}\right)$ so that the DC-component of the filter equals one.

Experiments have been performed with five and ten subsets using the HLBK ordering scheme. The σ-values determining the amount of low-pass filtering were set to 1, 2 and 4. Error measurements σ_e with respect to the number of iterations are shown in Figure 6.7. In all four cases, the amount of artifacts at constant regions are reduced as σ is increased. For five subsets with $\alpha = 0.50$ and ten subsets with $\alpha = 0.25$, the divergent sequences are turned into more stable sequences showing no signs of divergence during the first ten iterations.

When σ is further increased, the amount of artifacts at constant regions drops below those introduced by the ordinary IWFBP. This is mainly because increasing σ also increase the required number of iterations for high frequencies to be reconstructed. Therefore, for large σ values we expect the σ_e values to slowly increase to

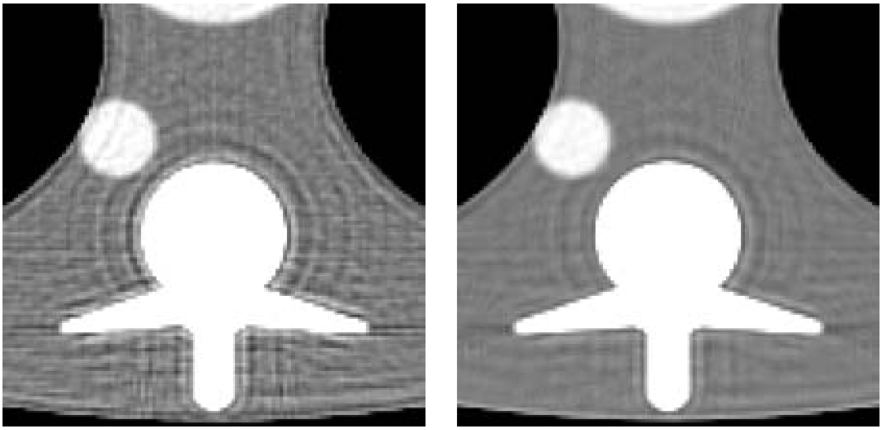

(a) 5 subsets, $\mathbf{f}_6$, no LP-filter

(b) 5 subsets, $\mathbf{f}_6$, $\sigma = 1$

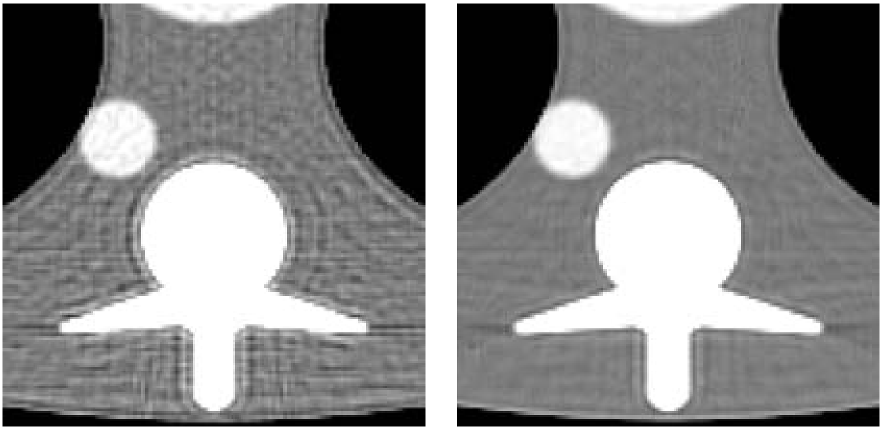

(a) 10 subsets, $\mathbf{f}_{11}$, no LP-filter

(b) 10 subsets, $\mathbf{f}_{11}$, $\sigma = 1$

Figure 6.8: Reconstruction results for the OS-IWFBP with five and ten subsets using the HLBK ordering scheme after *one* full iterations. The α values were selected so that the methods diverge without low-pass filtering, and $\sigma = 1$ was used. Greyscale window ±50HU.

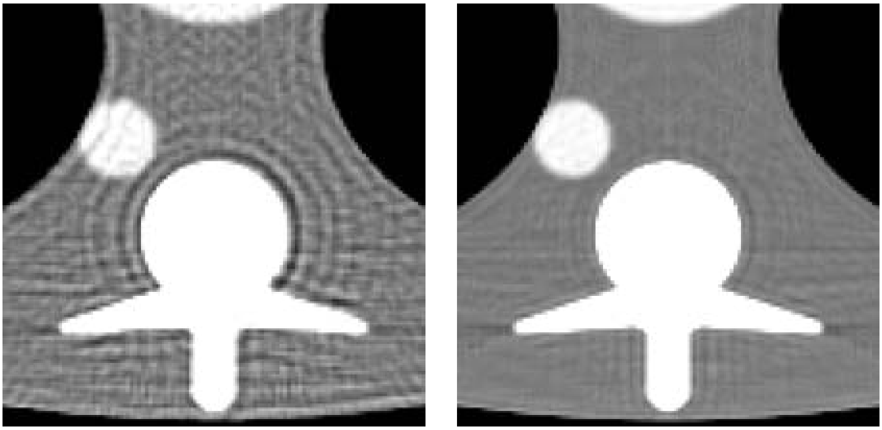

(a) 5 subsets, $\mathbf{f}_{11}$, no LP-filter

(b) 5 subsets, $\mathbf{f}_{11}$, $\sigma = 1$

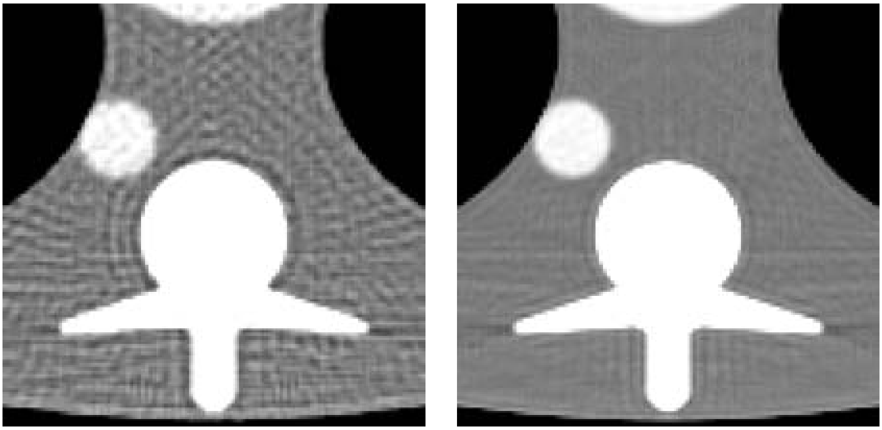

(a) 10 subsets, $\mathbf{f}_{21}$, no LP-filter

(b) 10 subsets, $\mathbf{f}_{21}$, $\sigma = 1$

Figure 6.9: Reconstruction results for the OS-IWFBP with five and ten subsets using the HLBK ordering scheme after *two* full iterations. The α values were selected so that the methods diverge without low-pass filtering, and $\sigma = 1$ was used. Greyscale window ±50HU.

levels similar to those of the ordinary IWFBP as the number of iterations increase.

6.4 Cone artifact reduction. 3D experiments.

The 2D experiments presented in Section 6.2 and 6.3 have dealt with (i) ordering of subsets, (ii) selection of α for different numbers of subsets, and (iii) low-pass filtering of updates. Guided by these results, more time-consuming three-dimensional experiments on OS-IWFBP were designed. Two subset configurations have been considered, one with five subsets and one with ten subsets ordered according to the HLBK scheme. This scheme was chosen because of the slightly better result after one full iteration with ten subsets according to Figure 6.6. For the five subset configuration, $\alpha = 0.5$ and $\alpha = 0.35$ were used together with low-pass filtering with $\sigma = 1$. For the ten subset configuration, $\alpha = 0.25$ and $\alpha = 0.15$ were used with and without low-pass filtering of updates.

RMSE and noise were measured by calculating the σ_e and σ_n values as described in Section 4.2. These results are shown in Figure 6.10. As expected, the σ_e values calculated over "cone artifact sets" drop faster for OS-IWFBP with high α-values than for ordinary IWFBP. This seems to be true also when the RMSE is measured over the "whole image" as specified in Section 4.2. From Figure 6.10, it is clear that the amplification of noise is also accelerated for OS with high α-values. Unfortunately, the difference in σ_n values between OS-IWFBP and IWFBP seem to remain after three iterations, while the difference in σ_e values between the methods is diminished. This indicates that the ordered subset technique does not only increase the rate of convergence but also increase the noise in the solution.

Figure 6.11 and 6.12 show images reconstructed with OS-IWFBP with five and ten subsets respectively. For comparison, reconstruction results obtained with ordinary IWFBP are included. Both for five and ten subsets, the observed initial reduction of cone artifacts is higher for the OS-IWFBP than for IWFBP. However, even if the result after one full iteration does not suffer from any visible cone artifacts, new ringing-like artifacts appear in the area near the vertebra. These artifacts are reduced after another iteration, but the contour of the vertebra overshoot is still not as sharp as for the ordinary IWFBP. After three iterations, the contour is sharper and its amplitude has been reduced as a sign of sharpening of the image, similar to what we can observe for ordinary non-regularized IWFBP in Figure 5.3.

In order to better relate results presented in this section to those presented in Figure 5.2, experiments have also been performed on the Turbell clock phantom [77]. The cone angles were $\pm 4.8^\circ$ and $\pm 9.6^\circ$, and the values of other scanning parameters were the same as specified in Section 4.1. Figure 6.13 show the results for $\kappa_{\max} = 4.8^\circ$. In this case, the ordered subset technique does not seem to offer much improvement to the results obtained with ordinary IWFBP. Already after one iteration, decent suppression of cone artifacts is achieved with ordinary IWFBP. The OS-IWFBP result is only marginally better. However, for the higher cone angle $\pm 9.6^\circ$ shown in Figure 6.14, the difference between the methods is more pronounced. After two iterations, there are clearly visible cone artifacts remaining

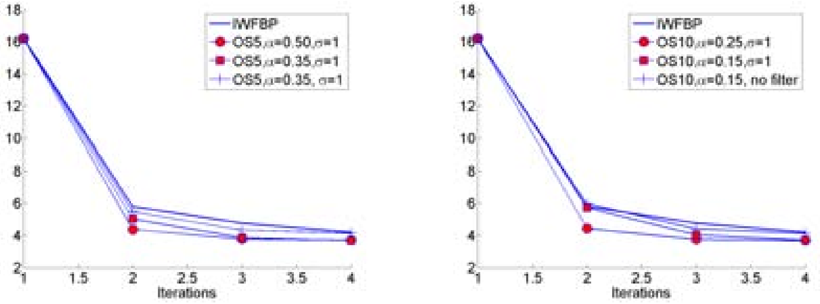

(a) OS-10, σ_e - “cone artifact areas” (b) OS-5, σ_e - “cone artifact areas”

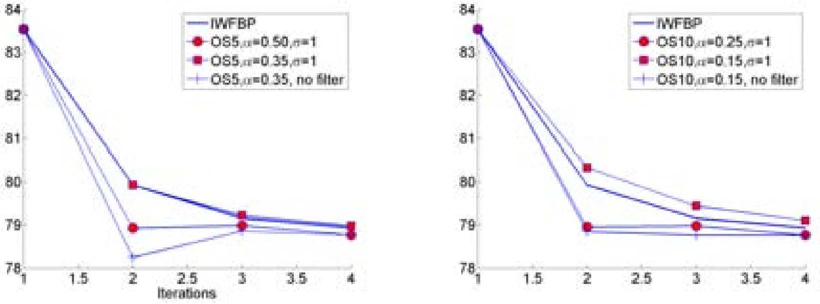

(c) OS-10, σ_e - “whole image” (d) OS-5, σ_e - “whole image”

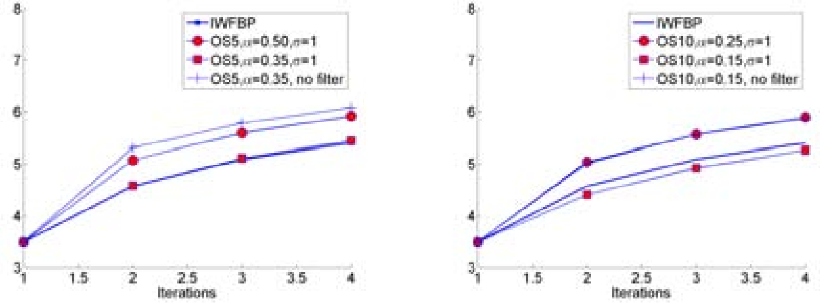

(e) OS-10, σ_n (f) OS-5, σ_n

Figure 6.10: σ_e and σ_n measurements for OS-IWFBP with five and ten subsets.

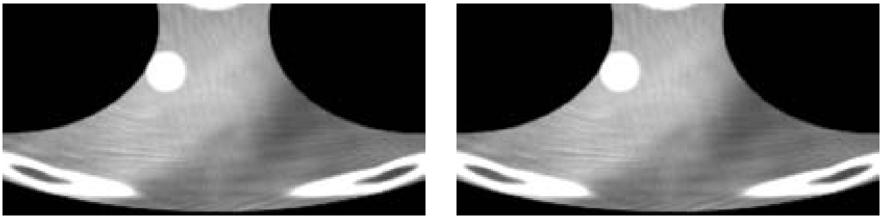

(a) IWFBP, $\mathbf{f}_1$ (b) OS5, $\mathbf{f}_1$

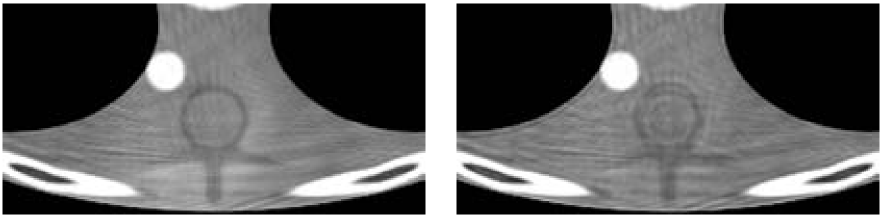

(c) IWFBP, $\mathbf{f}_2$ (d) OS5, $\mathbf{f}_6$

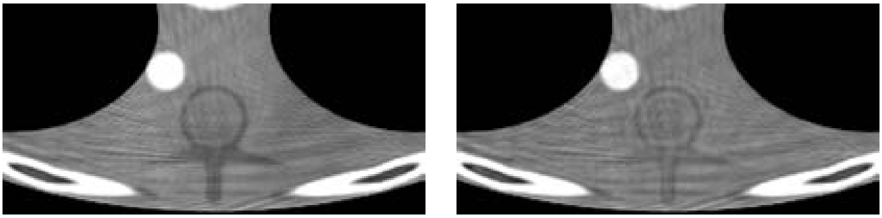

(e) IWFBP, $\mathbf{f}_3$ (f) OS5, $\mathbf{f}_{11}$

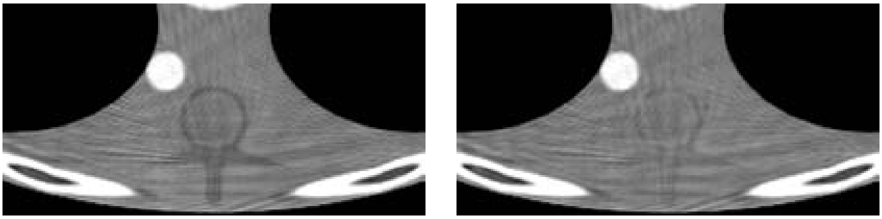

(g) IWFBP, $\mathbf{f}_4$ (h) OS5, $\mathbf{f}_{16}$

Figure 6.11: Comparison between non-regularized IWFBP and OS-IWFBP with 5 subsets. $\alpha = 0.50$ and $\sigma = 1$. Greyscale window ±50 HU.

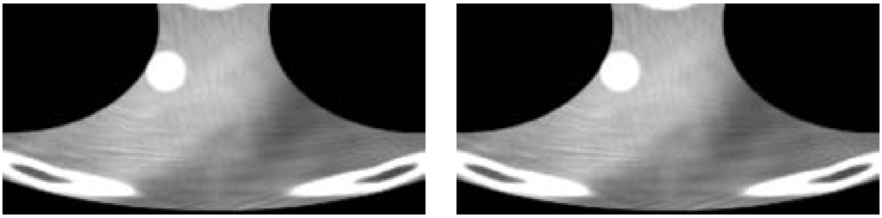

(a) IWFBP, $\mathbf{f}_1$

(b) OS10, $\mathbf{f}_1$

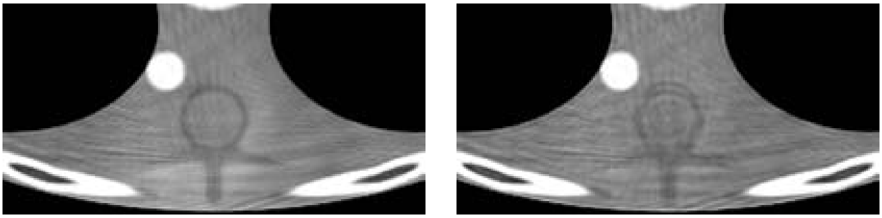

(c) IWFBP, $\mathbf{f}_2$

(d) OS10, $\mathbf{f}_{11}$

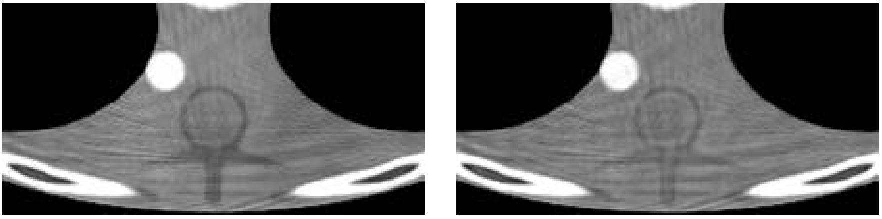

(e) IWFBP, $\mathbf{f}_3$

(f) OS10, $\mathbf{f}_{21}$

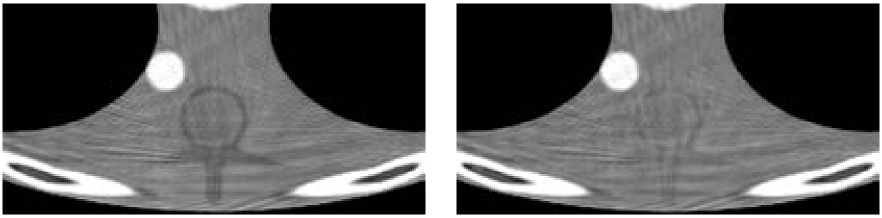

(g) IWFBP, $\mathbf{f}_4$

(h) OS10, $\mathbf{f}_{31}$

Figure 6.12: Comparison between non-regularized IWFBP and OS-IWFBP with 10 subsets ordered according to the HLBK scheme. $\alpha = 0.25$ and $\sigma = 1$. Greyscale window ±50 HU.

in the ordinary IWFBP result, while in terms of cone artifacts, the image produced by OS-IWFBP is close to perfect.

The reconstruction results in Figure 6.13 contain so called windmill artifacts: diverging streak patterns that occur close to high gradients in the z-direction. These artifacts were examined by Silver *et al.* [69] and are slightly more pronounced after two full OS-iterations than after two simultaneous iterations.

6.5 Conclusions

From the experiments presented in Section 6.2 we conclude that if the α-values are chosen approximately as $1/N_{\text{sets}}$, the proposed OS-IWFBP algorithm works in two-dimensions without introducing severe artifacts during the first iterations.

Only subtle differences have been noted for ordering schemes and subset configurations presented in Section 6.2. Since no experiments have been made with larger number of subsets than 29, perhaps larger differences can be found for a large number of subsets.

The value of α should be as high as possible to get maximal suppression of cone artifacts. For a certain subset configuration, it was shown in Section 6.3 that a low-pass filter prior to backprojection reduces the ringing and the noise-like artifacts caused by a high α-value in the update step. Our filter was a Gaussian with $\sigma = 1$, which made it possible to avoid artifacts otherwise apparent when $\alpha = 0.25$ for ten subsets and $\alpha = 0.50$ for five subsets. One side-effect of this low-pass filtering is reduced convergence rate for high frequencies. This could lead to blurred results in the first iterations before the high frequencies have converged. However, $\sigma = 1$ does not seem to change the spatial resolution of the images after two iterations to any appreciable extent.

The main motivation for combining the ordered subsets technique with the IWFBP algorithm is to accelerate the suppression of cone artifacts, hopefully so much that only one iteration is needed. Indeed, in Section 6.4 it was shown that for this scanning configuration, the cone-artifacts caused by WFBP can be almost perfectly suppressed after one iteration. However, near edges, new ringing artifacts appear. Another unfortunate side effect seems to be that noise is amplified more than for the ordinary IWFBP.

From Figure 5.2, one may conclude that an almost perfect result can be obtained after only one iteration. Unfortunately, this conclusion only holds when input data are generated by the operator $\mathbf{P}$ used for projection generation in the iterative loop. We have now shown that under more realistic circumstances, such as a non-bandlimited object of interest and inconsistencies in input data due to noise, the highest possible acceleration is lower than shown in Figure 5.2 (cf. Figure 6.14). The relatively small improvement comparison with ordinary IWFBP for reasonable realistic input data and cone angles smaller than 4.8° combined with the poor noise properties makes the OS-IWFBP technique less interesting than have been expected from the seemingly impressive result in Figure 5.2.

Another drawback of the OS-IWFBP technique is that it is more difficult to understand than ordinary IWFBP in terms of convergence and the possible ex-

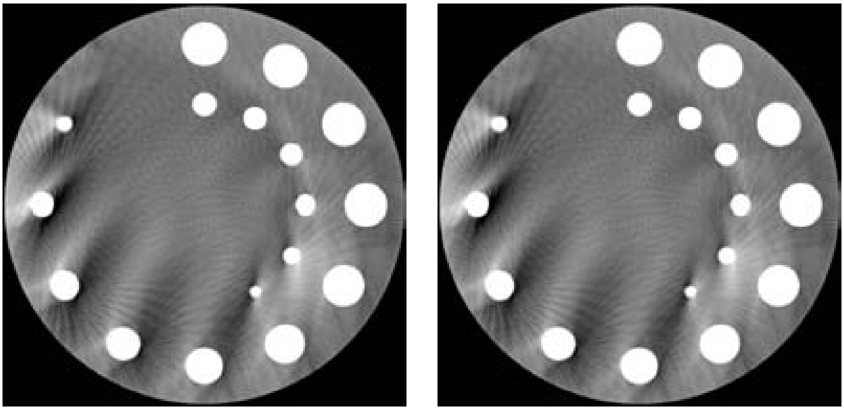

(a) IWFBP, $\mathbf{f}_1$ (b) OS10, $\mathbf{f}_1$

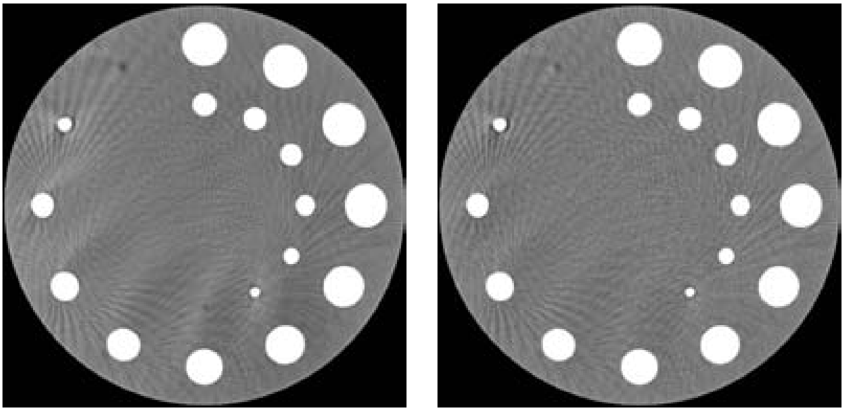

(c) IWFBP, $\mathbf{f}_2$ (d) OS10, $\mathbf{f}_{11}$

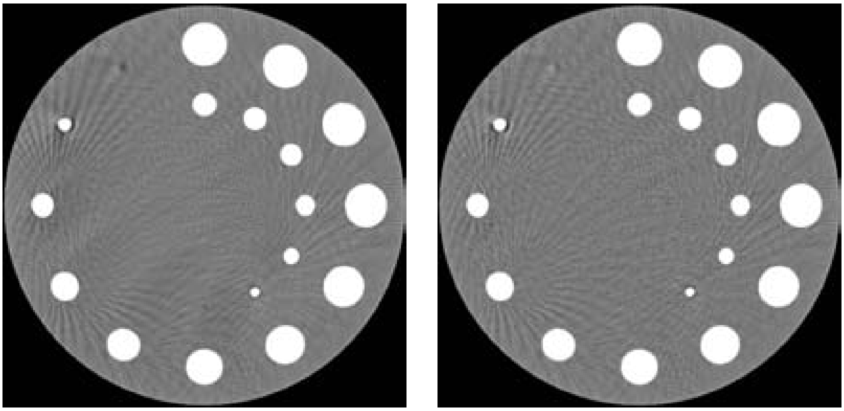

(e) IWFBP, $\mathbf{f}_3$ (f) OS10, $\mathbf{f}_{21}$

Figure 6.13: Clock phantom reconstructions with non-regularized IWFBP and OS-IWFBP with 10 subsets respectively. Cone angle $\kappa \approx \pm 4.8°$. Greyscale window ±50 HU.

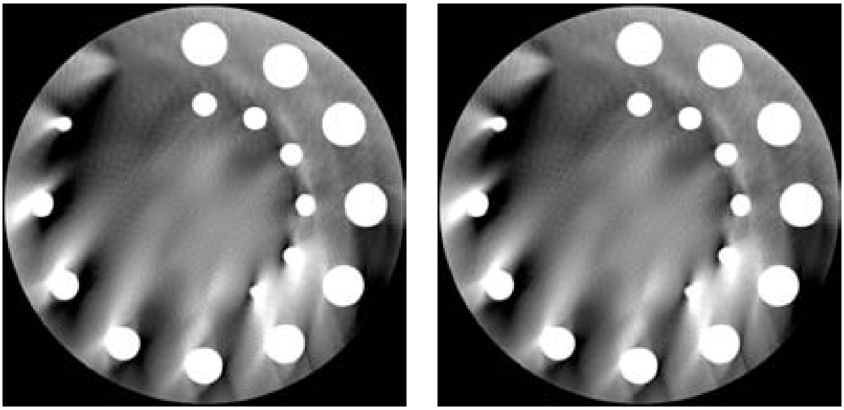

(a) IWFBP, $\mathbf{f}_1$ (b) OS10, $\mathbf{f}_1$

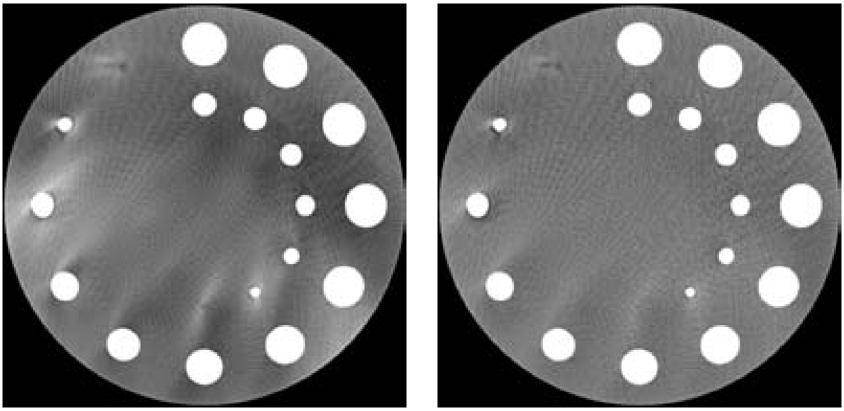

(c) IWFBP, $\mathbf{f}_2$ (d) OS10, $\mathbf{f}_{11}$

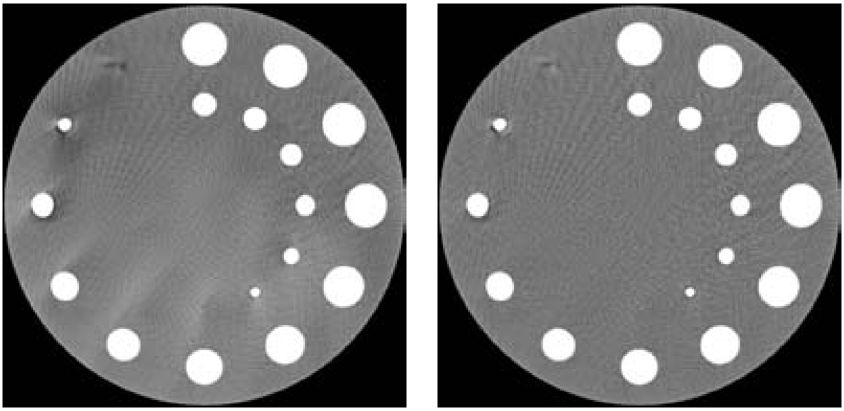

(e) IWFBP, $\mathbf{f}_3$ (f) OS10, $\mathbf{f}_{21}$

Figure 6.14: Clock phantom reconstructions with non-regularized IWFBP and OS-IWFBP with 10 subsets respectively. Cone angle $\kappa \approx \pm 9.6^\circ$. Greyscale window ±50 HU.

istence of a fixed point. This makes it hard to predict good parameters and to augment the loop with, for instance the regularization concept from the previous chapter.

Chapter 7

Frequency domain partitioning (FDP) of projection data

7.1 Introduction

In Section 5, it was shown how IWFBP can be used to suppress cone artifacts in a few iterations. Unfortunately, to avoid new artifacts caused by the iterative scheme, reconstruction must be made to a sampling density that is unnecessarily high with respect to the Nyquist limit of the input data. Another drawback is that in contrast to non-iterative WFBP, the whole region of interest (ROI) must be reconstructed even if just a small part is to be studied. Thus, it is interesting to find ways to make the computation of one iteration cheaper.

Here, we examine a method that could make it possible to reduce the computational cost by reducing the amount of data that the iterative loop operates on. This method was suggested by Danielsson [10] and is illustrated in Figure 7.1. The first step is to divide the projection data after rebinning $\mathbf{p}_{\text{reb}}$ into two parts; one part $\mathbf{p}_{\text{LF}} = \mathbf{H}_{\text{LP}}\mathbf{p}_{\text{reb}}$ containing only low frequencies in the radial direction and one part $\mathbf{p}_{\text{HF}} = (\mathbf{I} - \mathbf{H}_{\text{HP}})\mathbf{p}_{\text{reb}}$ containing only high frequencies. In the next step, $\mathbf{p}_{\text{LF}}$ is reconstructed with IWFBP while the high-frequency part $\mathbf{p}_{\text{HF}}$ is reconstructed with the non-iterative WFBP. Hence, the reconstruction result is given by

$$\mathbf{f} = \mathbf{Q}_{\text{IWFBP}}\mathbf{H}_{\text{LP}}\mathbf{p}_{\text{reb}} + \mathbf{Q}_{\text{WFBP}}(\mathbf{I} - \mathbf{H}_{\text{LP}})\mathbf{p}_{\text{reb}}, \tag{7.1}$$

where $\mathbf{Q}_{\text{WFBP}}$ and $\mathbf{Q}_{\text{IWFBP}}$ are the matrices corresponding to the WFBP and IWFBP method respectively. This method will in the following be referred to as the frequency domain partitioning (FDP) method.

The LP filter represented by $\mathbf{H}_{\text{LP}}$ in (7.1) is defined in the Fourier domain by

$$H_{\text{LP}}(u) = \begin{cases} 1 & , \quad 0 \leq u \leq u_{\text{pass}} \\ \cos^2\left(\frac{\pi}{2}\frac{u - u_{\text{pass}}}{u_{\text{stop}} - u_{\text{pass}}}\right) & , \quad u_{\text{pass}} < u < u_{\text{stop}} \\ 0 & , \quad u_{\text{stop}} \leq u \leq u_{\text{nyq}} \end{cases} , \tag{7.2}$$

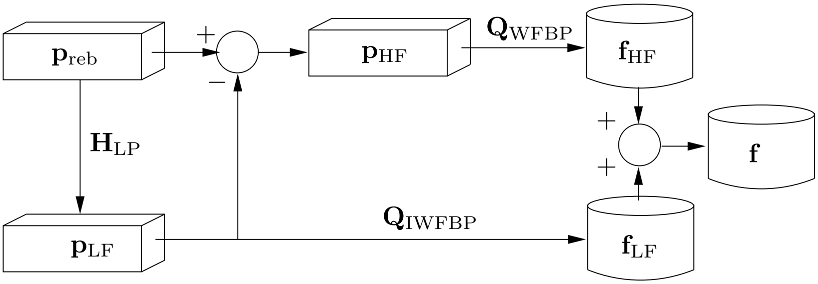

Figure 7.1: Illustration of the FDP method. Rebinned projection data are divided into one part $\mathbf{p}_{\text{HF}}$ containing high radial frequencies and one part $\mathbf{p}_{\text{LF}}$ containing low radial frequencies. The high-frequency part is reconstructed with the non-iterative WFBP and the low-frequency part is reconstructed with the IWFBP method. Finally, the reconstruction results $\mathbf{f}_{\text{HF}}$ and $\mathbf{f}_{\text{LF}}$ are added together.

where u_{pass} defines the point where the amplitude spectrum starts to drop from one to zero, and u_{stop} defines the point where the spectrum reaches zero. u_{nyq} is the Nyquist frequency in the radial direction of projection data. In the following experiments, the value of u_{pass} has been fixed to the relatively low $0.05u_{\text{nyq}}$ in order to make the transition $u_{\text{stop}} - u_{\text{pass}}$ as long as possible. In order to study how the choice of this parameter affect the result, the value of u_{stop} has been varied between $0.1u_{\text{nyq}}$ to $0.6u_{\text{nyq}}$ as shown in Figure 7.2.

As previously mentioned, one motivating property of the FDP method is speed. If the low-frequency part in Figure 7.1 can be implemented with downsampled input and output data, a high number of iterations will be less painful.

A necessary condition is that $\mathbf{p}_{\text{HF}}$ can do its task without iterations, *i.e.* without being afflicted by cone artifacts. The amount of cone artifacts produced by the WFBP method when applied to LP- and HP-filtered data has been examined by studying differences between 2D and 3D reconstructions. Figure 7.3 show these differences for HP-filtered input data. Clearly, the cone artifacts caused by the high z-gradient close to the vertebra is absent in these images. In contrast, we see in Figure 7.4 that this cone artifact is preserved when input data are LP-filtered. This serves as a motivation for the following experiments.

7.2 Impact of the parameter u_{stop}

In order to evaluate the frequency domain partitioning scheme described in the previous section, the configuration described in Chapter 4 has been used. The values of the parameter u_{stop} have been set to $0.1u_{\text{nyq}}$, $0.2u_{\text{nyq}}$, $0.4u_{\text{nyq}}$ and $0.6u_{\text{nyq}}$. If the image matrix sampling density is approximately 1mm (true when $N_x = 513$), the image matrix sampling density equals 1.3 times the radial detector sampling density. Therefore, the above values of u_{stop} correspond to 0.13, 0.26, 0.52 and 0.78 times the Nyquist frequency of the image matrix.

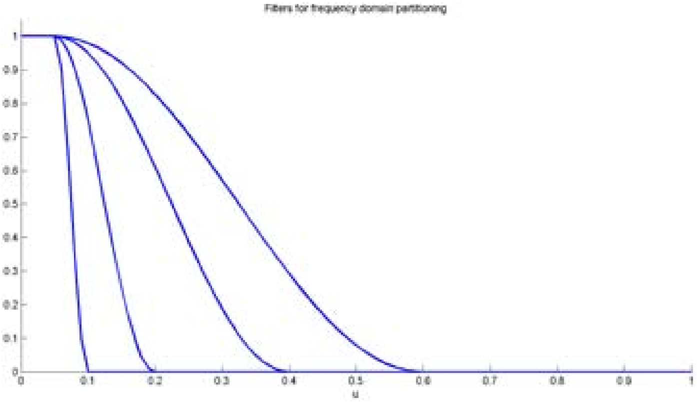

Figure 7.2: Amplitude spectra for the filters H_{LP} used for frequency domain partitioning. Corresponding high-pass filters are defined as $H_{\text{HP}}(u) = 1 - H_{\text{LP}}(u)$.

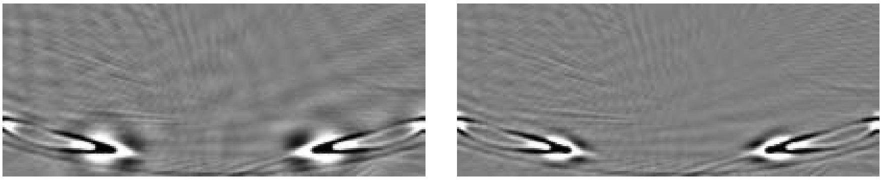

(a) $u_{\text{stop}} = 0.1u_{\text{nyq}}$ (b) $u_{\text{stop}} = 0.2u_{\text{nyq}}$

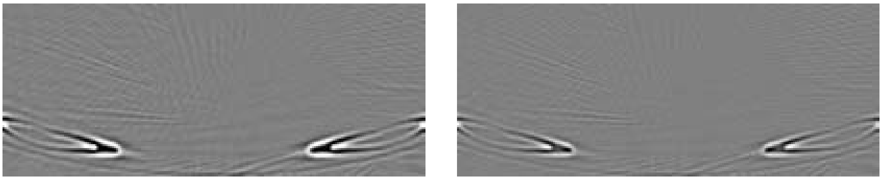

(c) $u_{\text{stop}} = 0.4u_{\text{nyq}}$ (d) $u_{\text{stop}} = 0.6u_{\text{nyq}}$

Figure 7.3: Differences between two-dimensional and non-exact three-dimensional reconstructions of HP-filtered projection data for four different frequencies. Note the absence of cone artifacts compared to the results for LP-filtered data in Figure 7.4.

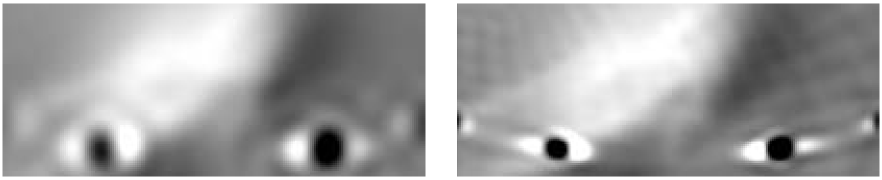

(a) $u_{\text{stop}} = 0.1u_{\text{nyq}}$

(b) $u_{\text{stop}} = 0.2u_{\text{nyq}}$

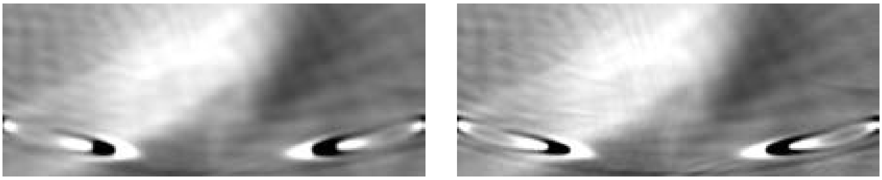

(c) $u_{\text{stop}} = 0.4u_{\text{nyq}}$

(d) $u_{\text{stop}} = 0.6u_{\text{nyq}}$

Figure 7.4: Differences between two-dimensional and non-exact three-dimensional reconstructions of LP-filtered projection data for four different frequencies. The cone artifact close to the vertebra is clearly preserved when the projection data are LP-filtered prior to WFBP reconstruction.

Figure 7.5 and 7.6 show axial slices of noise-free Thorax phantom reconstructions with WFBP, FDP after five iterations with different values of u_{stop}, and non-regularized IWFBP after five iterations. The grey scale window is ±30HU, *i.e.* slightly narrower than the greyscale windows used in Chapter 5 and 6. Three different slices are shown for each value of u_{stop}. These slices are located at (top to bottom) $z \approx -10$mm, $z \approx -11$mm, and $z \approx -12$mm. The cone artifact apparent in the WFBP result seem to be suppressed for all choices of u_{stop}. However, for $u_{\text{stop}} = 0.1u_{\text{nyq}}$ and $u_{\text{stop}} = 0.2u_{\text{nyq}}$, new low-frequent "blob" artifacts appear close to high z-gradients. This effect is also observed in the Figure 7.7 showing zoomed saggital slices of the same reconstruction results. For $u_{\text{stop}} = 0.1u_{\text{nyq}}$ and $u_{\text{stop}} = 0.2u_{\text{nyq}}$, the "blob" artifact is observed as a dark strip between the bottom of the rib and the bottom of the sharp part of the vertebra.

Table 7.1 shows σ_e and σ_n values for the FDP method. The initial reduction of σ_e measured over "cone artifact sets" when u_{stop} is increased from $0.1u_{\text{nyq}}$ to $0.2u_{\text{nyq}}$ could be explained by a reduction of "blob" artifacts and improved cone-artifact suppression. When u_{stop} is further increased, these σ_e values increase due to more streak artifacts similar to those obtained with non-regularized IWFBP. σ_e measured over "the whole image" is reduced when u_{stop} is increased, *i.e.* when the FDP is becoming more similar to the non-regularized IWFBP. The noise measure σ_n shows a similar behavior. For low values of u_{stop}, the noise properties are more similar to those of WFBP, and for high values of u_{stop}, the noise properties are more similar to those of IWFBP.

Spatial resolution properties of the FDP method have been examined by measuring modulation transfer functions (MTFs) and slice sensitivity profiles (SSPs) as described in Chapter 4. The MTFs are shown in Figure 7.8a. For low frequencies, the values of the FDP MTFs are close to those of the IWFBP method.

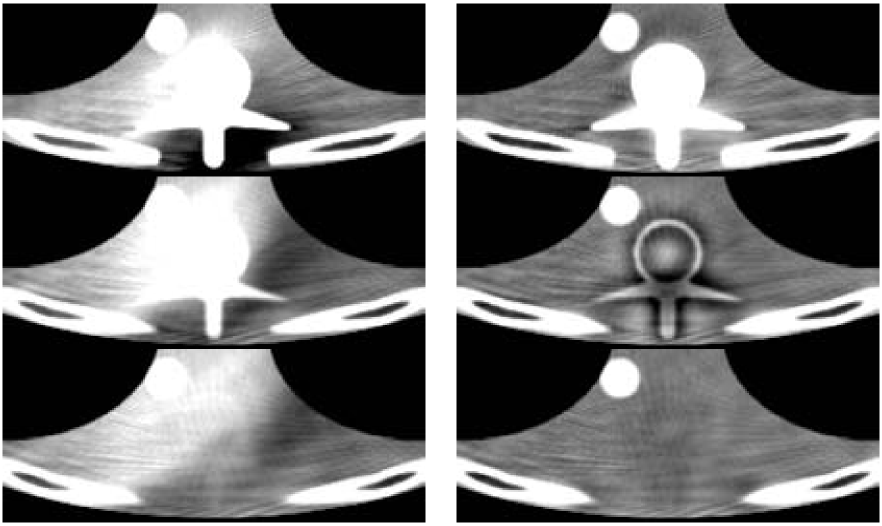

(a) WFBP reconstruction (b) FDP, $\mathbf{f}_6$, $u_{\text{stop}} = 0.1u_{\text{nyq}}$

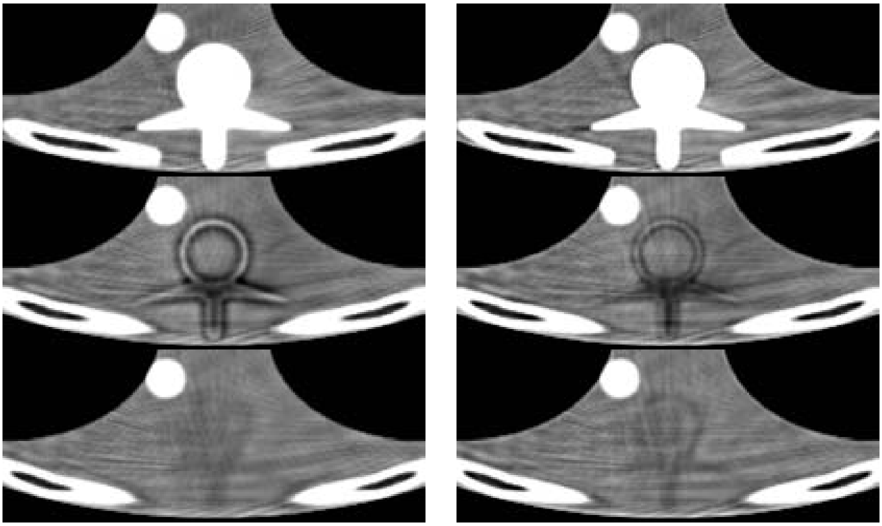

(c) FDP, $\mathbf{f}_6$, $u_{\text{stop}} = 0.2u_{\text{nyq}}$ (d) FDP, $\mathbf{f}_6$, $u_{\text{stop}} = 0.4u_{\text{nyq}}$

Figure 7.5: Axial slices of non-regularized FDP reconstructions of the Thorax phantom for different values of u_{stop}. For each value of u_{stop}, three axial slices are shown. The locations of these slices are given by (top to bottom) $z \approx -10\text{mm}$, $z \approx -11\text{mm}$ and $z \approx -12\text{mm}$. See also Figure 7.6. Grey scale window ±30HU.

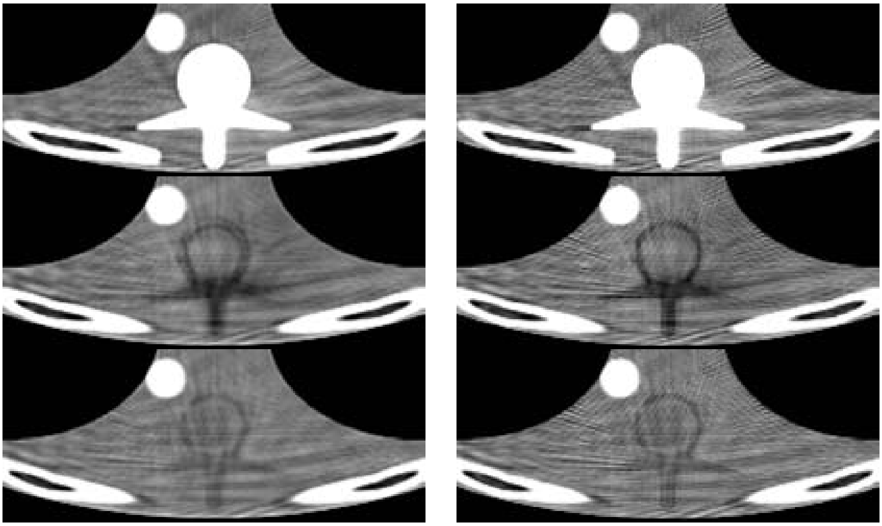

(a) FDP, $\mathbf{f}_6$, $u_{\text{stop}} = 0.6u_{\text{nyq}}$ (b) Non-regularized IWFBP, $\mathbf{f}_6$

Figure 7.6: Axial slices of non-regularized FDP reconstructions of the Thorax phantom for different values of u_{stop}. For each value of u_{stop}, three axial slices are shown. The locations of these slices are given by (top to bottom) $z = -10\text{mm}$, $z = -11\text{mm}$ and $z = -12\text{mm}$. See also Figure 7.5. Grey scale window ±30HU.

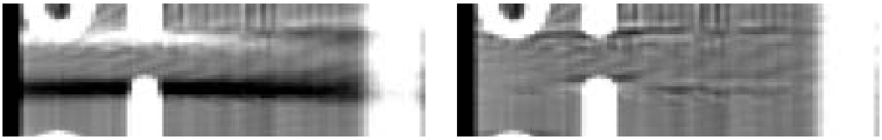

(a) WFBP reconstruction (b) FDP, $\mathbf{f}_6$, $u_{\text{stop}} = 0.1u_{\text{nyq}}$

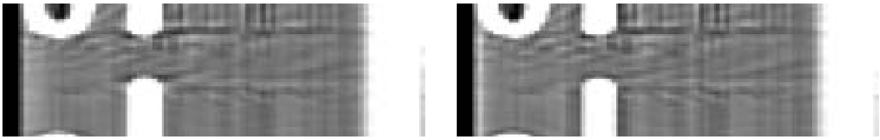

(c) FDP, $\mathbf{f}_6$, $u_{\text{stop}} = 0.2u_{\text{nyq}}$ (d) FDP, $\mathbf{f}_6$, $u_{\text{stop}} = 0.4u_{\text{nyq}}$

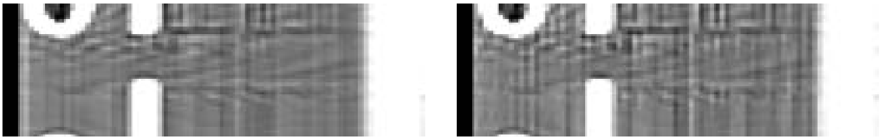

(e) FDP, $\mathbf{f}_6$, $u_{\text{stop}} = 0.6u_{\text{nyq}}$ (f) Non-regularized IWFBP, $\mathbf{f}_6$

Figure 7.7: Saggital slices of FDP reconstructions of the Thorax phantom for different values of u_{stop}. Grey scale window ±30HU.

Table 7.1: σ_e and σ_n values after five iterations for different values of u_{stop}. Images shown in Figure 7.5, 7.6 and 7.7.

β	σ_e (HU) cone artifact areas	σ_e (HU) whole image	σ_n (HU)
WFBP	16.21	83.54	3.50
FDP, $u_{\text{stop}} = 0.1u_{\text{nyq}}$	3.91	83.47	3.53
FDP, $u_{\text{stop}} = 0.2u_{\text{nyq}}$	3.40	83.18	3.65
FDP, $u_{\text{stop}} = 0.4u_{\text{nyq}}$	3.44	81.96	4.15
FDP, $u_{\text{stop}} = 0.6u_{\text{nyq}}$	3.56	80.71	4.68
IWFBP, $\beta = 0.0000$	4.00	78.80	5.78

Depending on the value of u_{stop}, as the frequency is increased, the FDP MTFs look more similar to those of the ordinary WFBP. In two dimensions, the Fourier slice theorem can be used to deduce that the MTF of the FDP method is given by

$$\text{MTF(FDP)} = H_{\text{LP}} \times \text{MTF(IWFBP)} + (1 - H_{\text{LP}}) \times \text{MTF(WFBP)}. \qquad (7.3)$$

Figure 7.8b shows the difference between the actual MTF and this prediction for $u_{\text{stop}} = 0.4u_{\text{nyq}}$. Clearly, at least for this value of u_{stop}, the difference is very small also in this cone-beam case.

SSP measurements are shown in Figure 7.9. For low values of u_{stop}, the SSP of the FDP method seem to be similar to that of the WFBP method. When u_{stop} is increased, this SSP becomes more similar to the IWFBP SSP. For $u_{\text{stop}} = 0.4u_{\text{nyq}}$ and $u_{\text{stop}} = 0.6u_{\text{nyq}}$, it is very difficult to distinguish between the SSP of the non-regularized IWFBP reconstruction and the SSP of the FDP method.

In Table 7.2, Q_1 and Q_2 values for the different methods are shown. Since for low values of u_{stop}, noise and axial spatial resolution properties are preserved while the spatial resolution in z-direction is increased, Q_1 and Q_2 values for these values of u_{stop} are high. However, it is not obvious that the FDP is better than WFBP for these values of u_{stop}, since new artifacts are introduced. Again, as concluded in Chapter 5, it does not seem reasonable to use Q_1 and Q_2 for comparing methods at different spatial resolutions since this measure is equivariant with very simple filtering operations that modify the spatial resolution.

7.3 Regularization

From the previous section, or more specifically Figure 7.8, we know that the MTF of the FDP method is approximately given by Equation (7.3). If the transition band is very narrow, *i.e.* $u_{\text{stop}} - u_{\text{pass}}$ is small, and the difference between MTF(IWFBP) and MTF(WFBP) is large in this transition band, the slope of the resulting MTF will be large in this band. This might be a source of artifacts. For instance, if $u_{\text{stop}} - u_{\text{pass}}$ is close to zero, the FDP MTF will be close to discontinuous in the transition band, resulting in ringing artifacts.

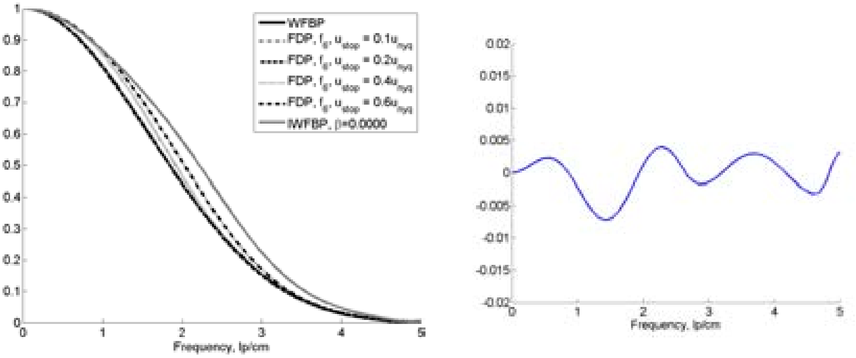

(a) MTF measurements (b) Prediction error

Figure 7.8: **a)** MTF measurements for WFBP, IWFBP, and FDP with different values of u_{stop}. For low frequencies, the MTF of the FDP method is similar to that of the IWFBP method, while for high frequencies, the MTF of the FDP method is similar to that of the WFBP method. The plots corresponding to $u_{\mathrm{stop}} = 0.1u_{\mathrm{nyq}}$ and $u_{\mathrm{stop}} = 0.2u_{\mathrm{nyq}}$ are difficult to see since they nearly coincide with the WFBP. **b)** Difference between the MTF for FDP with $u_{\mathrm{stop}} = 0.4u_{\mathrm{nyq}}$ and the corresponding prediction suggested by the Fourier slice theorem in two dimensions (see accompanying text for details).

Table 7.2: $Q_1 = c/(\sigma^2\rho_{10\%}^{-3}SD)$, $Q_2 = c/(\sigma^2\rho_M^{-3}SD)$ and the entities used for calculating these figures of merit for different values of u_{stop}. The dose is excluded, since it is kept constant.

u_{stop}	σ_n (HU)	$\rho_{10\%}$ (cm^{-1})	$\rho_{50\%}$ (cm^{-1})	S (mm)	Q_1	Q_2
WFBP	3.50	3.30	1.84	2.01	1.47	0.69
$0.1u_{\mathrm{nyq}}$	3.53	3.30	1.84	1.77	1.63	0.77
$0.2u_{\mathrm{nyq}}$	3.65	3.29	1.84	1.67	1.61	0.76
$0.4u_{\mathrm{nyq}}$	4.15	3.35	1.92	1.62	1.31	0.64
$0.6u_{\mathrm{nyq}}$	4.68	3.55	2.03	1.62	1.06	0.55
IWFBP	5.78	3.55	2.22	1.62	0.83	0.44

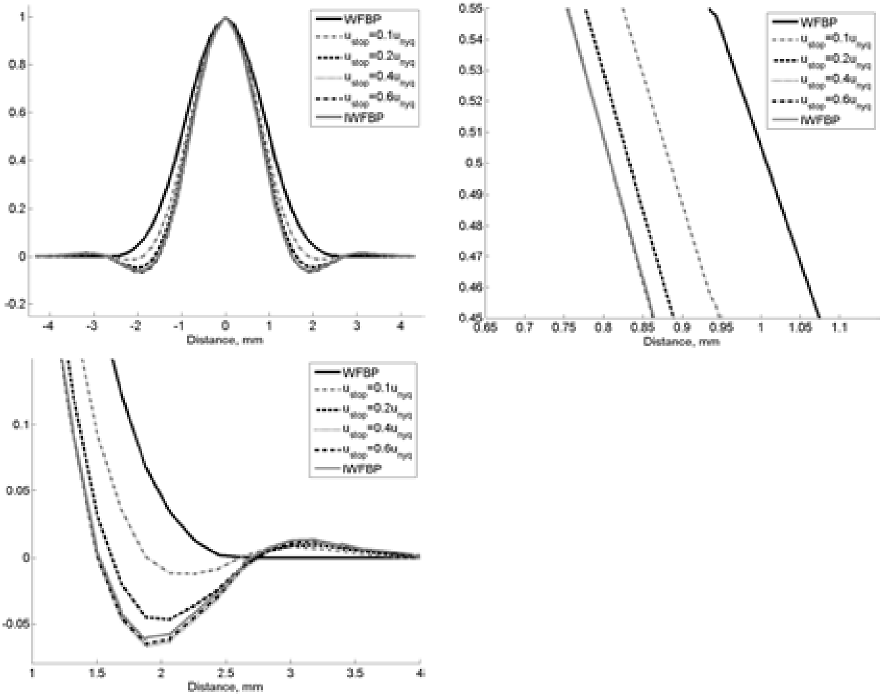

Figure 7.9: SSP measurements for WFBP, IWFBP, and FDP with different values of u_{stop}. As u_{stop} is reduced towards zero, the SSP of the FDP method becomes increasingly similar to that of the WFBP method, and when u_{stop} is increased towards u_{nyq}, the SSP of the FDP method becomes increasingly similar to that of the IWFBP method. The plots for $u_{\text{stop}} = 0.4u_{\text{nyq}}$ and $u_{\text{stop}} = 0.6u_{\text{nyq}}$ are almost indistinguishable from the IWFBP SSP.

Table 7.3: σ_e and σ_n values for regularized FDP with $\beta = 0.0005$ after five iterations for different values of u_{stop}. Images shown in Figure 7.10, 7.11 and 7.12.

β	σ_e (HU) cone artifact areas	σ_e (HU) whole image	σ_n (HU)
WFBP	16.21	83.54	3.50
FDP, $u_{\text{stop}} = 0.1u_{\text{nyq}}$	3.65	83.54	3.51
FDP, $u_{\text{stop}} = 0.2u_{\text{nyq}}$	3.37	83.47	3.55
FDP, $u_{\text{stop}} = 0.4u_{\text{nyq}}$	3.30	83.23	3.72
FDP, $u_{\text{stop}} = 0.6u_{\text{nyq}}$	3.29	83.01	3.87
IWFBP, $\beta = 0.0005$	3.27	83.41	3.79

By regularizing the IWFBP method as described in Chapter 5, the difference between the WFBP and IWFBP MTFs can be made comparably small. Thus, the above described effect can be suppressed by using regularized IWFBP instead of non-regularized IWFBP. This have been examined by repeating the experiments in the previous section, but with $\beta = 0.0005$ in the iterative scheme.

Figure 7.10, 7.11 and 7.12 show result images from these experiments. Clearly, the difference between FDP results and WFBP results in terms of edge response and aliasing artifacts looks smaller than in the non-regularized case. The amplitude of the “blob” artifacts for low values of u_{stop} also seem to have diminished. One effect that might be related to the “blob” artifact is that as u_{stop} is reduced, the overshoots close to z-gradients become increasingly blurred in the xy-plane. At the same time, the amplitude of the overshoots is reduced.

Table 7.3 shows the σ_e and σ_n values for the regularized FDP method. In contrast to the non-regularized FDP experiment, the σ_e value measured over “cone artifact sets” is now monotonically decreasing as u_{stop} is increased. This supports the explanation for increasing σ_e values given in the last section, since for regularized FDP, aliasing artifacts are not increased as u_{stop} is increased. The σ_e values measured over the “whole image” set defined in Section 4.2 are seemingly unaffected by the choice of u_{stop}.

The MTFs for the regularized FDP method are shown in Figure 7.13. As expected, these are very similar to each other. Even if it is not clear from Figure 7.13, the FDP MTFs follow the IWFBP MTFs for frequencies below the transition band and the WFBP MTFs for frequencies above the transition band.

Figure 7.14 show the SSPs for the regularized FDP method. These are slightly wider than for the non-regularized FDP method, and the amplitude is slightly lower. Apart from this, the SSPs of the non-regularized and regularized FDP are very similar.

7.4 Image matrix sampling densities

One conclusion in Chapter 5 was that in order not to enhance aliasing artifacts more than necessary, reconstruction must be made to a grid with higher density

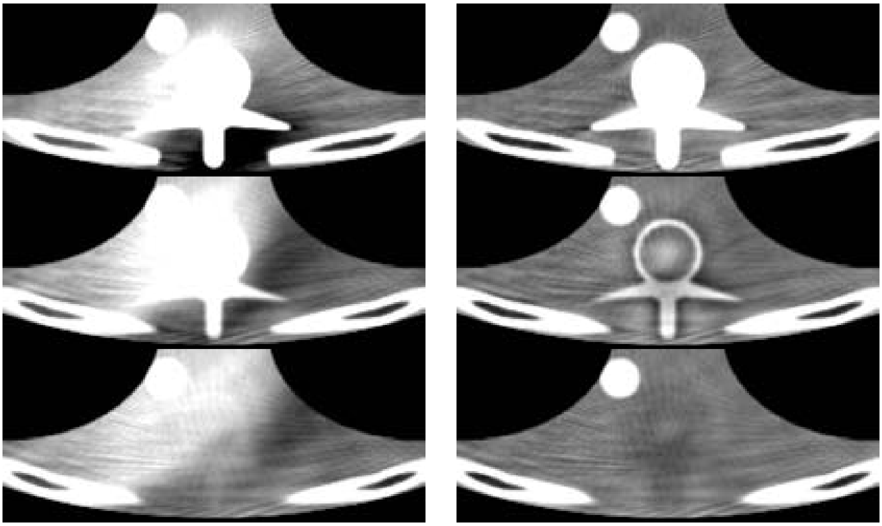

(a) WFBP reconstruction (b) FDP, $\mathbf{f}_6$, $u_{\text{stop}} = 0.1u_{\text{nyq}}$

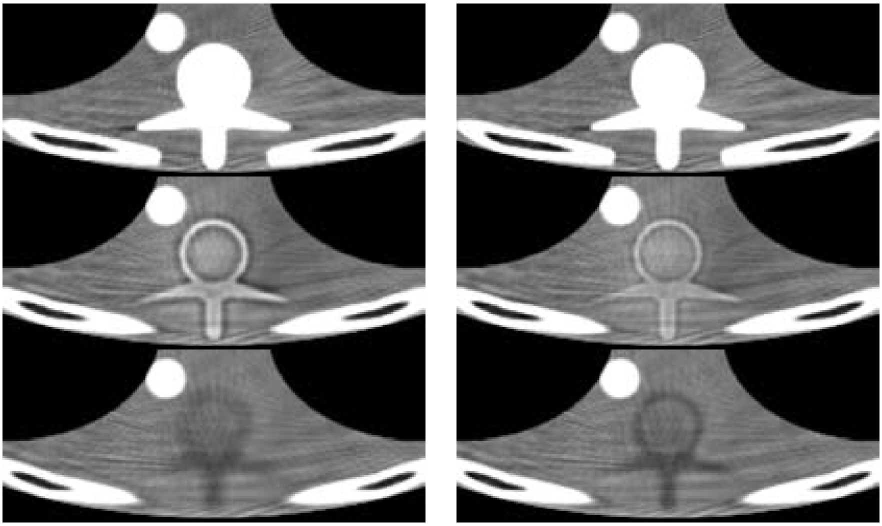

(c) FDP, $\mathbf{f}_6$, $u_{\text{stop}} = 0.2u_{\text{nyq}}$ (d) FDP, $\mathbf{f}_6$, $u_{\text{stop}} = 0.4u_{\text{nyq}}$

Figure 7.10: Axial slices of regularized ($\beta = 0.0005$) FDP reconstructions of the Thorax phantom for different values of u_{stop}. For each value of u_{stop}, three axial slices are shown. The locations of these slices are given by (top to bottom) $z \approx -10$mm, $z \approx -11$mm and $z \approx -12$mm. See also Figure 7.11. Grey scale window ±30HU.

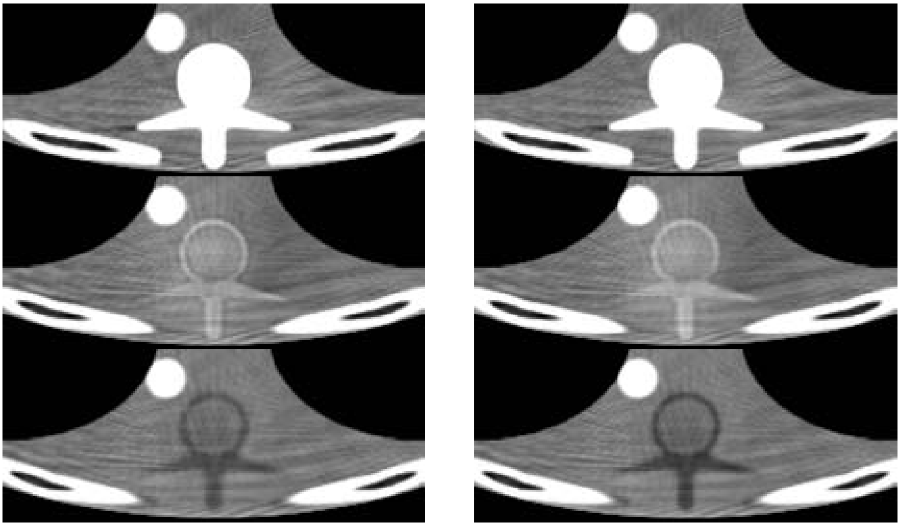

(a) FDP, $\mathbf{f}_6$, $u_{\mathrm{stop}} = 0.6u_{\mathrm{nyq}}$ (b) Regularized IWFBP, $\mathbf{f}_6$, $\beta = 0.0005$

Figure 7.11: Axial slices of regularized ($\beta = 0.0005$) FDP reconstructions of the Thorax phantom for different values of u_{stop}. For each value of u_{stop}, three axial slices are shown. The locations of these slices are given by (top to bottom) $z \approx -10$mm, $z \approx -11$mm and $z \approx -12$mm. See also Figure 7.11. Grey scale window ±30HU.

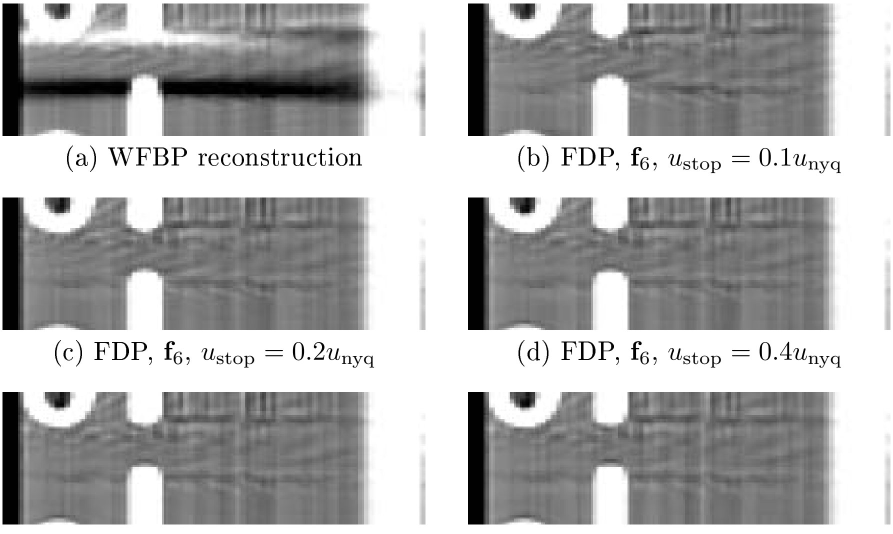

(a) WFBP reconstruction (b) FDP, $\mathbf{f}_6$, $u_{\mathrm{stop}} = 0.1u_{\mathrm{nyq}}$

(c) FDP, $\mathbf{f}_6$, $u_{\mathrm{stop}} = 0.2u_{\mathrm{nyq}}$ (d) FDP, $\mathbf{f}_6$, $u_{\mathrm{stop}} = 0.4u_{\mathrm{nyq}}$

(e) FDP, $\mathbf{f}_6$, $u_{\mathrm{stop}} = 0.6u_{\mathrm{nyq}}$ (f) Regularized IWFBP, $\mathbf{f}_6$, $\beta = 0.0005$

Figure 7.12: Saggital slices of regularized ($\beta = 0.0005$) FDP reconstructions of the Thorax phantom for different values of u_{stop}. Grey scale window ±30HU.

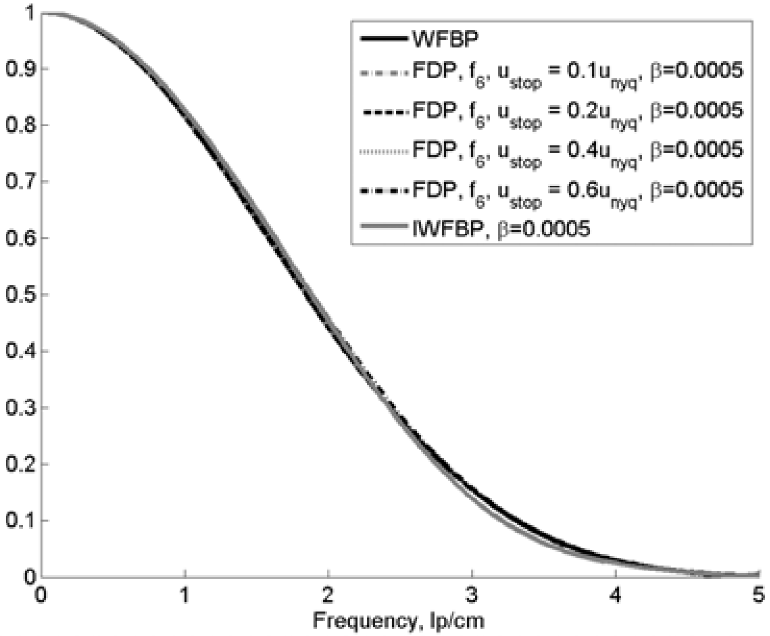

Figure 7.13: MTF measurements for WFBP, regularized IWFBP ($\beta = 0.0005$), and regularized FDP with different values of u_{stop}. Since the MTF of WFBP and IWFBP are very similar, all plots presented here are very similar.

Table 7.4: $Q_1 = c/(\sigma^2 \rho_{10\%}^{-3} SD)$, $Q_2 = c/(\sigma^2 \rho_M^{-3} SD)$ and the entities used for calculating these figures of merit for regularized FDP with different values of u_{stop}. The dose is excluded, since this entity is kept constant.

u_{stop}	σ_n (HU)	$\rho_{10\%}$ (cm^{-1})	$\rho_{50\%}$ (cm^{-1})	S (mm)	Q_1	Q_2
WFBP	3.50	3.30	1.84	2.01	1.47	0.69
$0.1u_{\text{nyq}}$	3.51	3.31	1.85	1.92	1.54	0.73
$0.2u_{\text{nyq}}$	3.55	3.31	1.85	1.86	1.55	0.73
$0.4u_{\text{nyq}}$	3.72	3.31	1.86	1.82	1.44	0.69
$0.6u_{\text{nyq}}$	3.87	3.32	1.89	1.84	1.33	0.64
IWFBP	3.79	3.21	1.88	1.90	1.21	0.60

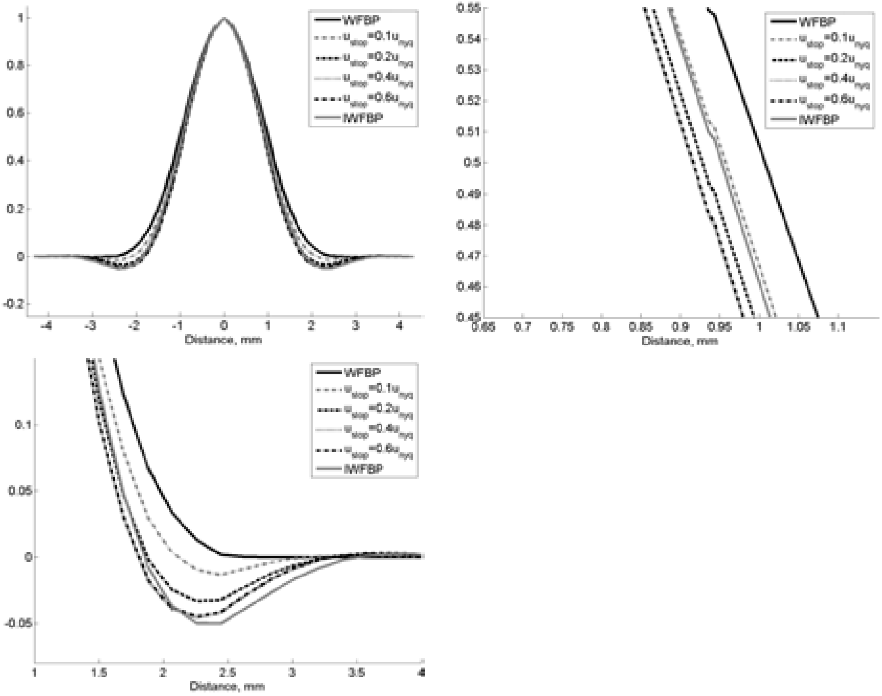

Figure 7.14: SSP measurements for WFBP, regularized IWFBP ($\beta = 0.0005$), and regularized FDP with different values of u_{stop}. These have a slightly larger FWHM and lower overshoot amplitude than in the non-regularized case (cf. 7.9).

than needed by ordinary filtered backprojection methods. Since the computational complexity of the backprojection step in the IWFBP method is $\mathcal{O}(N_x N_y N_z N_\theta)$, doubling the voxel density results in an eight times more expensive backprojection operation. It is therefore meaningful to examine how this operation can be made cheaper.

From Section 7.2, we know that $u_{\text{stop}} = 0.4u_{\text{nyq}}$ implies that $\mathbf{p}_{\text{LF}}$ contains no frequencies higher than approximately 0.52 times the Nyquist frequency of the sampling grid when reconstructing to a 513×513 grid. Therefore, it should be possible to reduce the computational cost both by reconstructing to a sparser grid.

We repeated the experiment presented in Section 5.4 for the FDP methods with $u_{\text{stop}} = 0.1u_{\text{nyq}}$,$u_{\text{stop}} = 0.2u_{\text{nyq}}$ and $u_{\text{stop}} = 0.4u_{\text{nyq}}$. The low contrast phantom presented in Section 4.2, has been two-dimensionally reconstructed to grids with 257×257, 385×385, and 513×513 pixels. Results for these grids are shown in Figure 7.15, 7.16 and 7.17 respectively. For all sampling densities, the largest artifact levels occurred with non-regularized IWFBP. High values of u_{stop} result in artifacts levels similar to those of IWFBP, while low values of u_{stop} result in a significant reduction of artifacts.

7.5 Conclusions

The experiments presented in this chapter illuminates the behavior of the FDP method in terms of spatial resolution and noise. This knowledge is a prerequisite for understanding effects caused by downsampling. More specifically, the following questions have been addressed.

1) How does the choice of the parameter u_{stop} affect the result in terms of cone artifact reduction?

2) How do the MTFs, SSPs and noise properties of the FDP method relate to those of the WFBP and IWFBP methods?

3) If the answer to the previous question is that there is a significant difference, can this difference be reduced by introducing regularization in the iterative part?

4) Can the artifacts that occur in Section 5.4 be reduced by the FDP method?

The answer to the first question is not trivial since it depends on what is meant by cone artifacts. For high values of u_{stop}, we observe that the overshoots caused by the IWFBP method become blurred in the xy-plane. As u_{stop} is reduced, this blurring become more and more apparent, and at some point when u_{stop} is approximately equal to $0.2u_{\text{nyq}}$ the blurred overshoots start to look like blob-artifacts, and cone artifacts start to appear (see Figure 7.5 and 7.6).

Apparently, the frequency characteristics of the FDP method in the xy-plane are such that for frequencies lower than u_{pass}, the FDP MTF is almost equal to the IWFBP MTF. For frequencies higher than u_{stop}, the FDP MTF is very similar to the WFBP MTF. The noise and SSPs of the FDP are similar to the WFBP

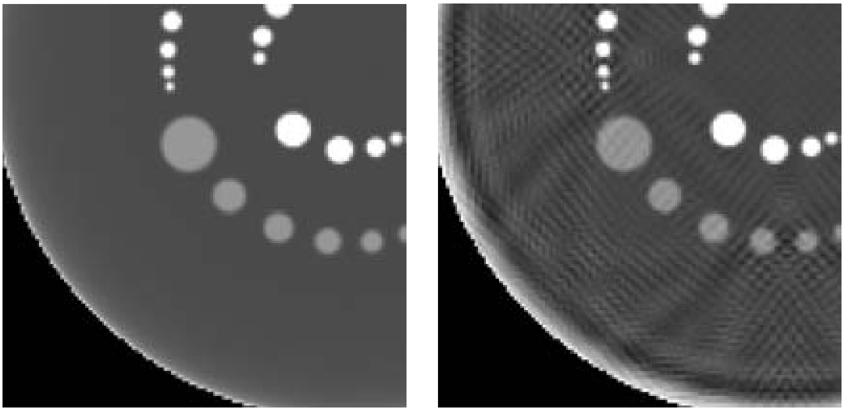

(a) WFBP, $\mathbf{f}_1$ (b) FDP, $u_{\text{stop}} = 0.1u_{\text{nyq}}$

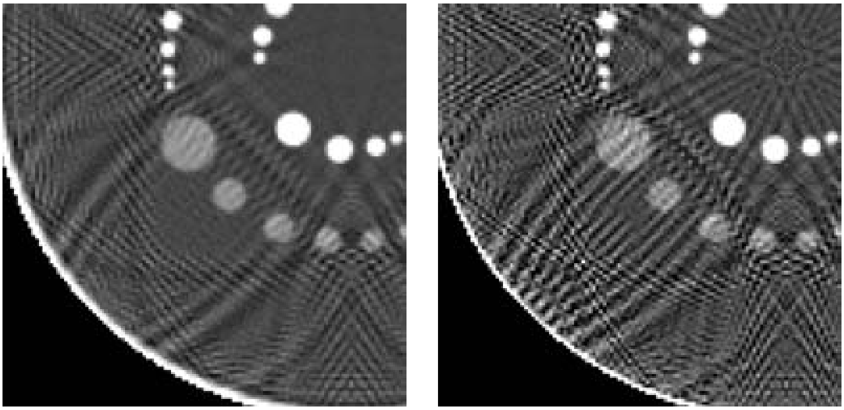

(c) FDP, $u_{\text{stop}} = 0.2u_{\text{nyq}}$ (d) FDP, $u_{\text{stop}} = 0.4u_{\text{nyq}}$

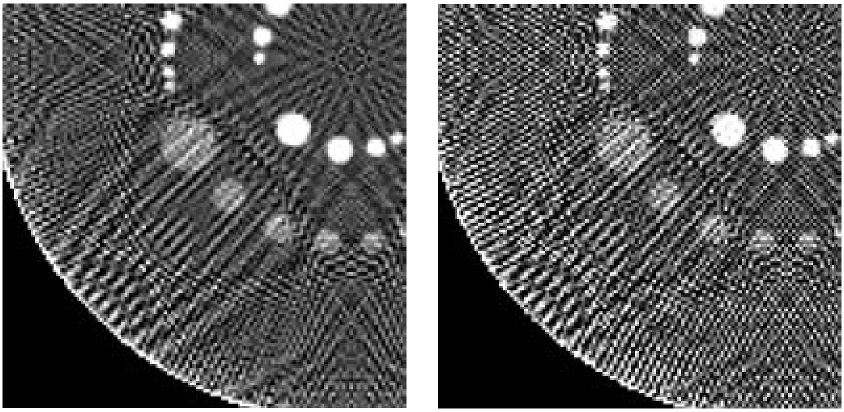

(e) FDP, $u_{\text{stop}} = 0.6u_{\text{nyq}}$ (f) Non-regularized IWFBP

Figure 7.15: FDP reconstructions of the low contrast phantom to a 257×257 grid. Grey scale window ±5HU.

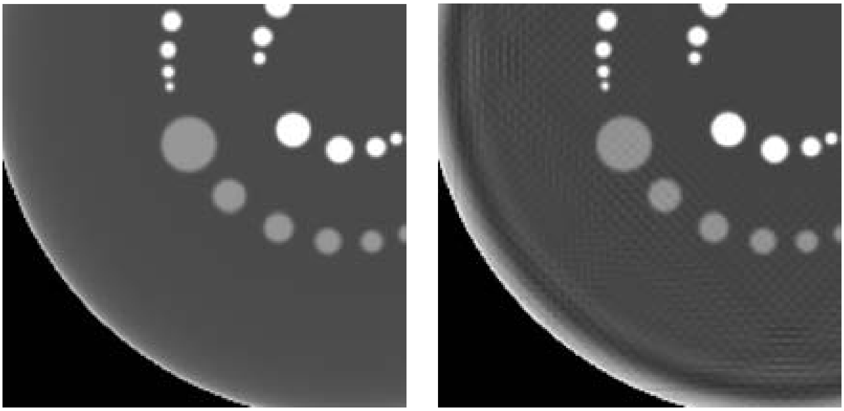

(a) WFBP, $\mathbf{f}_1$ (b) FDP, $u_{\text{stop}} = 0.1u_{\text{nyq}}$

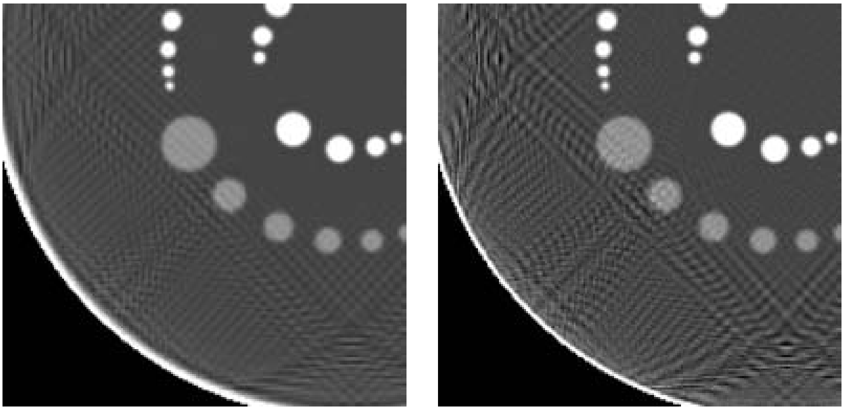

(c) FDP, $u_{\text{stop}} = 0.2u_{\text{nyq}}$ (d) FDP, $u_{\text{stop}} = 0.4u_{\text{nyq}}$

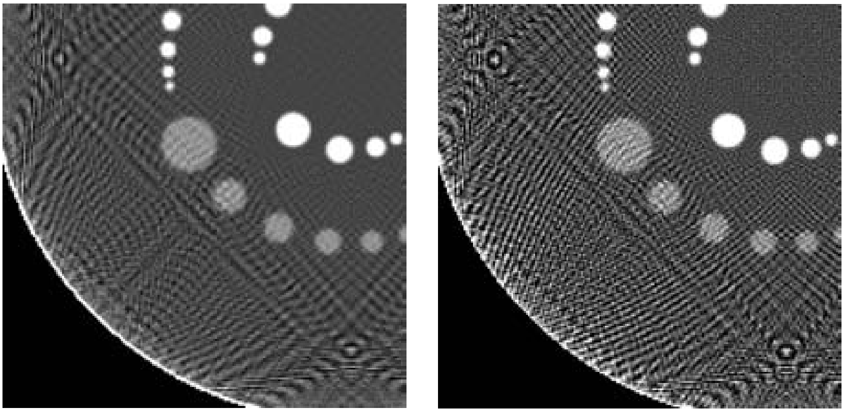

(e) FDP, $u_{\text{stop}} = 0.6u_{\text{nyq}}$ (f) Non-regularized IWFBP

Figure 7.16: FDP reconstructions of the low contrast phantom to a 385 × 385 grid. Grey scale window ±5HU.

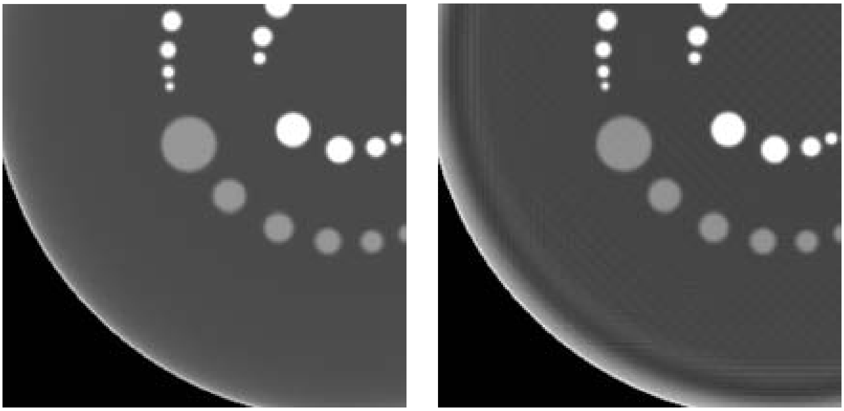

(a) WFBP, $\mathbf{f}_1$ (b) FDP, $u_{\text{stop}} = 0.1u_{\text{nyq}}$

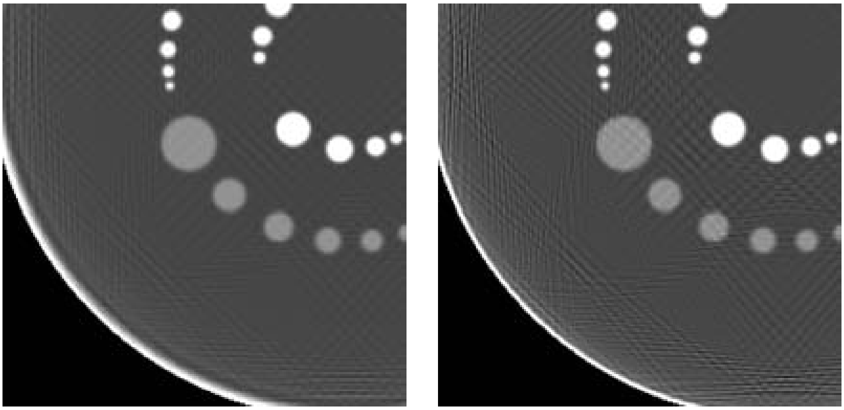

(c) FDP, $u_{\text{stop}} = 0.2u_{\text{nyq}}$ (d) FDP, $u_{\text{stop}} = 0.4u_{\text{nyq}}$

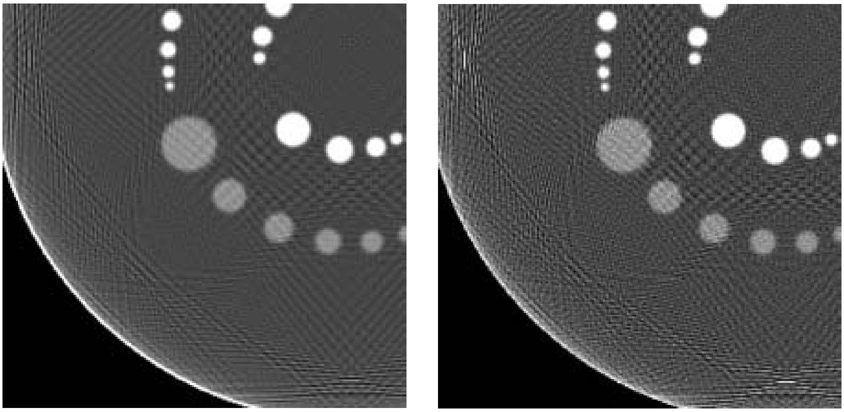

(e) FDP, $u_{\text{stop}} = 0.6u_{\text{nyq}}$ (f) Non-regularized IWFBP

Figure 7.17: FDP reconstructions of the low contrast phantom to a 513 × 513 grid. Grey scale window ±5HU.

for low values of u_{stop} and similar to IWFBP for high values of u_{stop}. Altogether, the spatial resolution and noise properties of the FDP method seems to be a combination of corresponding properties of the WFBP and IWFBP methods.

By using regularization, the spatial resolution and noise properties of the WFBP and IWFBP methods become very similar. From the results in Section 7.3, we see that this applies also to the FDP method. Indeed, apart from the overshoots of the FDP results in the z-direction and the cone artifacts in the WFBP result, the images in Figure 7.10a are very similar to those in 7.10d and 7.11a.

Experiments with reconstructions to lower grid densities have shown that the amount of artifacts of the type shown in Figure 7.15 to 7.17 are reduced when using the FDP method instead of the IWFBP method. However, the spatial resolution given by $\rho_{10\%}$ puts a lower bound on the sampling grid density. In our case, this is given by

$$(N_x)_{\text{min}} = \frac{500\text{mm}}{(\Delta_x)_{\text{max}}} = 2 \times \rho_{10\%} \times 500\text{mm}. \tag{7.4}$$

This means that if $\rho_{10\%} = 0.3(\text{mm})^{-1}$, at least a 300×300-grid is needed for any reconstruction method to be able to reconstruct the image without significant aliasing distortion.

Chapter 8

Conclusions and future research

8.1 Summary of conclusions

In this thesis, we have investigated three methods for iterative suppression of artifacts caused by non-exact analytical methods. These methods are the regularized iterative weighted filtered backprojection (IWFBP) method, ordered subsets IWFBP (OS-IWFBP), and the frequency domain partitioning (FDP) method, all of them based on the IFBP scheme proposed by Chang [8], Walters *et al.* [81] and Medoff *et al.* [53].

It was shown in Chapter 5 that the artifacts caused by the WFBP method can be efficiently suppressed within less than five iterations. However, the general image quality of the WFBP and the IWFBP methods are different. The latter is characterized by higher spatial resolution (mostly for the good) and noise level (always for the bad). In order to reduce this difference, a regularization operation, carefully chosen to preserve linearity, was augmented to the iterative loop. The resulting method produced images with similar noise and spatial resolution properties as those of WFBP. Another positive effect of the regularization became evident when we compared rate of change, measured as $\log_{10}(\|\mathbf{f}_{k+1} - \mathbf{f}_k\|/C)$ in Figure 5.6. Clearly, only the regularized IWFBP offers a possibility to use this as a stopping criterion with predictable result. In the non-regularized case, a mistaken guess may cost dearly in terms of many useless iterations. This effect can not be achieved with post-smoothing, which otherwise could have been an alternative to the proposed regularization.

The sampling density in the reconstruction domain together with the chosen basis function determines the highest frequency that is possible to produce with the projection operator $\mathbf{P}$. Thus, if the sampling density is too low, structures containing high frequencies will be erroneously reconstructed. Since projection and backprojection rays that travel through these structures also visit other areas, the artifacts caused by the insufficient sampling density are non-local as shown in Figure 5.16. This is not the case for WFBP, since sampled data in the reconstruction domain are never reused.

The main conclusion of Chapter 6 is that the reduction of cone artifacts in the IWFBP method can indeed be accelerated by the OS technique. For instance, two full OS iterations seem to reduce the cone artifacts as much as three full non-OS iterations. A drawback of the OS-IWFBP method is that its convergence properties are extremely difficult to analyze. The results are generally noisier than for IWFBP and more care must be taken in the choice of gain factor α. Experimentally, in order to maintain convergence at least over a small number of iterations, we found that the gain factor α must be chosen approximately inversely proportional to the number of subsets N_{sets}. By low-pass filtering projection data in the radial direction prior to each update, the gain α could be increased which resulted in a higher rate of convergence. Taking into account the drawbacks of noise amplification and poorer convergence properties, the OS-IWFBP technique might be more useful for cone angles above ±4.8°, where the advantages of acceleration become more apparent.

In Chapter 7, spatial resolution, noise, and cone artifact reduction were investigated for the FDP method with different choices of u_{stop}, the parameter which indicate how much of the frequency band will be subjected to iterative improvement. It was shown that u_{stop} must be greater than or equal to $0.4u_{\text{nyq}}$ in order to efficiently suppress cone artifacts. For smaller values, cone artifacts occurred in the non-iterative high frequency part. By using regularization in the IWFBP part, MTFs very similar to those of the WFBP method were obtained. In the z-direction, the FDP method behaves more like the IWFBP method. So far, no serious investigations of downsampling in the IWFBP part have been made.

8.2 Open questions and suggestions for future research

IWFBP versus least squares methods

In all experiments presented in the thesis, the reconstruction operator $\mathbf{Q}_{\text{WFBP}}$ differs from the transpose of the projection operator $\mathbf{P}^T$ in the following four ways.

1) The rampfilter.

2) The $\cos^2$-weighting of detector data given by Equation (2.17).

3) The normalization in the backprojection operation.

4) The interpolation in the backprojection operation.

With the exception of number four, each step contributes to making the IWFBP method faster than the original Landweber method. However, certain side effects exist.

Step number 2, the $\cos^2$-weighting of detector data, reduces the weight for certain rays, so that the objective is changed from $\|\mathbf{Pf}-\mathbf{p}_{\text{in}}\|$ to $\|\sqrt{\mathbf{W}}(\mathbf{Pf}-\mathbf{p}_{\text{in}})\|$, where $\mathbf{W}$ correspond to the weighting performed. Intuitively, this increases the amount of noise in the reconstructed images. In the experiments presented here, the weighting parameter Q has always been equal to 0.7. It would be interesting to examine how the number of necessary iterations and the signal to noise ratio varies when this parameter is changed.

Step number 3, the normalization in the backprojection operation, can be written as

$$\mathbf{B}_N = \mathbf{D}_0^r \mathbf{P}^T \mathbf{D}_0^p + \cdots + \mathbf{D}_{N_\theta - 1}^r \mathbf{P}^T \mathbf{D}_{N_\theta - 1}^p, \tag{8.1}$$

where $\mathbf{D}_l^r$ and $\mathbf{D}_l^p$, $l = 0, ..., N_\theta - 1$ are diagonal normalization matrices. Multiplication with $\mathbf{P}$ from the right shows that in general, $\mathbf{B}_N\mathbf{P}$ is non-symmetric. This fact prohibits the analysis in terms of square norms as described in Section 3.3. From a theoretical as well as practical viewpoint, a relevant experiment would be to examine how the required number of iterations and noise properties change if this normalization is replaced with the "symmetric" normalization used in SIRT [21, 30], namely

$$\mathbf{B}_N = \mathbf{V}^{-1}\mathbf{P}^T, \tag{8.2}$$

where $\mathbf{V}$ is a diagonal matrix with elements

$$V_{jj} = \sum_{i=1}^{M} P_{ij}, \; j = 1, ..., N. \tag{8.3}$$

Step number 4, the interpolation in the backprojection operation, is another cause for the non-symmetric $\mathbf{QP}$ matrix. As in the previous paragraph, such non-symmetry make it difficult to understand whether the iterative method is convergent. Therefore, it is of relevance to investigate projection operators that allow for their transposes to be used as backprojectors. One example of such an operator is given below in the paragraph on projection operator modeling.

Regularization and sampling density

In the experiments on regularization, the parameters d_{ij} from Section 3.3 were chosen without taking into account the sampling density in the reconstruction domain. This means that the amount of smoothing due to the regularization term is changed if the spatial resolution is changed. Another consequence is that different sampling densities in the xy- and z-directions lead to different amounts of smoothing. It would be interesting to investigate if and how these parameters can be automatically selected so that the amount of smoothing is invariant to the choice of sampling density.

Acceleration of the FDP method

Acceleration of the FDP method by means of downsampling input data and the reconstruction volume as shown in Figure 8.1 remains to be investigated.

An alternative to downsampling is to use ordered subsets in the iterative part of the FDP scheme. Since the highest frequencies have been removed, the noise

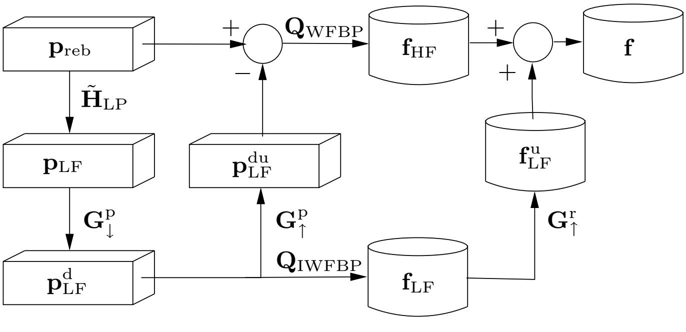

Figure 8.1: Illustration of how downsampling in the angular and radial directions can be used for accelerating the FDP scheme. Here, $\tilde{\mathbf{H}}_{\text{LP}}$ denotes low-pass filtering and $\mathbf{G}^{\text{p}}_{\downarrow}$, $\mathbf{G}^{\text{p}}_{\uparrow}$ and $\mathbf{G}^{\text{r}}_{\uparrow}$ denotes down- and up-sampling operations. The direct reconstruction $\mathbf{Q}_{\text{WFBP}}$ now operates on $(\mathbf{I} - \tilde{\mathbf{H}}_{\text{LP}}\mathbf{G}^{\text{p}}_{\downarrow}\mathbf{G}^{\text{p}}_{\uparrow})\mathbf{p}_{\text{reb}}$ while the iterative reconstruction $\mathbf{Q}_{\text{IWFBP}}$ operates on $\tilde{\mathbf{H}}_{\text{LP}}\mathbf{G}^{\text{p}}_{\downarrow}\mathbf{p}_{\text{reb}}$.

amplification observed in Chapter 6 is not expected to be significant. Instead of the regularization in Section 7.3, post-smoothing can be used. In this way it seems like a good result could be obtained after only two iterations (see Figure 6.11 and 6.12).

Modeling of the projection operator

There are at least two reasons to consider other projection operators than those used in this thesis. These are given below.

1) The Joseph projection operator does not take into account the blurring caused by the gantry rotation, finite size of detector and focus or non-linear phenomena such as beam hardening and the non-linear partial volume effect. Ignoring blurring could cause unnecessarily unsharp results, and ignoring the non-linear effects is bound to generate beam hardening and non-linear partial volume artifacts.

2) Reconstructing images by minimizing $\|\mathbf{Pf}-\mathbf{p}_{\text{in}}\|$, where $\mathbf{P}$ is based on *line integral* calculations inherently lead to non-smooth reconstruction results. By instead using a projection operator that calculates *area integrals*, smoother results can be obtained without using penalty functions [50, 87].

Only preliminary experiments on modeling of the projection operator as described in Section 3.2 have been made so far. There are many possibilities here. By modifying the Joseph projection operator to calculate strip integrals instead of line integrals (cf. De Man and Basu [50] and Ziegler *et al.* [87]), artifacts similar to those in Section 5.4 can be suppressed. Danielsson [10] suggested that more realistic linear physical models can be implemented by fast convolutions with rectangles of variable width. However, it should be noted that better linear modeling is really worthwhile only when applied to non-rebinned data. The rebinning step acts as a blurring screen between the original input data and the projection data generated in the iterative loop.

Beam hardening correction

De Man *et al.* [52] showed how a polychromatic model of the acquisition can be used for suppressing artifacts due to beam hardening. It would be interesting to investigate if these ideas can be transferred to the IWFBP method, and if better results can be achieved in this way than with existing pre-correction methods.

Truncated projection data

Recently, the problem of truncated projection data has gained renewed interest. It was shown by Noo *et al.* [58] and Zou and Pan [90] how a function can be perfectly reconstructed along parallel lines that are fully contained in the scanned region of interest. Later, Defrise *et al.* [14] showed experimentally that even better results could be achieved with the iterative OSEM method. It is not obvious how to extend the methods examined in this thesis to handle this type of truncated projections, but one possibility could be to insert a smooth padding step before rampfiltering in $\mathbf{Q}_{\mathrm{WFBP}}$.

Appendices

A Acronyms

Algebraic reconstruction technique	ART	*p.* 21
Computed tomography	CT	*p.* 1
Contrast recovery coefficient	CRC	*p.* 21
Direct fourier method	DFM	*p.* 10
Electrical and musical industries limited	EMI	*p.* 1
Filtered backprojection	FBP	*p.* 9
Frequency domain partitioning	FDP	*p.* 6
Full width at half maximum	FWHM	*p.* 61
Golden Ratio	GR	*p.* 74
Hounsfield units	HU	*p.* 44
Hudson-Larkin-Beekman-Kamphuis	HLBK	*p.* 73
Iterative filtered backprojection	IFBP	*p.* 5
Iterative weighted filtered backprojection	IWFBP	*p.* 6
Line spread function	LSF	*p.* 47
Markov random field	MRF	*p.* 34
Matlab Connecting ITK and VTK	MCIV	*p.* 45
Maximum a posteriori	MAP	*p.* 22
Maximum likelihood	ML	*p.* 22
Maximum likelihood expectation maximization	MLEM	*p.* 22
Modulation transfer function	MTF	*p.* 47
Ordered subsets	OS	*p.* 6
Ordered subsets IWFBP	OS-IWFBP	*p.* 71
Point spread function	PSF	*p.* 11
Root mean squared error	RMSE	*p.* 44
Signal to noise ratio	SNR	*p.* 21
Simultaneous algebraic technique	SART	*p.* 21
Simultaneous iterative reconstruction technique	SIRT	*p.* 21
Single photon emission computed tomography	SPECT	*p.* 21
Slice sensitivity profile	SSP	*p.* 47
Weighted filtered backprojection	WFBP	*p.* 6

B Notation

The following notational conventions are used. Scalars and functions are denoted with italic lowercase letters, *e.g.* x and $f(x)$. Bold lowercase letters, *e.g.* $\mathbf{r}$, are used for denoting vectors. The jth component of a vector $\mathbf{r}$ is written as r_j. Matrices are denoted by bold uppercase letters, *e.g.* $\mathbf{P}$, and operators are denoted by italic uppercase letters, *e.g.* P_{phys}. The superscript ^{T} is used for denoting the transpose of a vector or a matrix.

Below follows a list of selected symbols used in the thesis. Unfortunately, the symbols α and β mean both fan-beam projection coordinates and parameters for the iterative loop. However, their meaning at a certain location should be clear from the context.

Geometry and sampling

Reconstruction space coordinates	x, y, z	*p.* 2
Reconstruction space coordinate vector	$\mathbf{r}$	*p.* 4
Parallel-beam projection data coordinates	θ, t	*p.* 9
Fan-beam projection data coordinates	α, β	*p.* 14
Projection data row coordinate	q	*p.* 14
Frequency coordinates	u, v	*p.* 10
Radial frequency coordinate	ρ	*p.* 10
Focus-isocenter distance	R_F	*p.* 14, 43
Detector height	h	*p.* 14, 43
Table feed	P	*p.* 14, 43
Maximal fan-angle	β_{max}	*p.* 43
Maximal cone-angle	κ_{max}	*p.* 5
Number of voxels in the xy-plane	N_x, N_y	*p.* 59
Number of reconstructed slices	N_z	*p.* 59
Sampling distance in the xy-plane	Δ_x	*p.* 59
Sampling distance in the z-direction	Δ_z	*p.* 59
Sampling density configurations	$\mathcal{C}_1, \mathcal{C}_2, \mathcal{C}_3$	*p.* 59

Evaluation

Root mean squared error	σ_e	*p.* 44
Noise measurement	σ_n	*p.* 44
Set for error and noise measurement	Ω	*p.* 44
Figure of merit	Q_1	*p.* 49
Figure of merit	Q_2	*p.* 49

WFBP, IWFBP, OS-IWFBP and FDP

Detector row down-weighting parameter (WFBP)	Q	*p.* 15
Regularization parameter (IWFBP)	β	*p.* 34
Number of subsets (OS)	L	*p.* 71
Amount of radial smoothing (OS)	σ	*p.* 80
Pass-band frequency (FDP)	u_{pass}	*p.* 92

Stop-band frequency (FDP)	u_{stop}	*p.* 92

Functions

Frequency for Projection data (2D)	$p(t, \theta)$	*p.* 9
Basis function	$b(\mathbf{r})$	*p.* 22
Irradiation function	$w_i(\mathbf{r})$	*p.* 22
Function to be reconstructed	$f(\mathbf{r})$, $f(x, y)$	*p.* 4, 9
Potential function	$V(\cdot)$	*p.* 34

Vectors and matrices

Reconstruction matrix	$\mathbf{Q}$, $\mathbf{Q}_{\text{WFBP}}$	*p.* 5, 38, 51
Projection matrix	$\mathbf{P}$	*p.* 5, 19
Step-length parameter	α	*p.* 5, 19
Input projection data vector	$\mathbf{p}_{\text{in}}$	*p.* 5, 19
Projection data vector	$\mathbf{p}$	*p.* 5
Sequence of estimates	$\mathbf{f}_1, \mathbf{f}_2, ...$	*p.* 19
Limit point for estimates	$\mathbf{f}_\infty$	*p.* 20
Objective function	$z(\cdot)$	*p.* 20
Regularization matrix	$\mathbf{R}$	*p.* 35

Transforms

1D Fourier transform	$\mathcal{F}$	*p.* 12
1D Fourier transform (radial direction)	$\mathcal{F}_t$	*p.* 10
2D Fourier transform	$\mathcal{F}_2$	*p.* 10
Radon transform	$\mathcal{R}$	*p.* 9

Bibliography

[1] A. H. Andersen and A. C. Kak. Simultaneous algebraic reconstruction technique (SART): A new implementation of the ART algorithm. *Ultrasonic Imaging*, 6(1):81–94, January 1984.

[2] F. J. Beekman and C. Kamphuis. Ordered subset reconstruction for x-ray CT. *Physics in Medicine and Biology*, 46:1835–1844, May 2001.

[3] J. E. Bowsher, M. P. Tornai, J. Peter, D. E. González Trotter, A. Krol, D. R. Gilland, and R. J. Jaszczak. Modeling the axial extension of a transmission line source within iterative reconstruction via multiple transmission sources. *IEEE Transactions on Medical Imaging*, 21(3):200–215, March 2002.

[4] R. N. Bracewell. *The Fourier transform and its applications.* McGraw-Hill, Singapore, 1986.

[5] R. N. Bracewell and A. C. Riddle. Inversion of fan-beam scans in radio astronomy. *Astrophysical Journal*, 150:427–434, November 1967.

[6] R. A. Brooks and G. Di Chiro. Statistical limitations in x-ray reconstructive tomography. *Medical Physics*, 3(4):237–240, July 1976.

[7] Y. Censor, T. Elfving, and G. T. Herman. A method of iterative data refinement and its applications. *Mathematical Methods in the Applied Sciences*, 7:108–123, 1985.

[8] L. T. Chang. A method for attenuation correction in radionuclide computed tomography. *IEEE Transactions on Nuclear Science*, 25(1):638–643, February 1978.

[9] N. H. Clinthorne, T.-S. Pan, P.-C. Chiao, L. Rogers, and J. A. Stamos. Preconditioning methods for improved convergence rates in iterative reconstrucitons. *IEEE Transactions on Medical Imaging*, 12(1):78–83, March 1993.

[10] P.-E. Danielsson. Personal communication.

[11] P.-E. Danielsson, P. Edholm, J. Eriksson, and M. Magnusson Seger. Towards exact 3D-reconstruction for helical cone-beam scanning of long objects. A new detector arrangement and a new completeness condition. In *International meeting on fully three-dimensional image reconstruction in radiology and nuclear medicine*, 1997.

[12] P.-E. Danielsson and M. Magnusson Seger. A proposal for combining FBP and ART in CT-reconstruction. In *International meeting on fully three-dimensional image reconstruction in radiology and nuclear medicine*, 2003.

[13] P.-E. Danielsson and M. Magnusson Seger. Combining Fourier and iterative methods in computer tomography. Analysis of an iteration scheme. The 2D-case. Technical Report LiTH-ISY-R-2634, ISSN 1400-3902, Department of Electrical Engineering, Linköping University, March 2005.

[14] M. Defrise, F. Noo, R. Clackdoyle, and H. Kudo. Enlargement of the region of accurate reconstruction in computed tomography from truncated data. In *International meeting on fully three-dimensional image reconstruction in radiology and nuclear medicine*, pages 46–50, July 2005.

[15] M. Defrise, F. Noo, and H. Kudo. A solution to the long-object problem in helical cone-beam tomography. *Physics in Medicine and Biology*, 45:623–643, 2000.

[16] I. A. Elbakri and J. A. Fessler. Statistical image reconstruction for polyenergetic x-ray computed tomography. *IEEE Transactions on Medical Imaging*, 21(2):89–99, February 2002.

[17] T. Flohr, K. Stierstorfer, H. Bruder, J. Simon, A. Polacin, and S. Schaller. Image reconstruction and image quality evaluation for a 16-slice CT scanner. *Medical Physics*, 30(5):832–845, May 2003.

[18] T. Fuchs. Simulation of noise. As available electronically in February 2007 at `http://www.imp.uni-erlangen.de/phantoms/index.html`.

[19] H. Erdoğan and J. A. Fessler. Ordered subsets algorithms for transmission tomography. *Physics in Medicine and Biology*, 44:2835–2851, 1999.

[20] S. Geman and D. E. McClure. Statistical methods for tomographic image reconstruction. *Bulletin of the International Statistical Institute*, 52:5–21, 1987.

[21] P. Gilbert. Iterative methods for the reconstruction of three-dimensional objects from their projections. *Journal of Theoretical Biology*, 36:105–117, 1972.

[22] R. Gordon, R. Bender, and G. T. Herman. Algebraic reconstruction techniques (ART) for three dimensional electron microscopy and x-ray photography. *Journal of Theoretical Biology*, 29:241–481, 1970.

[23] R. P. Grimaldi. *Discrete and combinatorial mathematics.* Addison Wesley Longman, 4th edition, 2000.

[24] K. M. Hanson and G. W. Wecksung. Local basis-function approach to computed tomography. *Applied Optics*, 24(23):4028–4039, December 1985.

[25] M. T. Heath. *Scientific computing. An introductory survey.* McGraw-Hill, New York, 2nd edition, 2002.

[26] T. Hebert, R. Leahy, and M. Singh. Fast MLE for SPECT using an intermediate polar representation and a stopping criterion. *IEEE Transactions on Nuclear Science*, 35(1):615–619, 1988.

[27] G. T. Herman. *Image reconstruction from projections. The fundamentals of computerized tomography.* Academic Press, New York, 1980.

[28] J. Hsieh. *Computed tomography. Principles, design, artifacts and recent advances.* SPIE Press, Washington, 2 edition, 2003.

[29] H. M. Hudson and R. S. Larkin. Accelerated image reconstruction using ordered subsets of projection data. *IEEE Transactions on Medical Imaging*, 13(4):601–609, December 1994.

[30] M. Jiang and G. Wang. Convergence of the Simultaneous Algebraic Reconstruction Technique (SART). *IEEE Transactions on Image Processing*, 12(8):957–961, August 2003.

[31] M. Jiang and G. Wang. Convergence studies on iterative algorithms for image reconstruction. *IEEE Transactions on Medical Imaging*, 22(5):569–579, May 2003.

[32] P. M. Joseph. An improved algorithm for reporjection rays through pixel images. *IEEE Transactions on Medical Imaging*, 1:193–196, June 1982.

[33] P. F. Judy. The line spread function and modulation transfer function of a computed tomographic scanner. *Medical Physics*, 3(4):233–236, July 1976.

[34] A. C. Kak and M. Slaney. *Principles of computerized tomographic imaging.* IEEE Press, New York, 1988.

[35] W. A. Kalender. *Computed Tomography. Fundamentals, system technology, image quality, applications.* Publicis, Erlangen, 2005.

[36] C. Kamphuis and F. J. Beekman. Accelerated iterative transmission CT Reconstruction using an ordered subsets convex algorithm. *IEEE Transactions on Medical Imaging*, 17(6):1101–1105, December 1998.

[37] A. Katsevich. Theoretically exact FBP-type inversion algorithm for spiral CT. In *International meeting on fully three-dimensional image reconstruction in radiology and nuclear medicine*, 2001.

[38] A. Katsevich. Theoretically exact filtered backprojection-type inversion algorithm for spiral CT. *SIAM Journal on Applied Mathematics*, 62(6):2012–2026, 2002.

[39] T. Köhler. A projections access scheme for iterative reconstruction based on the golden section. In *Nuclear Science Symposium Conference Record, 2004 IEEE*, volume 6, pages 3961–3965, October 2004.

[40] H. Kudo, S. Park, F. Noo, and M. Defrise. Performance of quasi-exact cone-beam filtered backprojection algorithm for axially truncated data. *IEEE Transactions on Nuclear Science*, 46(3):608–617, 1999.

[41] L. Landweber. An iteration formula for Fredholm integral equations of the first kind. *American Journal of Mathematics*, 73(3):615–624, July 1951.

[42] K. Lange and R. Carson. EM reconstruction algorithms for emission and transmission tomography. *Journal of Computer Assisted Tomography*, 8(2):306–16, 1984.

[43] K. Lange and J. A. Fessler. Globally convergent algorithms for maximum a posteriori transmission tomography. *IEEE Transactions on Medical Imaging*, 4(10):1430–1438, October 1995.

[44] F. Larsson, L. Arvidsson, A. Eklund, L. Gustafsson, and N. Ingemars. Matlab connecting ITK and VTK. As available electronically in February 2007 at `http://www.cvl.isy.liu.se/Education/UnderGraduate/TSBB51/MCIV/about.html`.

[45] R. M. Lewitt. Multidimensional digital image representations using generalized Kaiser-Bessel window functions. *Journal of the Optical Society of America A*, 7(10):1834–1846, October 1990.

[46] R. M. Lewitt. Alternatives to voxels for image represntation in iterative reconstruction algorithms. *Physics in Medicine and Biology*, 37(3):705–716, October 1992.

[47] Z. Liang, R. Jaszczak, and K. Greer. On bayesian image reconstruction from projections: Uniform and nonuniform a priori source information. *IEEE Transactions on Medical Imaging*, 8(3):227–235, September 1989.

[48] M. Magnusson, P.-E. Danielsson, and J. Sunnegårdh. Handling of long objects in iterative improvement of nonexact reconstruction in helical cone-beam CT. *IEEE Transactions on Medical Imaging*, 25(7):935–940, July 2006.

[49] B. De Man. *Iterative reconstruction for reduction of metal artifacts in computed tomography.* Phd thesis, Katholieke Universiteit Leuven, 2001.

[50] B. De Man and S. Basu. Distance-driven projection and backprojection in three dimensions. *Physics in Medicine and Biology*, 49:2463–2475, 2004.

[51] B. De Man, J. Nuyts, P. Dupont, G. Marchal, and P. Suetens. Reduction of metal streak artifacts in x-ray computed tomography using a transmission maximum a posteriori algorithm. *IEEE Transactions on Nuclear Science*, 47(3):977–981, June 2000.

[52] B. De Man, J. Nuyts, P. Dupont, G. Marchal, and P. Suetens. An iterative maximum-likelihood polychromatic algorithm for CT. *IEEE Transactions on Medical Imaging*, 20(10):999–1008, October 2001.

[53] B. P. Medoff, W. R. Brody, M. Nassi, and A. Mocovski. Iterative convolution backprojection algorithms for image reconstruction from limited data. *Journal of the Optical Society of America B*, 73:1493–1500, 1983.

[54] K. Mueller, R. Yagel, and J. J. Wheller. Anti-aliased three-dimentional cone-beam reconstruction of low-contrast objects with algebraic methods. *IEEE Transactions on Medical Imaging*, 18(6):519–537, June 1999.

[55] K. Mueller, R. Yagel, and J. J. Wheller. Fast implementations of algebraic methods for three-dimensional reconstruction from cone-beam data. *IEEE Transactions on Medical Imaging*, 18(6):538–548, June 1999.

[56] F. Natterer. *The mathematics of computerized tomography.* Wiley and B.G. Teubner, Stuttgart, 1986.

[57] J. Nocedal and S. J. Wright. *Numerical optimization.* Springer Series in Operations Research. Springer, second edition, 1999.

[58] F. Noo, R. Clackdoyle, and J. D. Pack. A two-step Hilbert transform method for 2D image reconstruction. *Physics in Medicine and Biology*, 49:3903–3923, 2004.

[59] J. Nuyts, B. De Man, P. Dupont, M. Defrise, P. Suetens, and L. Mortelmans. Iterative reconstruction for helical CT: a simulation study. *Physics in Medicine and Biology*, 43:729–737, 1998.

[60] N. Ohyama, S. Ohki, S. Inoue, J. Tsujiuchi, and T. Honda. Discrete radon transform in a continuous space. *Journal of the Optical Society of America A*, 4(2):318–324, February 1987.

[61] J. D. O'Sullivan. A fast sinc function gridding algorithm for fourier inversion in computer tomography. *IEEE Transactions on Medical Imaging*, MI-4(4):200–207, December 1985.

[62] T. M. Peters. Algorithms for fast back- and reprojection in computed tomography. *IEEE Transactions on Nuclear Science*, NS-28:3641–3647, 1981.

[63] J. Radon. Über die Bestimmung von Funktionen durch ihre Integralwerte längs gewisser Mannigfältigkeiten. *Berichte Sächsiche Akademie der Wissenschaften. Leipzig.*, 69:262–267, 1917. Reprinted in J. Radon, Gesammelte Abhandlungen, Birkhäuser Verlag, Vienna, 1987.

[64] S. Schaller. Low contrast phantom. As available electronically in February 2007 at `http://www.imp.uni-erlangen.de/phantoms/index.html`.

[65] S. Schaller, F. Noo, F. Sauer, K.C. Tam, G. Lauritsch, and T. Flohr. Exact Radon rebinning algorithms using local region-of-interest for helical cone-beam CT. In *International meeting on fully three-dimensional image reconstruction in radiology and nuclear medicine*, pages 11–14, 1999.

[66] M. Magnusson Seger. *Linogram and other direct Fourier methods for tomographic reconstruction.* PhD thesis 320, Department of Electrical Engineering, Linköping University, Linköping, Sweden, November 1993.

[67] L. A. Shepp and Y. Vardi. Maximum likelihood reconstruction for emission tomogrphy. *IEEE Transactions on Medical Imaging*, MI-1(2):113–121, October 1982.

[68] R. L. Siddon. Fast calculation of the exact radiological path for a three-dimensional CT array. *Medical Physics*, 12(2):252–255, Mars 1985.

[69] M. D. Silver, K. Taguchi, I. A. Hein, B. Chiang, M. Kazama, and I. Mori. Windmill artifact in multislice helical CT. In *Proceedings of SPIE, Medical Imaging*, volume 5032, pages 1918–1927, May 2003.

[70] D. L. Snyder and M. I. Miller. The use of sieves to stabilize images produced with the EM algorithm for emission tomography. *IEEE Transactions on Nuclear Science*, NS-32:3864–3872, October 1985.

[71] D. L. Snyder, M. I. Miller, L. J. Thomas, and D. G. Politte. Noise and edge artifacts in maximum-likelihood reconstructions for emission tomography. *IEEE Transactions on Medical Imaging*, MI-6(3):228–236, September 1987.

[72] K. Sourbelle. Thorax phantom. As available electronically in February 2007 at `http://www.imp.uni-erlangen.de/phantoms`.

[73] K. Stierstorfer, T. Flohr, and H. Bruder. Segmented multiple plane reconstruction: a novel approximate reconstruction scheme for multi-slice spiral CT. *Physics in Medicine and Biology*, 47:2571–2581, July 2002.

[74] K. Stierstorfer, A. Rauscher, J. Boese, H. Bruder, S. Schaller, and T. Flohr. Weighted FBP - a simple approximate 3DFBP algorithm for multislice spiral CT with good dose usage for arbitrary pitch. *Physics in Medicine and Biology*, 49:2209–2218, 2004.

[75] J. Sunnegårdh. Iterative enhancement of non-exact reconstruction in cone beam CT. Master's thesis, Linköpings Universitet, September 2004.

[76] J. Sunnegårdh, P.-E. Danielsson, and M. Magnusson Seger. Iterative improvement of non-exact reconstruction in cone-beam CT. In *International meeting on fully three-dimensional image reconstruction in radiology and nuclear medicine*, 2005.

[77] H. Turbell. *Cone-Beam reconstruction using filtered backprojection.* PhD thesis 672, Department of Electrical Engineering, Linköping University, Linköping, Sweden, February 2001.

[78] H. Turbell and P.-E. Danielsson. Helical cone-beam tomography. *International Journal of Imaging Systems and Technology*, 11(1):91–100, 2000.

[79] M. Unser. Splines. A perfect fit for signal processing. *IEEE Signal processing magazine*, 16(6):22–38, November 1999.

[80] E. Veklerov and J. Llacer. Stopping rule for the MLE algorithm based on statistical hypothesis testing. *IEEE Transactions on Medical Imaging*, MI-6(4):313–319, December 1987.

[81] E. Walters, W. Simon, D. A. Chesler, and J. A. Correia. Attenuation correction in gamma emission computed tomography. *Journal of Computer Assisted Tomography*, 5:89–94, 1981.

[82] X.-L. Xu, J.-S. Liow, and S. C. Strother. Iterative algebraic reconstruction algorithms for emission computed tomography: A unified framework and its application to positron emission tomography. *Medical Physics*, 20(6):1675–1684, November 1993.

[83] G. Yang and D. N. Firmin. The birth of the first CT Scanner. *IEEE Engineering in Medicine and Biology*, 19(1):120–125, January-February 2000.

[84] W. Zbijewski and F. Beekman. Characterization and suppression of edge and aliasing artefacts in iterative x-ray CT reconstruction. *Physics in Medicine and Biology*, 49:145–157, 2004.

[85] G. L. Zeng and G. T. Gullberg. Unmatched projector/backprojector pairs in an iterative reconstruction algorithm. *IEEE Transactions on Medical Imaging*, 19(5):548–555, May 2000.

[86] K. Zeng, Z. Chen, and L. Zhang. An error-reduction-based algorithm for cone-beam computed tomography. *Medical Physics*, 31(12):3206–3212, December 2004.

[87] A. Ziegler, T. Köhler, T. Nielsen, and R. Proksa. Iterative cone-beam CT image reconstuction with spherically symmetric basis functions. In *International meeting on fully three-dimensional image reconstruction in radiology and nuclear medicine*, pages 80–83, July 2005.

[88] Y. Zou and X. Pan. Exact image reconstruction on PI-lines from minimum data in helical cone-beam CT. *Physics in Medicine and Biology*, 49:941–959, 2004.

[89] Y. Zou and X. Pan. Image reconstruction on PI-lines by use of filtered backprojection in helical cone-beam CT. *Physics in Medicine and Biology*, 49:2717–2731, 2004.

[90] Y. Zou and X. Pan. Image reconstruction in regions-of-interest from truncated projections in a reduced fan-beam scan. *Physics in Medicine and Biology*, 50:13–27, 2005.